Single Electron Charge Pumps Based on Single Wall Carbon Nanotubes

Dissertation

zur Erlangung des Grades eines

Doktors der Naturwissenschaften

der Fakultät für Mathematik und Physik

der Eberhard-Karls-Universität Tübingen

vorgelegt von

Dipl.-Phys. Viktor Siegle

aus Karaganda

Tübingen

2010

Tag der mündlichen Prüfung: 28.06.2010

Dekan: Prof. Dr. W. Knapp

1. Berichterstatter: Prof. Dr. D. Kern

2. Berichterstatter: Dr. habil. S. Roth

Abstract

The aim of this work is to experimentally investigate the suitability of the single wall carbon nanotubes (SWNT) for single electron charge pumps. Approaches using surface acoustic waves, local gating and properties of the superconducting–isolating–normal conducting interface (SINIS) are examined.

These investigations result in a novel SWNT device. In the SINIS configuration an individual SWNT or a thin bundle is contacted by layered Nb/Ti–contacts. The periodic modulation is provided by the AC signal applied at a nearby gate. The first SWNT–based SINIS device is successfully operated in the frequency range up to 80 MHz with quantized currents of several picoamperes. The quantization of the current is achieved as function of applied source–drain voltage, the magnitude of the applied AC–signal and the value of the DC gate voltage. Effects observed during the operation of the device are discussed.

Zusammenfassung

In der vorliegenden Arbeit wird die Eignung der einwändigen Kohlenstoffröhrchen (SWNT) für Einzelelektronenpumpen untersucht. Verfolgt werden unterschiedliche Ansätze basierend auf Oberflächenwellen, lokalem Gaten und Eigenschaften vom Übergang zwischen einem Supraleiter, Isolator und einem Normalleiter (SINIS).

Das Ergebnis dieser Untersuchungen ist eine neuartige SWNT–basierte Einzelelektronenpumpe basierend auf dem SINIS–Ansatz. Im Kern besteht sie aus einem Kohlenstoffröhrchen(bündel) mit Nb/Ti–Kontakten. Die Stromquantisierung wird durch das Anlegen von einem HF–Signal am Gate erreicht. Die quantiesierten Ströme sind in der Größenordnung von einigen Pikoampere. Die Quantisierung kann durch Variiren von unterschiedlichen Parametern erreicht werden. Im Anschluss werden Effekte diskutiert, die wärend des Betriebs einer solchen Pumpe beobachtet werden können.

Contents

Appendix

List of Figures

Chapter 1

Motivation & Overview

1.1 The SI and the Metrological Triangle

The International System of Units – or SI in short – provides a set of basic units. This set is internationally used for measurements both in and outside of science. Its choice influences not only the numbers resulting from our experiments, but also our understanding of the matter we are dealing with. It is therefore not surprising, that SI is subject to careful but continuous changes going along with progresses in technology and scientific insight.

In the beginnings of SI the basic units were connected to artefacts. So, metre was defined by the length of a particular metal bar. This type of definition, albeit intuitive, has intrinsic limitations in usability and precision as it depends on material properties of this very artefact. Only after the metre was linked to the speed of light – a natural constant – its definition became universal.

Electric basic units – voltage, current and resistance – all connected by Ohm's law, form the so called metrological triangle[1–3]. In analogy to the metre, it is possible to link the edges of this triangle to natural constants, as can be seen in Fig. 1.1. The precision of the experiments employing the quantum Hall effect, discovered by von Klitzing[4, 5], and Josephson effects[6] is sufficiently high for metrological purposes[7].

However, it is not yet possible to produce a current, which would satisfy metrological requirements. This poses a problem in several respects. Firstly, it prevents a direct experimental validation of the metrological triangle, which is still missing and highly desirable. The second reason is that in SI the uncertainties of basic units are interconnected, just as the respective units themselves. Therefore, the low precision of the base unit Ampere affects the overall precision of the SI, which is a serious obstacle on the way to new physics.

Over the last two decades several methods for *quantized charge pumping* were proposed and realized, using both static[8] and modulated[9] tunneling barriers, multiple tunneling junctions[10, 11], local gating of 1D-channel[12], scaled–down charge-coupled devices[13] and moving quantum dots created by surface acoustic waves[14].

Most of the approaches aiming at the solution of the problem involve top–down technological processes which result in devices which are as small as hundreds of nanometres. However, as of now, despite of a large variety in approaches, there are no metrologically satisfying results.

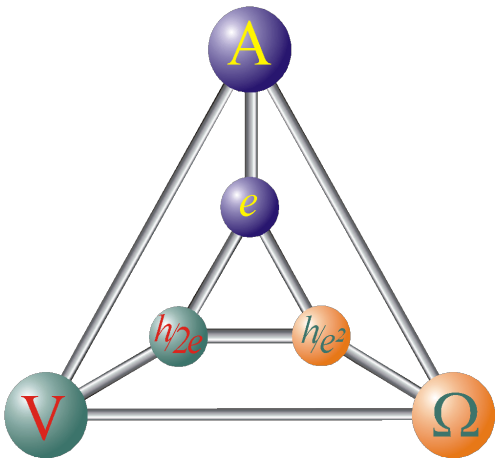

Figure 1.1: Illustration of the metrological triangle. Electrical units can be linked to fundamental constants. Josephson and quantum Hall effect provide a possible definition for voltage and resistance, respectively. In analogy, electrical current can be defined precisely by single electron pumping.

1.2 Carbon nanotubes – a nano-playground

Since the publication by Iijima in 1991[15] much attention was devoted to carbon nanotubes – in many aspects, by many scientists[16]. Carbon nanotubes (CNT) are often described as elongated fullerenes or as seamlessly wrapped up graphene sheets. They exist either as a single shell (so called *single wall carbon nanotube*, SWNT, Fig. 1.2(a)), or as shells nested within each other (*multi wall carbon nanotube*, MWNT, Fig. 1.2(b)) A good introduction into the field of carbon nanotubes can be found in [17–20]; details relevant for this work are given in Appendix C on page 99.

Dimensions CNTs are very thin (typically 1–100 nm) but long (typically several µm) which leads to a large ratio between length and thickness (so called *aspect ratio*) of 10^3–10^8. The length of the CNTs is macroscopic (single tubes with more than 2 mm length have been reported by Zheng et al. in 2004[22]). On the other hand, the small width of CNTs gives rise to effects specific for low–dimensional structures (e.g. *single electron charging/Coulomb oscillations* or *van Hove singularities*). CNTs represent so called *mesoscopic*[1][23] material. Their properties originate from the transition between the macroscopic to the microscopic, atom–size scale.

Material properties CNTs are light but tougher than steel; they conduct heat better than diamond. As for electrical conduction, CNTs show a certain peculiar-

[1] from Greek $\mu\varepsilon\sigma o\varsigma$ = in between

Figure 1.2: Illustration of different carbon nano structures

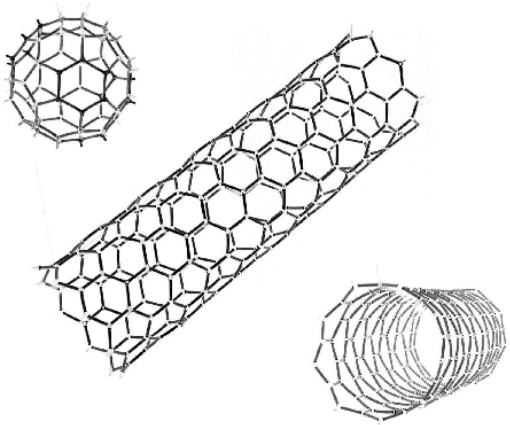

(a) An illustration of a fullerene (top left corner) and a (single wall) carbon nanotube (middle and bottom right).

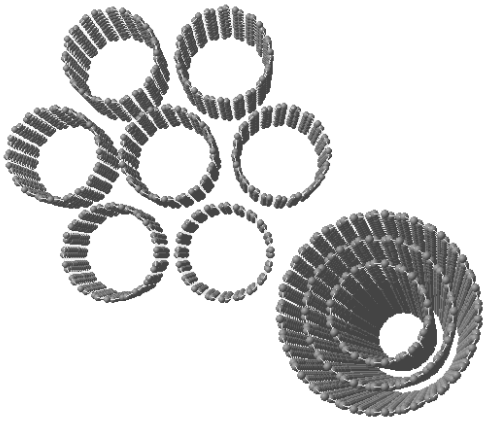

(b) An illustration of a SWNT bundle (upper left) and an individual multi wall carbon nanotube (bottom right) [21]

ity: depending on how the imaginary graphene sheet is wrapped up to form a nanotube (so called *rolling vector*[1]) its properties can vary from semiconducting to metal-like. The size of the band gap depends on the rolling vector. For vanishing band gap one obtains so called *metallic* tubes, which allow higher current densities than copper wires.
Under certain circumstances electrons in CNTs can have a very long (up to several hundred nanometer[24]) mean free path. For mean free paths longer than the actual length of the CNT one speaks of *ballistic transport*.
These outstanding properties gave rise to the popularity of CNTs. In the last years a large variety of devices was reported, which utilize either individual features or a suitable combination of them. The dimensions, semiconducting/metallic properties, and the ballistic nature of the electrical and spin transport in nanotubes lead among other things to following CNT–devices:

- cold electron sources[25]
- CNT-based transistor[26]
- light emitting devices[27]
- spintronic devices[28]

[1] sometimes also called *helicity vector*

Recently, a new development in the research of carbon nanotubes gained weight, namely the frequency–dependent behaviour of SWNT. A high frequency transistor based on an individual carbon nanotube was implemented by Appenzeller and Frank in 2004[29]. This device, switched by a back gate, showed no degradation of signal up to 580 MHz, a limit imposed by the experimental setup. Another device, operating via top–gates in the range of 0.1–1.6 GHz at room temperature was reported by Chaste et al. in 2008[30] (see Fig. 1.3). Also flexible transistors based on SWNT networks and operating in gigahertz regime were reported [31].

It is obvious that a nanotube device operating at such frequencies could have an variety of applications, as demonstrated by a nanotube radio (Jensen et al.[32]). Another application, which might be relevant for metrology, is the real–time electron counting as reported by Bylander et al. in 2005[33].
Beyond that, the SWNT is expected to operate in terahertz regime due to its properties as a ballistic conductor and its very small capacitances. This area is also a subject of intensive current investigations[34, 35].

Figure 1.3: Top–gate SWNT transistor operating in gigahertz regime [30]. The gate length is 300 nm.

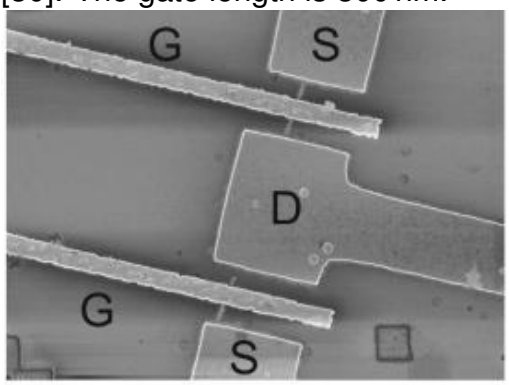

1.3 Quantized current with SWNTs

Both the field of carbon nanotubes and single electron pumping evolved strongly in the last two decades. Combining these two fields creates many unexplored aspects. Consequently, the application of SWNT in devices generating quantized currents was not only suggested recently by several authors (Talyanskii et al.[36] and Kaestner[37]), but also partly implemented by Leek et al.[38] and Würstle et al.[39].
Indeed, using SWNT has several advantages compared with conventional semiconducting or metallic systems. As a rule of thumb, both accuracy and the maximum current which of a charge pump depend on the charging energy E_c of the

island. Increasing of E_c usually implies a reduction of island's dimensions, a procedure which has been extensively followed[40]. Yet there's an alternative to this top-down approach.
The field of molecular electronics offers a great variety of suitable candidates for small size, high E_c single electron devices. Especially carbon nanotubes offer an extended playground for low dimensional physics and single electron devices since 1990s[41].
The capacitance of a SWNT with 1–1.5 nm in diameter and 300–900 nm length can be as small as some attofarad, resulting in a charging energy E_c=2–20 meV. This value is 1-2 orders of magnitude higher than the one obtained by common methods, giving a big advantage for generation of quantized currents.
Despite of the large amount of SWNT–related work, their use for metrological purpose remained a topic addressed by a few publications[38, 39, 42]. Also many aspects are not clear or not investigated so far.
The aim of the presented work is to experimentally investigate the suitability of single wall carbon nanotubes for devices generating quantized current. Several possibilities were analyzed and examined. As a result of these investigations a novel SWNT device could be implemented and operated, based on the idea of the hybrid turnstile device as proposed by Pekola et al.[43].
The resulting device allows the generation of quantized charge currents controlled to an extend which was not achieved before with nanotube–based devices.

1.4 Organization of this thesis

This work is organized in several chapters. Chapter 2 starts with an overview of basic principles of charge pumping. Several proposals for sources of quantized currents, including SWNT-based, are introduced, together with their implementations and experimental data.
Chapter 3 gives details on experimental part of the thesis. The first part of the chapter deals with the device fabrication. Details on the measurement setup and techniques used in this work are discussed in the second part.
Several implementations for a SWNT based source of a quantized current were tested during this work. Chapter 4 is therefore devided in three parts, each dealing with results obtained for each individual implementation.

Finally, Chapter 5 summarizes the thesis and gives an outlook on the field of SWNT based quantized charge pumps and turnstiles.
For an easier access to the very diverse topic discussed within this work, there is an appendix with several short introductions to the respective fields. Appendix A on page 89 gives a quick overview on the field of surface acoustic waves. Single electron transport is introduced in Appendix B on page 93. Single wall carbon nanotubes, and their properties are dealt with in Appendix C on page 99.
These introductions are not meant to give an exhaustive overview of each field involved. Instead, their purpose is rather to provide the reader with important details and main facts relevant for this thesis.

Chapter 2

Charge Pumping

2.1 Basic Principles of Quantized Charge Pumping

Thouless[44] introduced the idea of a quantized charge transport in 1983. Yet the development of quantized charge pumping devices – similarly to SWNT devices – started in the 1990s. It was triggered by realizing that due to the Coulomb repulsion electrons can be loaded one by one on a small metal or semiconducting island even though the total number of electrons on such an island might be very large[45–47] (see also Appendix B.1 on page 93). The possibility of manipulating single electrons attracted large interest and created a broad field of *single electron devices*. The *island* has to be separated from the (*source*) lead by a tunneling junction (with a resistance higher than $R_K = \frac{h}{e^2}$ =25.812 kΩ) and its Fermi level is to be modified by a nearby *gate*. This arrangement is known as *single-electron box*. Adding an *drain* lead results in a device known as *single electron transistor* (SET) as illustrated in Fig. 2.1.

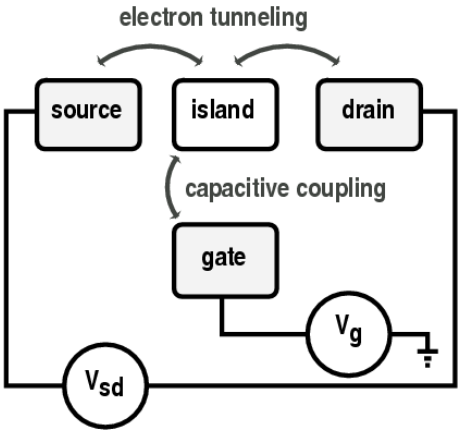

Figure 2.1: A scheme of a single electron transistor (SET). The source and drain leads are separated from the island by high–ohmic junctions. Therefore, the electron transport can occur by tunneling only. The coupling of the gate electrode to the island is purely capacitive. Its function lies in the alignment of the energy states of the island.

Capturing n electrons from the source lead on the island and releasing them some time later on the drain lead results in transferring a charge of exactly $n \cdot e$, with e being the elementary charge. If this cycle is repeated with some frequency f, the resulting current is described by a simple relation

$$I = n \cdot e \cdot f. \tag{2.1}$$

Such devices are commonly referred to as *turnstile devices* if an additional source–drain voltage V_{sd} across the source of quantized current is essential for its operation, otherwise they are denoted as *charge pumps*.
To generate quantized current it is not only necessary to localize a well-defined number of electrons n on an island (which is the case, if the contact resistance

$R >> R_K$ [46]). One also has to ensure that the desired number of electrons tunnels to the desired direction. Difficulties linked to this second issue can be illustrated by analyzing the SET.

Although an SET is perfectly able to *confine* charge on the single electron level (i.e. in the *off–state*, see Fig. 2.2(a)), it fails to control one-by-one electron *flow*. Indeed, Fig. 2.2(b) shows that when the energy states of the island are between the Fermi energy of the leads (the *on–state*), there is no possibility of controlling electrons tunneling from source to drain in a one–by–one way.

Figure 2.2: Working principle of a single electron transistor

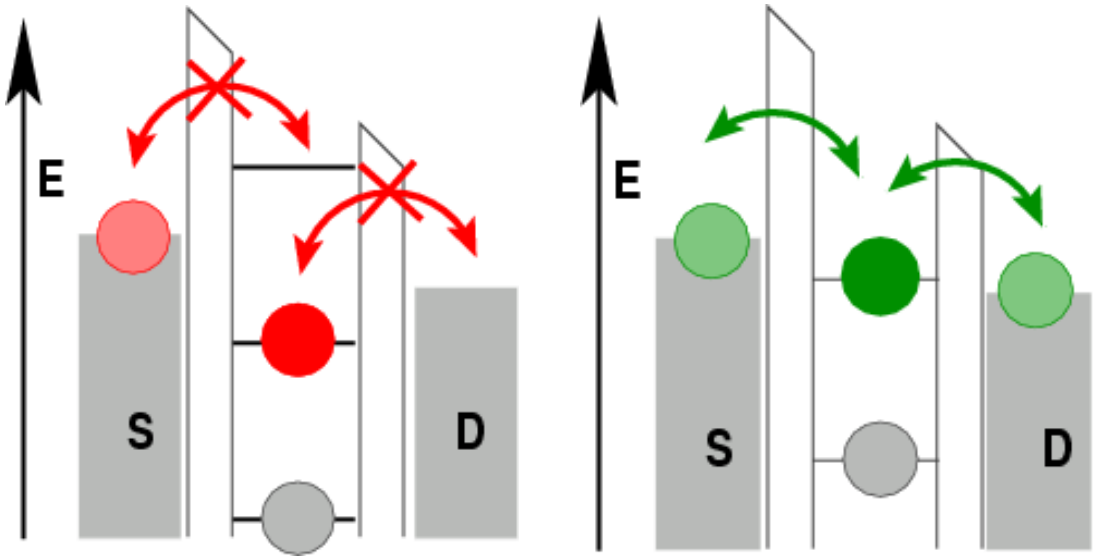

(a) Off–state of an SET. Despite of applied bias no electron transport is possible. The energy of the electron in the highest occupied state of the island is not sufficient to escape to neither of the electrodes. The next higher energy state of the island is energetically not available.

(b) On–state of an SET. When the energy state of the island is in the energy range between the Fermi levels of the source and drain electrodes (tuned by the gate electrode), tunneling events from/to the island take place.

Therefore, a plain SET cannot be employed as a device for generating quantized current. However, the existing implementations of such devices either are built upon a modified version of an SET or use a core part of it. In the following, some of these implementations will be introduced and discussed in rough chronological order.

2.2 Geerligs device

One of the early implementations was presented by Geerligs et al. in 1990[8]. Similar to the devices discussed above, it requires a small source–drain voltage to operate. As illustrated in Fig. 2.3(a), the central part of the device resembles an SET. This central SET is extended by additional tunneling junctions. The two extra islands, if charged by a single electron, control the current flow through the central SET. This setup ensures a one–by–one electron transport through the device even if the central SET is in the on–state. If the gate voltage is modulated by a high frequency source then a quantized current is generated, as can be seen in Fig. 2.3(b).

Figure 2.3: Geerligs turnstile device

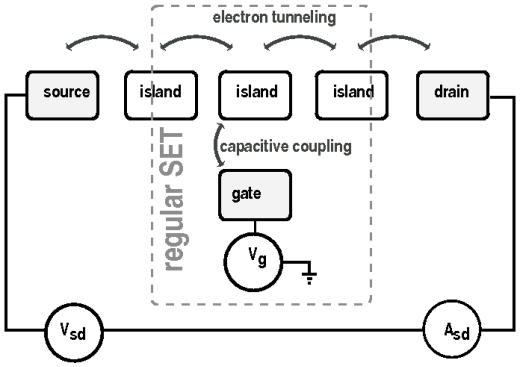

(a) Geerligs turnstile device scheme. The central part resembles an SET (Fig. 2.1). Additional island regulate the electron tunneling through the central SET such allowing quantized currents.

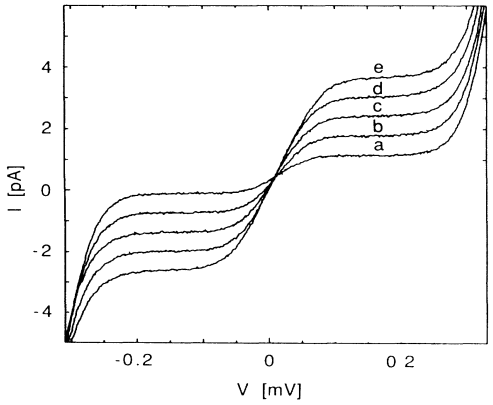

(b) Quantized current generated by the Geerligs turnstile device (for different frequencies) by Geerligs[48].

2.3 Kouwenhoven device

The setup presented by Kouwenhoven et al. in 1991[9] makes use of a slightly different approach and does not employ additional static structures. Instead, it can be seen as a single island, possessing tunneling barriers with tunable height.

Fig. 2.4 illustrates the working principle of Kouwenhoven's device. The central island is separated from the leads by tunneling barriers, the height of which can

Figure 2.4: Operation cycle of Kouwenhoven's pumping device

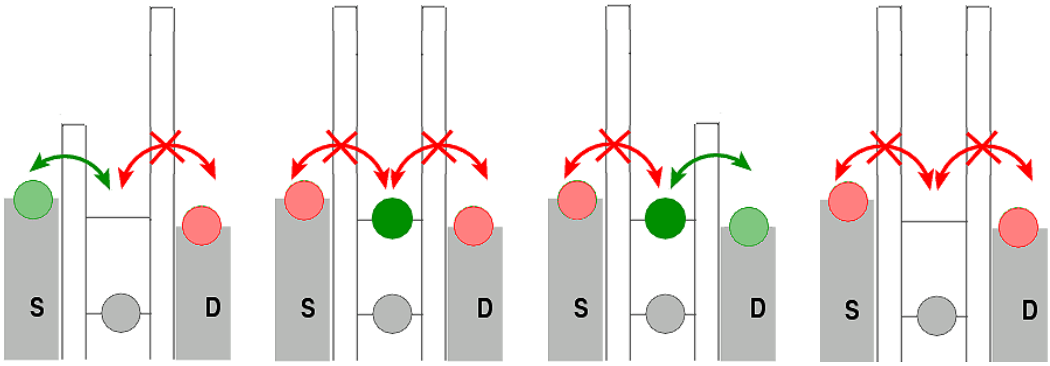

(a) Charging of the quantum dot (QD)

(b) Charged QD

(c) Discharging of the quantum dot

(d) Discharged QD

be modulated by an applied voltage. At the beginning of the cycle both barriers are sufficiently high to suppress any tunneling events from and to the island. An applied RF signal can lower the barrier such allowing the electrons to tunnel. If the phase of RF signals applied to both tunneling barriers differ by π, it is possible to allow the electrons to tunnel consecutive from the source lead to the island and from the island to the drain lead[49]. Therefore, applying a small source–drain voltage results in a quantized net current according to the relation (2.1).

2.3.1 Drawbacks of the Geerligs and Kouwenhoven devices

Albeit functioning, the approaches presented above have serious experimental disadvantages which prevent these implementations to satisfy high metrological requirements. Sufficiently high accuracy it given only if exactly one[1] electron is transferred in each working cycle. However, to ensure the tunneling of an electron through a barrier some finite time must be spent. Therefore, the operation frequency of devices described so far is limited to several MHz if accuracy requirements are to be met. As a consequence of this limitation achieved currents can be only as high as few pA. So far the highest accuracy (15 ppb) was achieved by a serial arrangement of 7 devices similar to the Geerligs device [10, 50] (see Fig. 2.5). However, while this accuracy is sufficient for a metrological standard, the current produced by this pump is as low as 1 pA.

[1] or any other well defined number of electrons

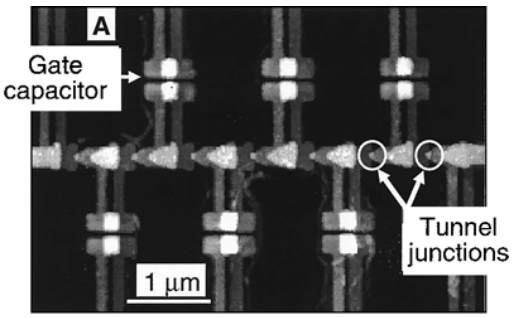

Figure 2.5: A 7–junction electron pump. This arrangement allows an accuracy of 15 parts in 10^9 at 5 MHz pumping frequency (by Keller et al.[10, 50])

2.4 Surface acoustic wave charge pumps

These limitations gave rise to an alternative approach, involving surface acoustic waves (SAW). In analogy to light, which is a combination of electric and magnetic waves, SAW in piezoelectric materials combine a mechanical longitudinal wave with an electrical transversal wave (more on the nature and properties of SAW can be found in the Appendix A). Approaches described below make use of the electrical part of SAW.

2.4.1 Charge pumps based on 2DEG

Fig. 2.6 shows a typical device scheme used for generating quantized current by SAW. The substrate is usually based on GaAs and fulfills two functions. Being a piezoelectric material it conducts SAW generated by the transducers $T_{1,2}$. A GaAs-based heterostructure also provides a specific electron configuration known *as 2–dimensional electron gas* (2DEG, see for example Weis[45]). In a 2DEG, electrons are free to move in x– and y–direction only, being restricted in the z–direction. The electrostatic potential within the 2DEG can be shaped by electrodes lying on the surface. Applying negative voltage to these structures called *split–gates* (G_{1-3} in Fig. 2.6) depletes parts of 2DEG from electrons.

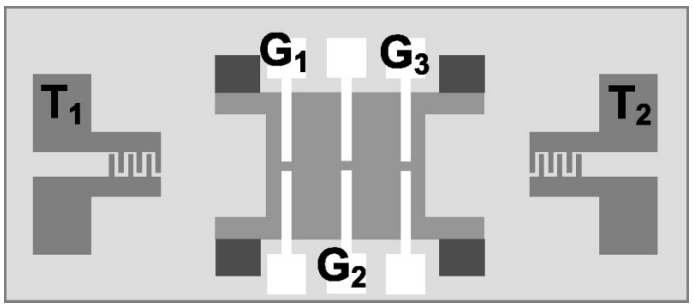

Figure 2.6: Scheme of the SAW based quantized charge pump[51]

Figure 2.7: Operation principle of the quantized charge pump driven by SAW by Shilton et al.[14].

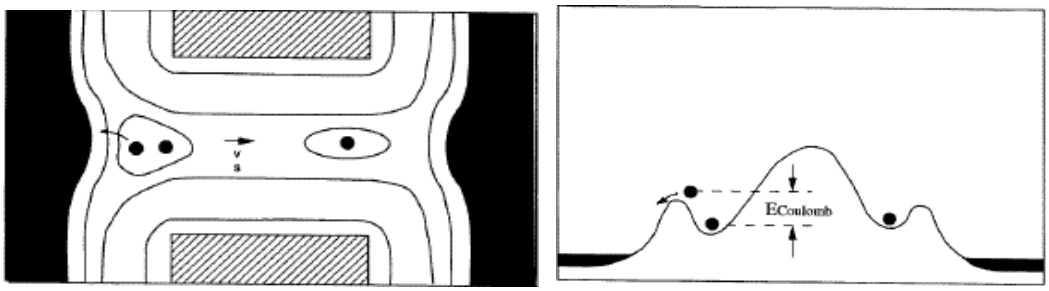

(a) top view of the potential landscape (b) side view of the potential landscape

The 2DEG within the split–gate is depleted to form an one dimensional channel with a length of some hundred nanometer. Inside of this channel electrons are confined within moving quantum dots, defined by SAW potential minima (see Fig. 2.7). By choosing suitable parameters it is possible to generate a quantized current. This approach underwent an extensive investigation by both experimentalists and theoreticians[14, 51–64]. As the SAW can be generated with frequencies of several GHz, the resulting current is high enough to serve as metrological standard. Indeed, quantized currents close to 1 nA have been generated. However, the accuracy of this pumping mechanism is severely limited due to non adiabatic processes taking place during the pumping. This is caused by the fact, that the exact electrostatic potential of each moving dot is changing as it travels through the split–gates. This makes it difficult to keep a well defined number of electrons in each cycle. Also, the tunneling coupling between the electron gas and the moving dot rapidly decays with time. These processes limit the accuracy of the quantization achieved with SAW devices to a value of 10^{-2}–10^{-4}[62].

2.4.2 Charge pumps based on carbon nanotubes

As introduced above, coupling of surface acoustic wave to low dimensional electron systems is a well–known principle for a quantized charge pump. However, the quantized charge pumping based on a SWNT, as proposed by Talyanskii et al.[36] in 2001 was a novelty (see Fig. 2.8). While conventional SAW–pumps would also benefit from high charging energies of carbon nanotube quantum dots, the motivation to use the SWNT was different.

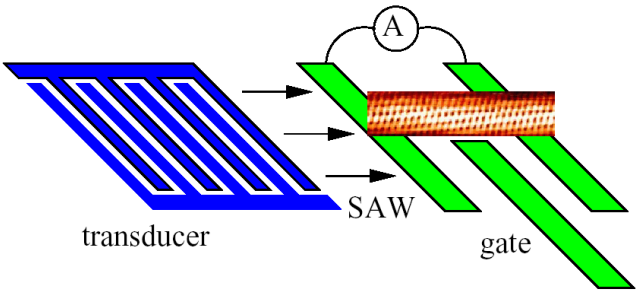

Figure 2.8: Scheme of the proposed SWNT based SAW adiabatic pump[65]

The electronic properties of SWNTs, such as ballistic transport and Luttinger Liquid behaviour combined with high electron density, opened the prospect of experimentally reaching the regime of *quantized adiabatic quantum pumping*, a novel effect, which has been predicted by Thouless[44]

Proposal for an SWNT based adiabatic quantum charge pump

It is characteristic for *quantum pumps* that the periodic deformation of the confining potential slowly changes the *wave function of the system*. One speaks of *adiabatic quantum pumping*, if the deformation of the confining potential of the mesoscopic system in question is slow on the relevant scale, i.e the dwell time of an electron within the dot. The wave function extends into the leads and transports charge to or from the reservoirs through the changes of the confining potential. This principle does not require the quantum dot to be well–separated by the leads and does not rely on Coulomb blockade, as in case of Geerligs and Kouwenhoven devices. Indeed, current pumping was shown by Switkes et al. in 1999[66] on the *open dot*, i.e. a structure well–coupled to the leads.
Under certain circumstances current generated by adiabatic quantum pumps can be also *quantized*. The regime of the quantized adiabatic quantum pumping is predicted to be insensitive to disorder and many–body interactions. This results in a very high accuracy[67]. There are similarities to the quantum hall effect, which produces highly accurate (10^{-8}–10^{-9}) results on less–than–perfect devices due to its topological nature[68]. The quantized adiabatic charge transport is expected to generate highly accurate currents for same reasons[69, 70].
The figure 2.9 shows the electron energy spectrum of an SWNT acting as an one–dimensional conductor in a adiabatic periodic potential of the form

$$V(x,t) = A\cos(kx - \omega t)$$

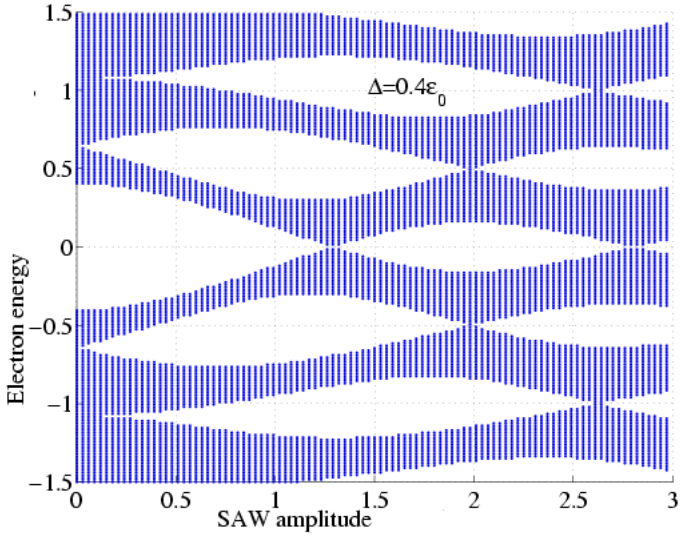

Figure 2.9: Energy spectrum calculated for an SWNT in a periodic SAW–induced electrostatic potential shows numerous minigaps (Talyanskii et al.[36]) . Quantized current is generated if the Fermi level lies within such a minigap

as generated by SAW[36]. Several minigaps open within this spectrum. Thouless showed that if the Fermi level is within such a minigap, the amount of charge transferred during a pumping cycle is quantized and follows the relation

$$I = n \cdot e \cdot f.$$

Reported results on SWNT based current pumps

Figure 2.10: Observations of SAW induced quantized current in SWNT

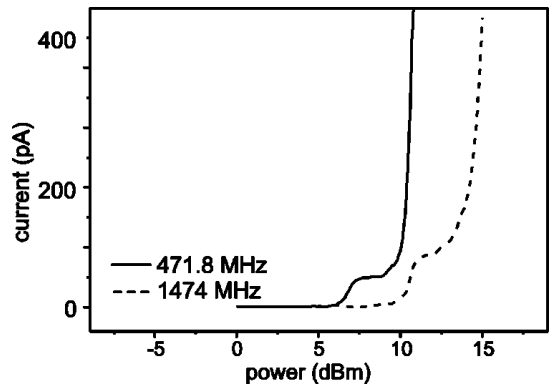

(a) By Ebbecke et al. in 2004[71]

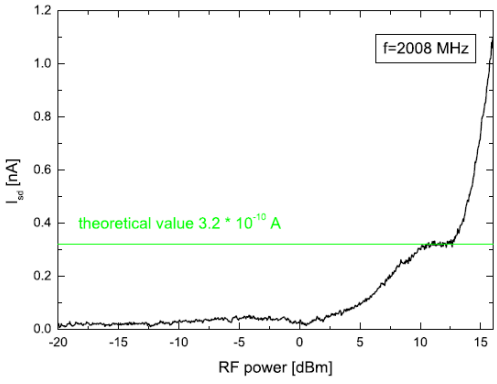

(b) By Würstle et al. in 2007[39]

Recently, two groups reported experimental progress in the SAW induced charge pumping in carbon nanotubes. Ebbecke et al.[71] reported in 2004 quantized charge pumping on carbon nanotubes. The nanotubes were dispersed on $LiNbO_3$

and subsequently contacted. The quantization was observable for both frequencies available with the device (the primary frequency of 475 MHz and the third harmonic[1] at 1425 MHz; all reported measurements were conducted at liquid helium temperature). While a reproducible current quantization could be observed (Fig. 2.10(a)), its value did not correspond to the expected value given by the relation $I = e \cdot f$.

The distance between the SWNT contacts was chosen to be 2 µm, which corresponds to $\lambda_{SAW}/4$ at the frequency of 475 MHz. Hence, the SAW modulated the barriers to the SWNT-QD in analogy to the Kouwenhoven device. Quantized charge pumping – based on the same principle – was reported by Würstle et al. in 2007[39] (using a similar fabrication method, see Fig. 2.10(b)) and by Leek in 2006[72] (on quartz in a metallic CVD–grown nanotube).

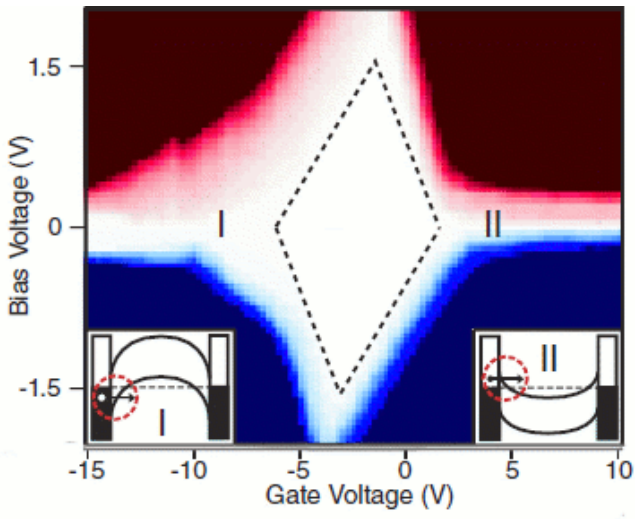

Figure 2.11: Current induced by SAW in a semiconducting SWNT as reported by Leek et al.[38]. (Red and blue colors correspond to positive and negative current, respectively)

Leek et al.[38] reported in 2005 also non quantized charge transport induced by SAW. It was observed in a semiconducting SWNT grown by CVD on a quartz substrate. The sign of pumped current could be modified by gate voltage applied at the SWNT as illustrated in Fig. 2.11. The data interpretation is illustrated in Fig. 2.12. According to this model, SAW creates an electric field at the interface between the metal contact and the nanotube. This bends the band structure allowing injection of selectively electrons or holes, depending on the sign of the gate voltage applied at the carbon nanotube.

[1] For more information on SAW generation of higher harmonics see also Appendix A.2 on page 91

Figure 2.12: The SAW packet transport model proposed by Leek et al.[38]

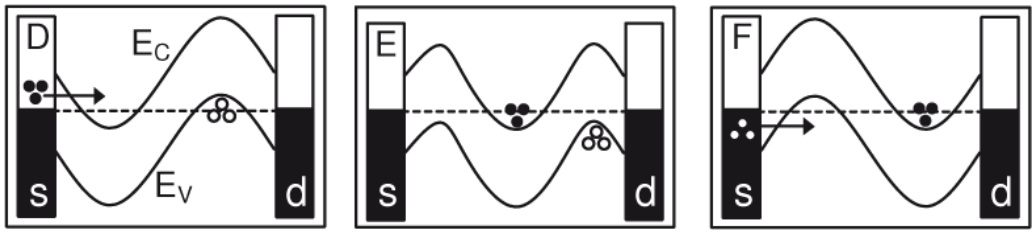

2.5 Quantized current by local gating

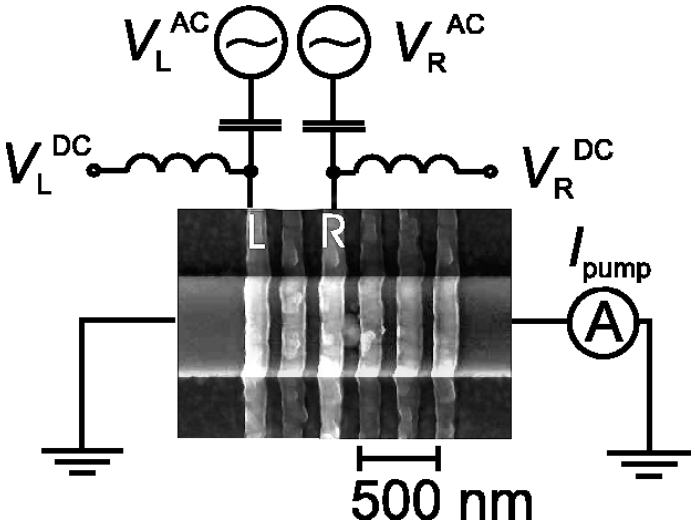

Figure 2.13: Scheme of the locally gated current pump by Blumenthal et al.[12]. The SEM micrograph shows the etched channel (horizontal) acting as 1D–conductor and several local gates (vertical). Two of them are denoted as (L)eft and (R)ight.

The dilemma of having either high current at the expense of the accuracy or vice versa made it necessary to look for new approaches. One of them is based on shaping of the electrostatic potential along an one–dimensional ballistic channel by applying voltage at locally acting gates. It was reported in 2007 by several authors[12, 73, 74]. The device scheme and its operation principle are illustrated in Figures 2.13 and 2.14. Its implementation involves a quantum wire, etched out of GaAs/Al-GaAs 2DEG, and two top gates labeled as *R* and *L* in Fig. 2.14. The voltage at the gate *R* is chosen so that the quantum wire beneath the gate is depleted of electrons at all times. The RF signal is applied to the gate *L*. During the cycle a quantum dot is formed loading electrons from the left part of the device and unloading them to the right. As no bias voltage is needed for the operation of this device, one obtains a quantized charge pump generating current at frequencies as high as several GHz and an accuracy of 10^{-4}[12]. Higher accuracy is expected for devices with higher charging energy, which can be achieved

Figure 2.14: Operation principle of the locally gated current pump. Main stages of the time–dependent potential as seen by individual electrons in the channel.

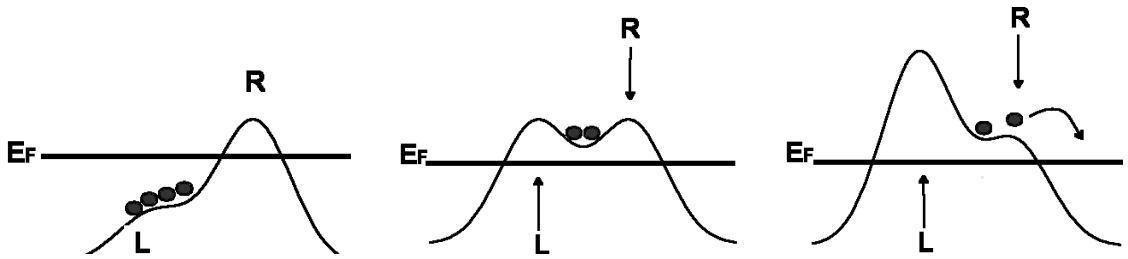

(a) The potential at L increases forming a quantum dot. The potential hill at R keeps its height at all times.

(b) The potential at L matches the potential at R. A quantum dot capturing electrons is developed.

(c) The potential at L is so high that the QD tilts to the right. The electron transfer is completed.

by decreasing the width of the quantum wire from currently several hundreds of nanometers to a much smaller value. Alternatively, several of these devices can be connected in parallel to increase the overall output current while low pumping frequency ensures a high value of accuracy.

2.6 Hybrid superconducting–normal conducting design

In 2008, Pekola et al.[43] reported a realization of another device type for generating quantized charge current. It comprises an SET combining superconducting (S) and normal conducting (N) materials (Fig. 2.15). Due to this combination it is known as *hybrid device*[43, 76]. Its principle of operation involves not only the electron–electron interaction governing the energy quantization on a small island but also features of the S–N interface. Both NISIN (normal conducting leads separated by an insulating layer from a superconducting island[43]) and SINIS configuration[75] were shown to generate quantized currents.
The latter is depicted in Fig. 2.15(a), where a small Cu–island is contacted by Al–contacts. In the superconducting state the charge carriers condense as *Cooper–pairs* below the the Fermi energy (for introduction in superconductors see[77, 78]). These states are separated from the higher energy states by the energy gap 2Δ, where Δ is the superconducting (BCS) band gap. In these states electrons can exist as individual particles (so called *quasi–particles*). At low temperatures the

Figure 2.15: The hybrid device[43, 75, 76]

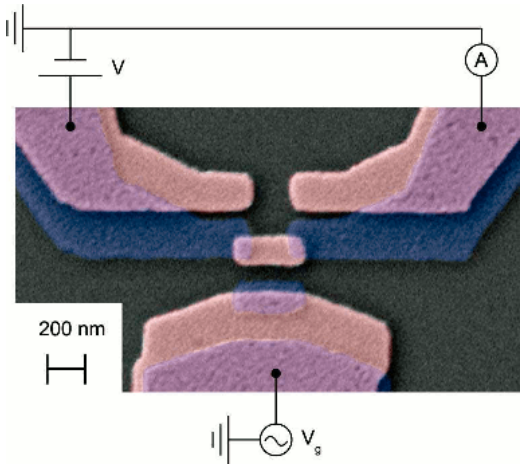

(a) The SEM picture of the all–metal SINIS hybrid device with superconducting leads (Al, barely visible grainy metal) and normal conducting island (Cu, bright metal). Aluminium oxide between these metals act as the tunneling barrier.

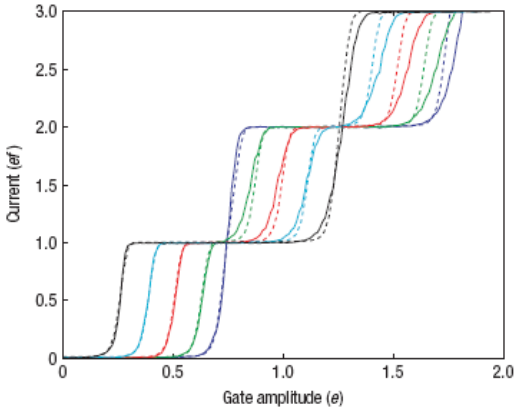

(b) Quantized current produced by the (NISIN) hybrid device[43] in units of elementary charge as function of gate amplitude (Measured for different d.c. gate voltages at 20 MHz)

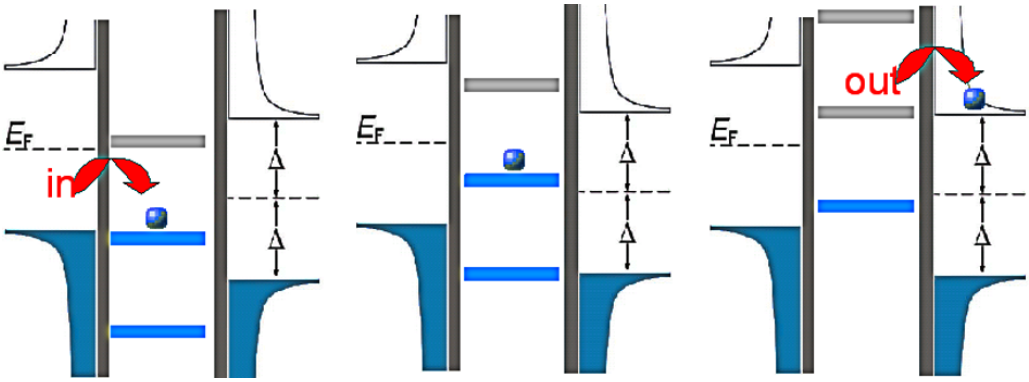

(c) SINIS device working principle. The density of states in the superconducting leads is is zero for $E_F \pm \Delta$, where E_F is the Fermi energy and Δ the superconducting gap. At low temperatures the states below the gap are fully occupied, while the states above the gap are empty.

states below the gap are almost perfectly occupied, while the states above the gap are empty.

Fig. 2.15(c) depicts the operation principle of the SINIS device. Essentially it comprises a 'regular' SET, yet with superconducting leads. Analogous to the normal SET, a small source–drain voltage V_{sd} is applied over the device and the energy states of the central island can be shifted by a nearby gate. The island is charged by a single electron when one of its available energy states is aligned with the Cooper pair state of the source lead. The island is discharged, when the occupied state is aligned with the quasi–particle state.

The band gap effectively suppresses tunneling effects for $V_{sd} < 2\Delta/e$. In contrast to the normal conducting (NININ) SET, this configuration allows a precise and controllable one–by–one electron transfer necessary for the quantized current generation. It is important to point out that a fully superconducting (SISIS) device could not provide the necessary quantization condition neither. Here, Josephson effect would cause superconducting currents with no applied bias. The hybrid SIN interface is therefore vital for this device type.

The function of the BCS band gap is illustrated by the stability diagrams[1] in Fig. 2.16. The pumping is schematically depicted for different configurations of the SET. For the regular (NININ) SET the stability regions of the states for charged ($n = 0$) and uncharged ($n = -1$) island are barely touching each other. The pumping signal (the thick red line) passes an area outside the stability regions, which results in an uncontrollable current through the device. However, the stability regions of the regular SET are extended in the hybrid device by the magnitude of the BCS band gap. Consequently they overlap, such forming a bi–stable configuration (charged/uncharged island) which allows a controlled charge transfer and quantized charge pumping.

One of the main advantages of the hybrid design is that it allows quantized charge pumping with a single island and a simple design. A pump with several islands (as reported by Keller et al. in 1996[50] and shown in Fig. 2.5) requires considerable engineering and experimental effort. Also the operation frequency is lowered by the high number of junctions. The hybrid design on the other hand could easily allow to employ several devices in parallel, such achieving much higher currents[2].

[1] More on the topic of single–electron transport and stability diagrams can be found in the appendix B.3 on page 95

[2] Kemppinen et al.[75] estimates that compared to the serial N–island pump (Fig. 2.5) hybrid design can provide roughly N^2 times higher currents while keeping the same amount of complexity

Figure 2.16: Schematic picture of pumping with different SET configurations. The coloured diamond–like areas are the stability regions of charge states $n = 0$ (charged island) and $n = -1$ (uncharged island). The lines represent the transition thresholds from these states by tunneling through left (L) or right (R) junction in (wanted) forward (F) or (unwanted) backward (B) direction. The thick red line corresponds to pumping with $V_{sd} = \Delta/e$. $n_g = C_g V_g/e$ is the amount of charge induced on the island by the gate. All energies are normalized in Δ respective in E_c, all charges are in units of e (from[75]).

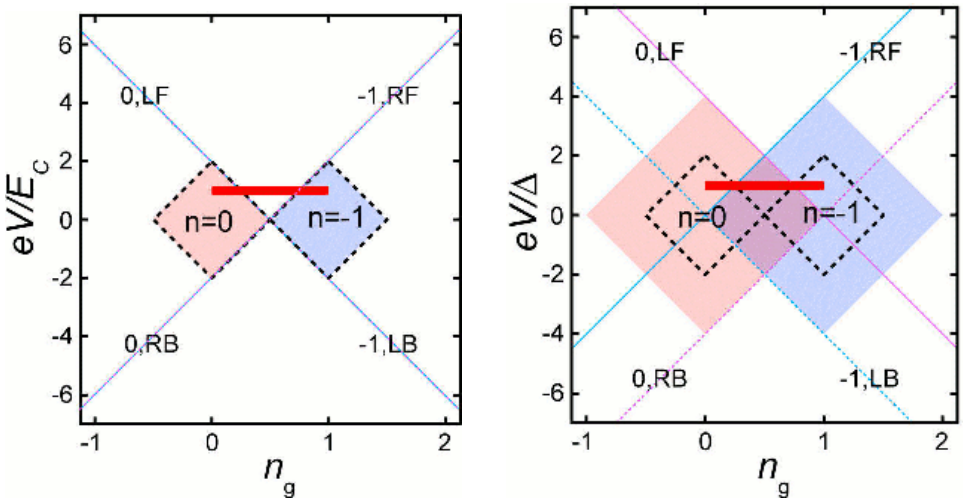

(a) Regular (NININ) SET

(b) Hybrid SET with equal charging and BCS gap energies

The accuracy of the hybrid device is predicted[43, 76] to be sufficiently high to fulfill the metrological requirements of generating quantized current in the order of 100pA at an error rate of 10^{-6}–10^{-8}. The main way of reaching this goal is (besides from optimization of the experimental parameters, such as using a rectangular signal shape) to obtain devices with ratios $E_c/\Delta > 10$. This property ensures suppression of higher–order processes (such as multiple Andreev reflection), which are the source for errors in the turnstile operation. As Δ is given by the superconducting contact material, this effectively requires fabrication of islands with charging energy of several milli-electron volts . The feasibility of such devices has been shown [40, 79], however linked with significant technical challenges.

Chapter 3

Experimental Details

3.1 Sample Preparation

3.1.1 Fabricating SWNT Devices – General Remarks

Top–down approach Many devices used to study the physics of low–dimensional system are usually fabricated in a so–called *top–down* approach. Here the properties of the material are defined during a technological process[1] resulting in a macroscopic amount of the material in question. This material is shaped and modified using a various number of techniques[2]. These techniques result in a microscopically small device, which is used for the actual investigation.
But however long a SWNT might be, it is still just *one single molecule*. Despite of huge interest and some encouraging reports[22, 80] it is still not possible to produce an individual SWNT on a length scale of several centimeters. Hence the *top–down* approach described above cannot be applied for the fabrication of SWNT devices.
While the *top–down* approach has proven itself, there is always a size limit down to which the structures can be modeled. Even though this limit is continuously pushed down by technical development, the imposed restrictions for the research on mesoscopic structures (e.g. SWNT) are substantial. To solve this problem a complementary approach is used.

Bottom–up approach In the so–called *bottom–up* approach the devices are not fabricated by shaping the matter with the tools and techniques described above. Instead the experimentalist rely on the fundamental interactions occurring on molecular and sub–molecular level. If chosen carefully, components and processes result in spontaneous organization of molecular or atomic structures, which properties can then be studied.
This approach involves several processes known from chemistry and material research, such as *Langmuir–Blodgett–films*, *self–assembled monolayers*, *chemical vapour deposition* (CVD) and MBE, which are widely used and are of great value.

[1] This could be purification of metals or semiconductors; doping of semiconductors, fabrication of heterostructures by the *molecular beam epitaxy* (MBE)
[2] Commonly used techniques are: optical and electron beam lithography, thermal and electron beam evaporation of thin films, various wet, dry, and plasma assisted etching processes

On the downside, these processes are more stochastic and erratic than the processes known from the macroscopic world. The outcome of an technological step can be predicted only statistically and not for each device individually.
SWNT, being a truly mesoscopic system, requires understanding and applying not only the features of the *top–down* approach but also of the *bottom–up*. While this is true for any mesoscopic system (e.g. 1D–whiskers or graphene nanoribbons), the SWNT have an additional characteristic. The electrical properties of a SWNT are very sensitive to its diameter and helicity. However, there is currently no possibility of controlling these properties. This introduces an additional uncertainty element in fabricating a device with specific characteristics.
Summing up, one can say that since their discovery SWNT have not lost anything of their exciting nature.

3.1.2 Device fabrication using the SWNT suspension

The three main ways of making SWNTs rely on obtaining carbon vapour in a catalytic environment, which would allow formation of SWNT. Out of these three, only with the chemical vapour deposition (CVD) method it is possible to place SWNT on predefined positions of a chip directly during their synthesis. This approach is both technologically challenging and promising and is often used for achieving high quality SWNT devices[81–83]. The usability of this approach for the fabrication of SWNT based quantized charge devices was also investigated within this work.
Devices used in the course of this work were fabricated using a different approach, which is also used very often for SWNT–devices. Here, the individual carbon nanotubes are brought into a suitable suspension to be absorbed on the surface of the substrate.
The carbon material is produced by *arc–discharge* or *laser ablation*. In both cases graphite is vaporized at temperatures around 2000 °C. Under the influence of the catalyst carbon atoms form a mixture of different carbon allotropes such as fullerenes, amorphous carbon, and various types of CNT. Typical source material for the experiments conducted during this work is illustrated in Fig. 3.1(a).
In order to obtain individual single walled nanotubes, several steps are needed. First of all, a stable suspension of carbon nanotubes has to be prepared. In the second step individual SWNT are extracted by centrifugation. Consequently,

Figure 3.1: Source SWNT material for this work

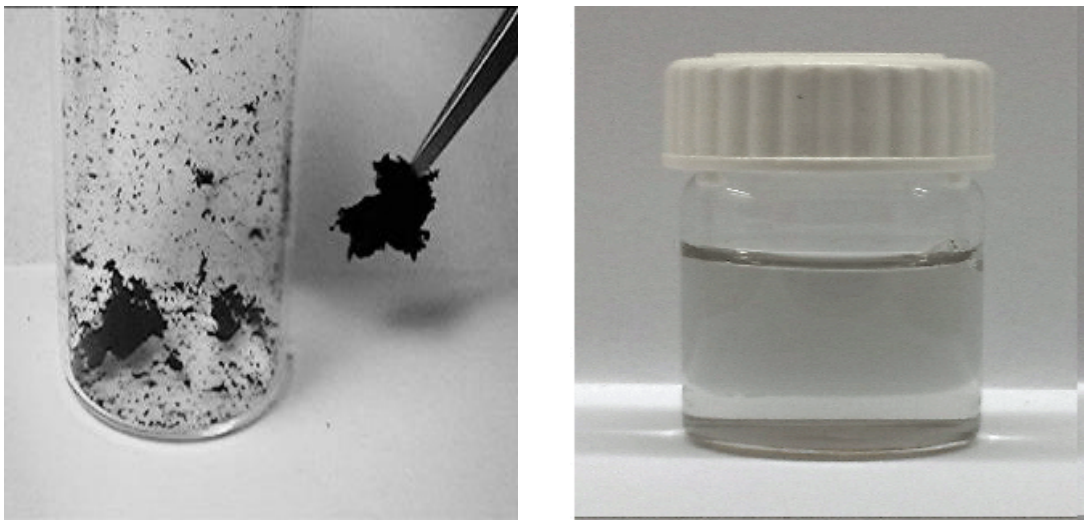

(a) Raw CNT material

(b) A ready-made SWNT suspension in an aqueous SDS solution

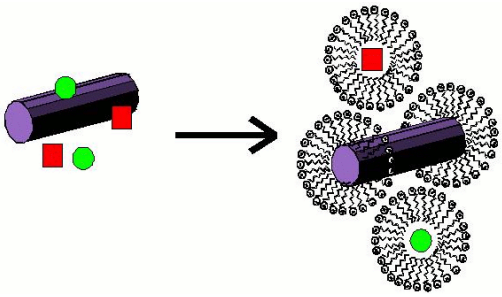

Figure 3.2: Preparation of the suspension of carbon nanotubes in a SDS solution. The first step is the separation of individual parts in the raw CNT material by the ultrasound. In the second step the long–chain SDS molecules surround the particles, which results is a stable suspension. Adapted from [84].

these nanotubes are adsorbed on the substrate and are ready for further processing. The results of the adsorption can be modified by an additional surface modification. Below, these steps are described in detail.

Preparation of the SWNT suspension Deionized water is often used as the base for SWNT suspensions. A small piece of the CNT–material (after optional chemical purification) is put into deionized water. The dispersion of the CNT–material is achieved by ultrasonication where the energy deposited by the ultrasound rod is pulling the carbon conglomerates (consisting of individual and bundled CNT, amorphous carbon and catalyst rests) apart[1]. However, as carbon-

[1] At the same time the ultrasonication is known to introduce additional defects to CNTs which effectively leads to cutting of CNTs

atious material is hydrophobic, large agglomerates form after a very short time. Therefore, a stable suspension of individual SWNT is obtained by using suitable surfactants.
Commonly, the sodium dodecyl sulfate (SDS, $C_{12}H_{25}NaO_4S$) molecule is used[85]. It has a hydrophilic part (Na^+) and a long hydrophobic tail. For our purpose a 1 wt% solution of SDS was used. It surrounds separated particles (Fig. 3.2), which results in a stable suspension. The separation of catalyst particles, amorphous carbon and (individual) carbon nanotubes is done by centrifuging.

Extraction of individual SWNT by centrifugation When needed, the original SDS suspension was centrifuged at 14000 RPM for 30 min to separate the (light) SWNT from (heavy) bundles, amorphous carbon and catalyst particles. After centrifuging the upper part of the suspension was used for adsorption. This procedure was repeated until satisfactory results were achieved. An example of resulting SWNT suspension is shown in Fig. 3.1(b).

Chip surface modification On some surfaces it can be necessary to modify the surface chemistry in order to obtain better adsorption and/or better selectivity for SWNTs. For SiO_2 this can be achieved by creating an additional surface layer, for example by a water solution (1:1000) of N-[3-(Trimethoxysilyl)Propyl]-Ethylen-Diamin (97%) [86, 87]. This additional step, known as *silanization* greatly increases the number of adsorbed nanotubes[1].
For this work also other substrates were used, such as quartz and lithium niobate ($LiNbO_3$). Materials with different surface chemistry might require different silanization processes. As quartz is chemically strongly related to the thermally grown (amorphous) silicon dioxide on the silicon chips, the same silane could be applied. However, for $LiNbO_3$, appropriate silanes need to be chosen. Good results were obtained by using (3–Aminpropyl)–triethoxysylan (99%). Examples of adsorbed SWNT are shown in Fig. 3.3.

Adsorption and selection of suitable SWNT Suspended tubes were adsorbed on the chip either by putting on its surface a droplet of the suspension or by dipping the chip into it. After this the chip was blow dried to remove the suspension. The density of adsorbed CNTs on the surface was controlled by adsorption time and

[1] A similar result can be obtained if instead of silane a layer of Al_2O_3 is used [88]

Figure 3.3: Results of the SWNT deposition from a suspension on different substrates. The density of adsorbed nanotubes can be controlled by the time the substrate and suspension stay in contact.

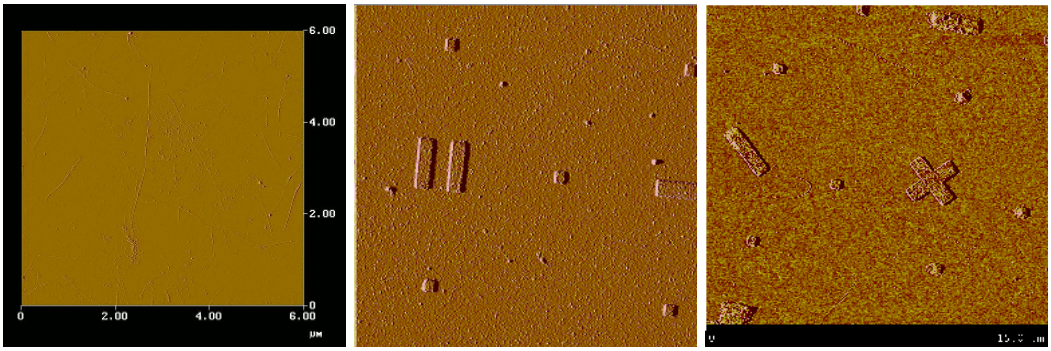

(a) $LiNbO_3$ (b) Quartz (the small squares have the dimensions of 500 nm×500 nm) (c) Si/SiO_2

monitored by *atomic force microscopy* (AFM) imaging. With some experience this very simple technique allows to obtain desirable results.

After adsorbing the nanotubes onto the chip surface it is necessary to locate and select the most promising candidates for successfully operating devices as precisely as possible[1].

As the nanotubes used in this work were usually only 1–1.5 nm thick, a method was required which reliably allows for resolving objects in nanometer scale. Among several existing techniques (such as *scanning electron microscope* SEM or *near field optical microscope* NFOM), the AFM has the benefit of working in ambient environment providing excellent resolution in sub–nanometer range[2]. These properties make AFM the type of microscopy often employed in the fabrication of CNT–based devices (an overview on AFM is given e.g. in [86]).

As the wafers of piezoelectric materials do not have a sufficiently smooth surface they need to be polished for further processing. Otherwise, the scratches left after

[1] In the beginnings[41] it was common to either randomly place contacts on top of suspended networks of CNTs or (randomly again) adsorb CNTs on top of predefined contacts. The experience showed however that with increasing demands towards more reproducibility, device characteristics, and device complexity this randomized approach is reaching its limits.

[2] This is valid at least for the z–direction. The lateral resolution in x– and y–directions are typically much lower. The consequence is that while it is possible to determine a diameter of a SWNT, it is very hard to exclude the possibility of two thin nanotubes running alongside or partly overlapping each other[89]

individual wafers were cut from the ingot make the location of adsorbed SWNT difficult.

3.1.3 Chip characteristics

Silicon chip The silicon based chip has become a *de facto* standard for DC–measurements on carbon nanotubes. The silicon is highly doped and therefore electrically conducting down to cryogenic temperatures. Thermally grown SiO_2 (200 nm thickness) on top of silicon is on the other hand insulating. The back side of the chip is metalized, allowing a good electrical contact. Hence, if voltage is applied at the back side, the silicon acts as a global gate and SiO_2 as the dielectric. This setup is widely used to investigate and implement SWNT–based devices such as transistors and diodes (see e.g. [90]).

Piezoelectric chips An important feature of presented work is the behaviour of SWNTs under the influence of high frequency electric fields. This can be implemented by several techniques. One possibility is to generate *surface acoustic waves* (SAW, see Appendix A on page 89). As SAW require piezoelectric materials, silicon based chips cannot be used. During this work the use of lithium niobate ($LiNbO_3$, yz–cut) and quartz (36° rotated y–cut) as substrate for SWNT–based devices was investigated.
An issue arising from using substrates other than the highly doped silicon is the lack of a global back gate. As both quartz and $LiNbO_3$ are bulk insulators, devices can be gated only by side or top gates, which might involve additional fabrication steps.

3.1.4 Contacting of SWNT

Contact Patterning All chips had in common predefined structures fabricated by xLith GmbH in the case of silicon chips and by Physikalisch–Technische Bundesanstalt in Braunschweig (PTB) in the case of piezoelectric chips. These structures provided metal leads which were used later for contacting the nanotubes. They also act as a system of markers (see Fig. 3.3(c)), which allows to localize a specific carbon nanotube for each of the necessary fabrication steps.

After the deposition on the substrate and the AFM selection suitable contacts to SWNT were patterned by means of standard *electron beam lithography* (EBL) (a detailed description of this step is given in e.g. [87, 91, 92]).

Figure 3.4: Wetting behaviour of some metals on SWNT (by Zhang and Dai[93])

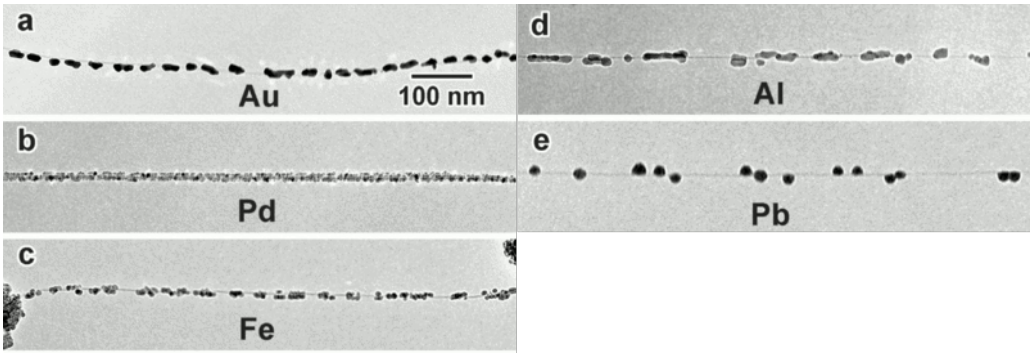

Contact Metalization After the lithography contacts to carbon nanotube were fabricated by evaporating or sputtering of various metals. The choice of the contact metal has a direct consequence on the nature of the electrical contacts[1] . One of the reasons is the wetting of the surface of a SWNT by the specific metal during the evaporation. The second is the Schottky barrier at the interface between the metal contact and a semiconducting carbon nanotube.

Wetting behaviour of different metals As illustrated in the introductory part, SWNT is basically all surface and no bulk. Therefore, surface effects are ubiquitous when dealing with nanotubes especially in the process and nature of the tube–metal interface.
An obvious example is wetting of SWNTs by different metals as shown in Fig. 3.4. While some metals and alloys form a continuous film, others tend to form clusters. When dealing with small dimensions as in the case of SWNT, this might lead to a contact interface which consists of a number of point contacts. Usually this results in a low reproducibility of contacts and a high contact resistance.

Schottky barrier and doping of SWNT by contact metal At the interface of a semiconducting nanotube and the metal contact additional effects occur. Caused

[1] An optional post processing step, such as annealing, is also known to have a certain influence on the quality of some SWNT–metal contact[92, 94–96]

by the difference in work function of SWNT and the metal, the band structure of the nanotube bends (Fig. 3.5), creating a tunneling barrier. This phenomenon is known as the *Schottky barrier* (see e.g. [27]. This tunneling barrier can significantly increase the contact resistance of the SWNT–device. Moreover, a doping of the carbon nanotube caused by the contacts can be observed in gate–dependent measurements, as illustrated in Fig. 3.6.

Figure 3.5: Schottky barrier at the SWNT–metal interface (from Liang[91]). The exact value of the work function in SWNT (≈4.5–5.5 eV[97]) depends on diameter and chirality (more information is provided by[98–100]; also see the discussion of nanotube/metal contacts in[19])

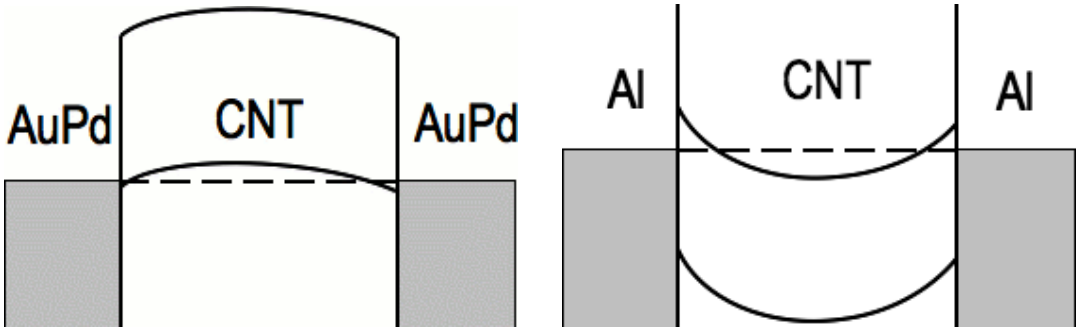

(a) High work function of AuPd (5.4 eV) cause p–doping of SWNT

(b) Aluminium contacts (work function 4.1 eV) results in n–doping

Contact resistance Theoretically[17, 23], the resistance of a well–coupled metallic nanotube equals to

$$R_K/4 \approx 6.45k\Omega, \tag{3.1}$$

where 4 is the number of conducting channels (two modes carrying two spins each) in a metallic SWNT[104]. The resistance originates solely from the contact resistance as the carbon nanotube is able to carry electrical current with no scattering and losses (so–called *ballistic transport*[1] [105]).
The experimentally achievable resistance is usually much higher than predicted by relation (3.1). As mentioned above, this is partly caused by poor metal wetting and Schottky barrier. Additional tunneling barriers can also be introduced by organic

[1] The assumption of a ballistic transport in a SWNT is valid only for low currents[91].

Figure 3.6: Doping of carbon nanotubes by contacting with different metals

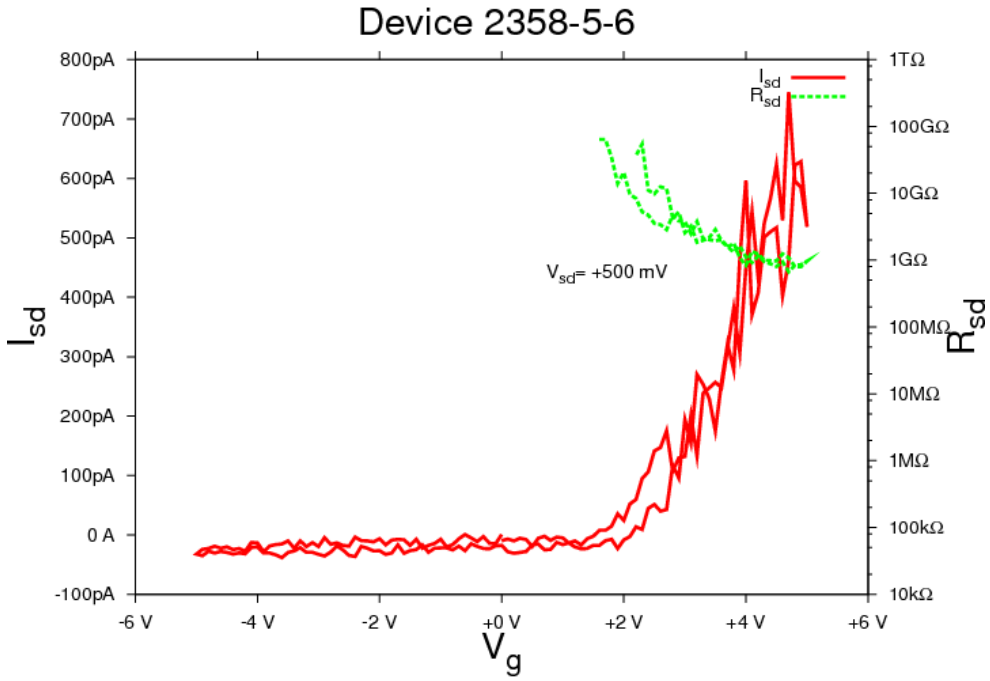

(a) n–doped behaviour after contacting by aluminium (T=300 K)

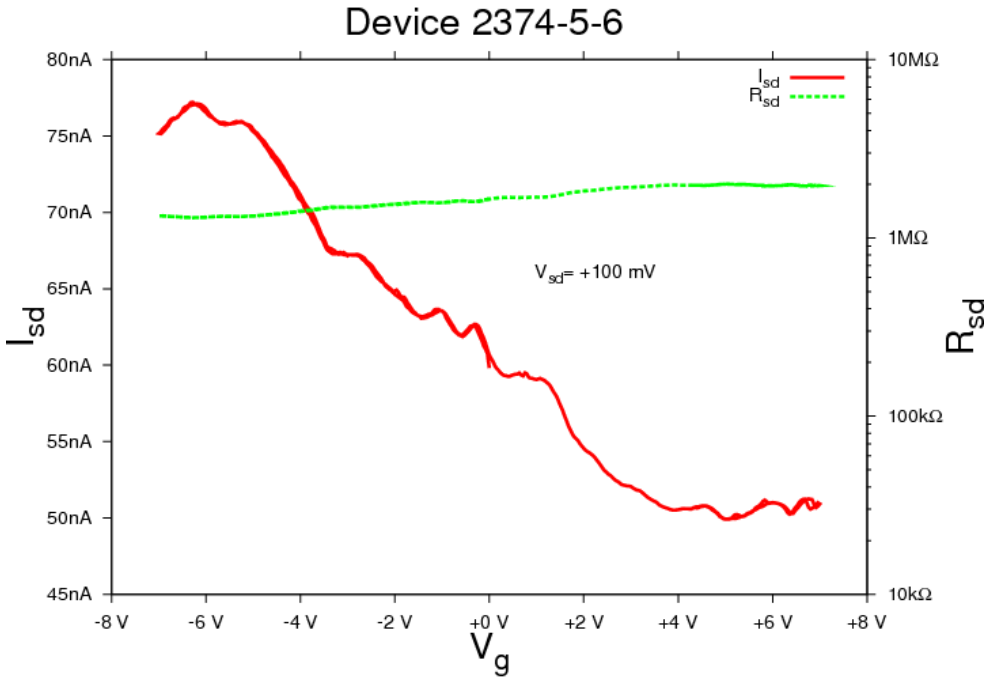

(b) p–doped behaviour after contacting by a layered NbTi (5 nm Ti followed by 30 nm Nb) contact (T=4.2 K). More on work function of Ti in [101, 102]

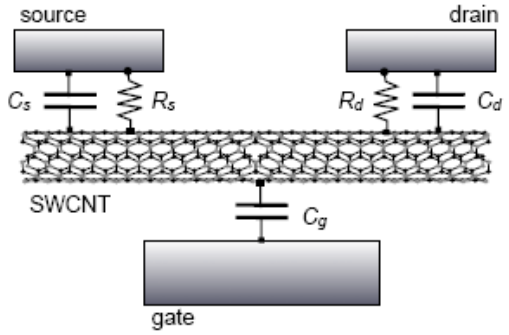

Figure 3.7: A schematic equivalent circuit of a SWNT–based transistor (from Yao[103]). This is also the device type used in this thesis. The gate electrode is coupled purely capacitively (C_g), while the source and drain electrodes are parameterized by contact resistances $R_{s,d}$ and capacitances $C_{s,d}$

impurities (e.g. remains of SDS or EBL resist) originating from the fabrication process[1].

Another reason for the high value of measured resistance is that the assumption of ballistic, scattering–free transport cannot be justified for all devices. In a SWNT device, scattering centres can be introduced in several ways, such as: twisting, bending and kinking of nanotubes; nanotube–nanotube interaction within a bundle; structural defects (hepta– and pentagons instead of hexagons) introduced during growth or device fabrication; scattering centres introduced by adsorbates on the SWNT (residues, catalyst particles, individual gas molecules). Some of these factors can be controlled experimentally to some extend, e.g. by refined fabrication and selection. Other factors appear randomly.

In Fig. 3.7 these contributions caused by tunneling barriers and defects are parameterized as contact resistances $R_{s,d}$ and contact capacitances $C_{s,d}$.

Figure 3.8(a) shows the result of a detailed investigation of the electron beam lithography procedure with following development. The micrographs show that even optimized parameters for the resist composition, its thickness, electron beam exposure, and developing time do not guarantee a flawless removal of the resist, which later might separate the SWNT from the evaporated metal contact. In addition, during the developing procedure floating debris of already solved resist might cover the nanotube, again preventing a good electrical contact (see Fig. 3.8(b)). This explains a strong variation of contact resistance.

During this work best values were obtained by using a very thin (3–5 Å) titanium film prior to evaporating 30–40 nm AuPd (60:40) alloy. Superconducting contacts (see Section 4.3) were fabricated by thermal evaporating of 5 nm titanium followed by *in situ* sputtering of 30–40 nm niobium.

[1] Also other factors influencing the contact resistance are under discussion, e.g. precise position of the contact on the SWNT[106].

Figure 3.8: Problems encountered during the fabrication process.

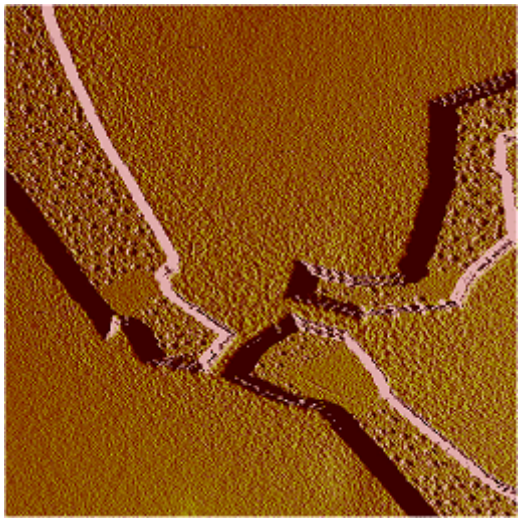

(a) Not completely removed resist layer

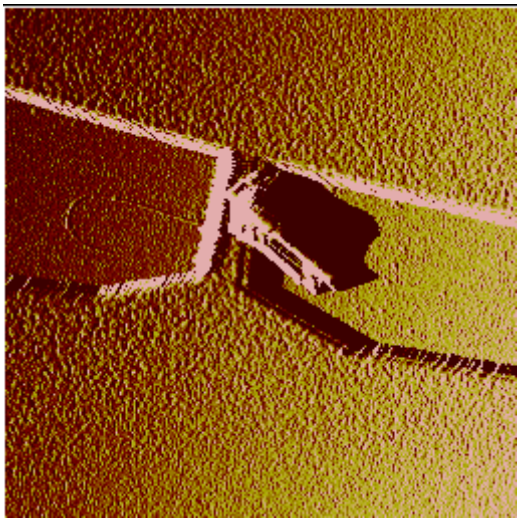

(b) Resist lumps covering the nanotube

Titanium possesses a high degree of wetting both for the chip surface and the carbon nanotube. It therefore provides an additional adhesion of the contacts on the chip surface. It also enhances the electrical contact transparency. During the fabrication of the superconducting contacts the titanium layer had also an additional function of providing a necessary protection for the carbon nanotube during the sputtering process.
Resistances achieved with this fabrication method were of the order of 10–100 kΩ at room temperature. This resistance values can increase significantly at low temperatures, depending on the electrical structure of the nanotube under test and the nature of the contacts.

Electron beam lithography on insulating substrates As already mentioned above, using quartz and $LiNbO_3$ requires different handling during the device fabrication. In particular, the electron beam lithography on these substrates requires additional measures. During the EBL an electron beam accelerated by an electron gun is breaking up chemical links in the organic resist such creating a pattern for e.g. metal contacts. As the silicon chip is highly conducting, it can be grounded easily and the electrons dissipate.

The piezoelectric oxides, however, are insulating. This leads to a strong charge accumulation on the substrate which deflects the incoming electron beam, such making a successful lithography impossible.
To solve this problem, the resist-covered side of the chips was covered by ca 10 nm thick film of chromium directly before the EBL step. This film provides the possibility of electrical grounding, while staying sufficiently transparent. Before proceeding with standard treatment (e.g. developing), the chromium needs to be removed by chromium etch[1].

[1] Similar results can be obtained by evaporating a 5 nm Au film. This procedure has the benefit that no extra etching step is required as the metal is removed during the developing step.

3.2 Experimental Setup

After the fabrication of the SWNT devices measurements have been conducted on several systems. This section gives necessary details on the experimental setup used during this work.

3.2.1 DC-measurements

Most of the DC–measurements were done at the Max Planck Institute for Solid State Research in Stuttgart. Here several systems of the same type were used for device development and characterization. One of these measurements setups was built up during this work (Fig. 3.10).

Figure 3.9: Electronics rack

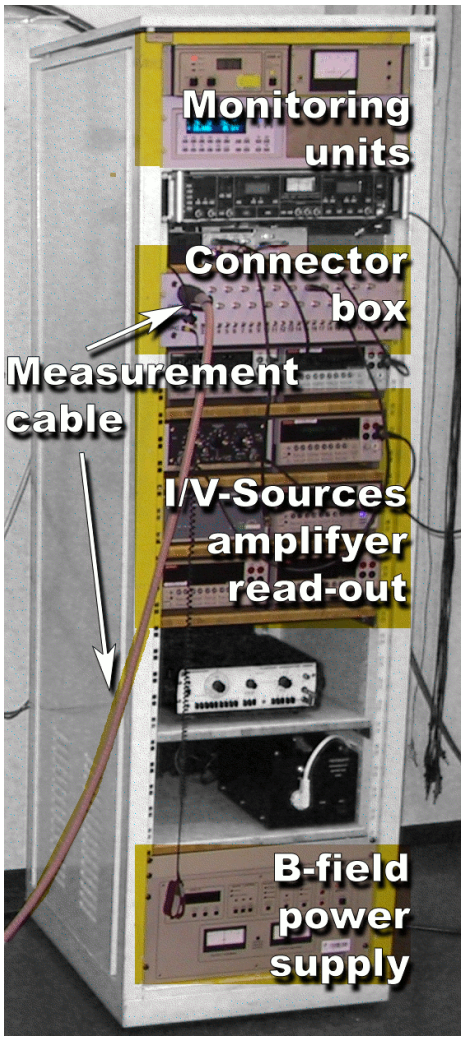

Measurement electronics Figure 3.9 shows main parts of the electronic equipment used for measurements. Applied voltages and currents were generated by source–measurement–units Keithley K2400, voltages were measured by digital multimeters Keithley K2000. Additional current amplifiers were used for measurements of low currents (pico– to nanoamperes). Temperature was monitored by using sensors incorporated into the sample stick. For this purpose sensors fabricated by Lake Shore Cryotronics were chosen for their applicability in a wide temperature and magnetic field range. Cryostates with a built–in superconducting magnetic field coil also require a power supply (Oxford PS-120).
A central part plays the connector box. Here, individual lines leading to the nanotube device (via measurement cable and sample stick)

Figure 3.10: Experimental setup built up and used for the measurements

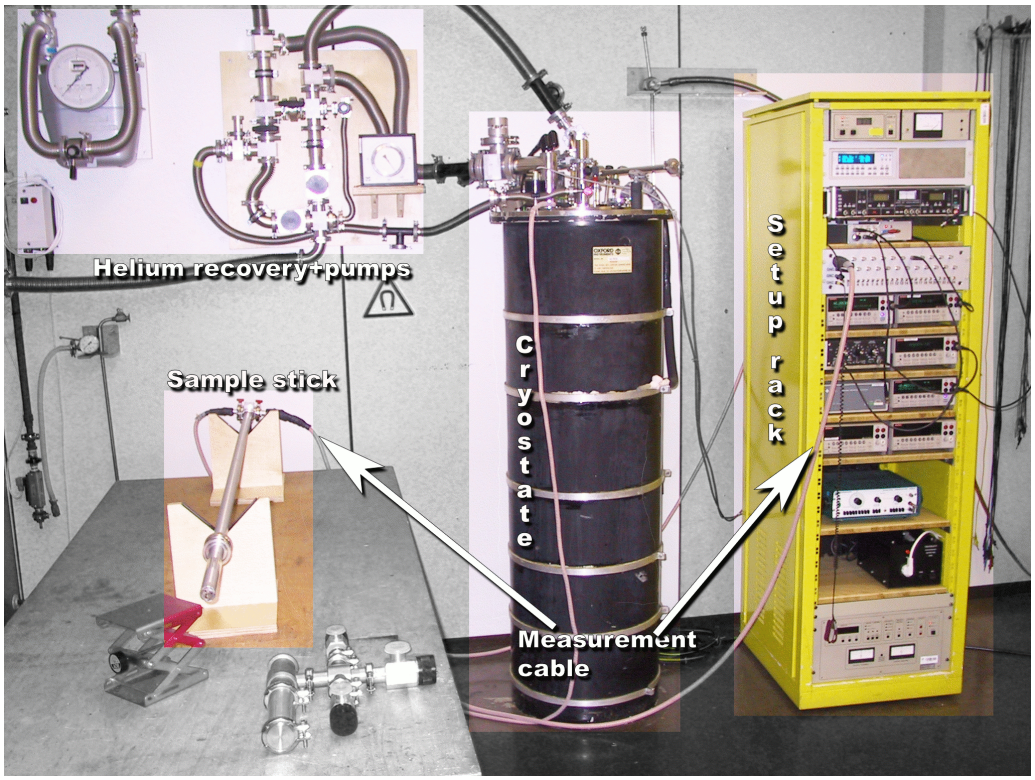

could be connected to measurement instruments. In order to protect delicate devices on the chip from damage of an electrostatic discharge or unintended leakage currents the connector box provided also the possibility of selectively keeping individual connections *grounded* i.e. on the same as the reference potential.
During assembly of the entire setup particular care was taken to minimize electrical noise resulting from the cross-talk in measurement lines or ground loops. Therefore, several measures were taken, such as additional electro–magnetic shielding of individual measurement lines and enforcing of a well-defined reference potential by galvanic decoupling of sensitive parts of the setup using optocouplers and isolating transformers.

^{4}Helium dewars & cryostats Cryogenic conditions were achieved by cooling with the liquid helium (^{4}He) in dewars or ^{4}He bath cryostates. Usually this type of equipment was used for temperature dependent measurements in the range from 4.2 K to room temperature ($\approx$ 300 K). A vacuum pump can also be connected to the associated system of helium recovery pipes. By pumping at the helium

bath inside the cryostat the temperature of the system could be temporarily lowered to approximately 1.8 K. The sample was placed inside the cryostat/dewar by the sample stick. It enclosed the sample, providing mechanical support, electromagnetic shielding and also the possibility of measurements in other than helium environments.

Figure 3.11: Graphical user interface of the software *ViDi*

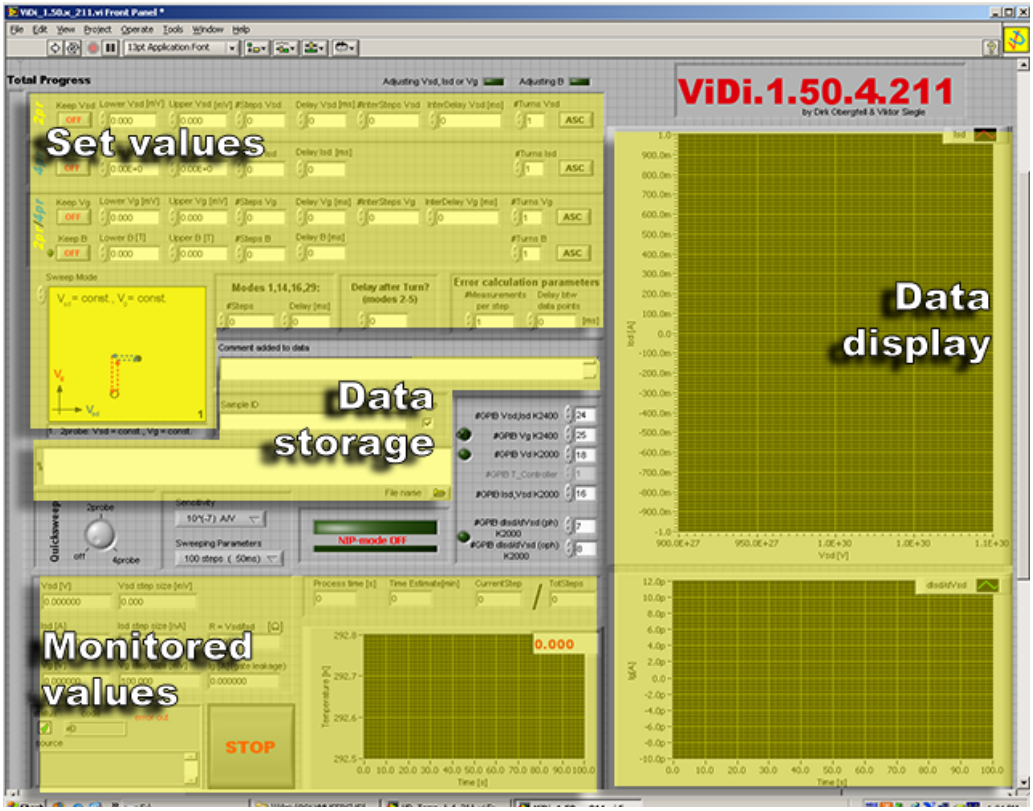

The *ViDi* software The control of the measurement system was performed by the means of *"ViDi*[1]*"*, a data acquisition and measurement control system based on the LabView framework and developed during this work. The software controls each involved instrument, such allowing applying and reading out voltages, currents, temperatures, and magnetic fields. It is also capable of taking electronic records of carried out experiments.

Figure 3.11 shows the screen shot of the graphic user interface. Along with the real time visualization of the measured data it contains the input of settings, monitoring of the experimental process (leakage current, temperature, magnetic field,

[1] formed from the first letters of authors' names: *Vi*ktor Siegle and *Di*rk Obergfell

estimated duration of the experiment), and the dialogue box for the storage of recorded data.
For an easier use of the program it provides several predefined *modes of operation*. These modes correspond to different measurements types typically conducted on SWNT–devices (current–voltage characteristics, dependence on gate voltage, temperature or magnetic field, 2– and 4–terminal measurements). In addition, the modes can be programmed to run over longer periods of time, which allows for automated detailed measurements. Additional features of the program are its ease of operation, usage of commercially available instruments, and adaptivity to new requirements.
Although the program was developed for personal needs it is now routinely used on several measurement setups both in and outside of the the Max Planck Institute. At the moment of writing, adapted versions of *ViDi* are used by several research groups at the Solid State Physics Laboratory of the ETH Zürich, Institute of Nanotechnology at KIT, and Trinity College Dublin.
An exhaustive description of the construction, configuration and operation of the measurement setup can be found in Obergfell[87], along with detailed information on the *ViDi*–software.

3.2.2 AC-measurements

As already discussed in the previous chapter, the operation of an electron pump or turnstile requires the application of an AC signal. A setup designed for high–frequency measurements was provided by the Physikalisch–Technische Bundesanstalt in Braunschweig.
Similar to MPI, the measurement setup at PTB can also be separated in three main parts, namely the cryostat, measurement electronics, and measurement software.

Dilution refrigerator Measurements at PTB were conducted using a cryostat system known as *dilution refrigerator*. The principle of operation is based on the mixture of two helium isotopes: ^{4}He and ^{3}He. In a mixing chamber of the cryostat, the ^{3}He isotope evaporates, cooling the system. Temperatures achieved by these systems are well in the millikelvin range.

The cryostat used at PTB is a Oxford sorption pumped ^{3}He cryostat with a base temperature of circa 30 mK. However, during the RF experiments, unavoidable power losses and a limited cooling power of the mixing chamber lead to heating up of the system. During the measurements the temperature oscillated in close vicinity of 100 mK, which can therefore be reasonably assumed as the base temperature.

Figure 3.12: Modular DAD measurement system developed at PTB

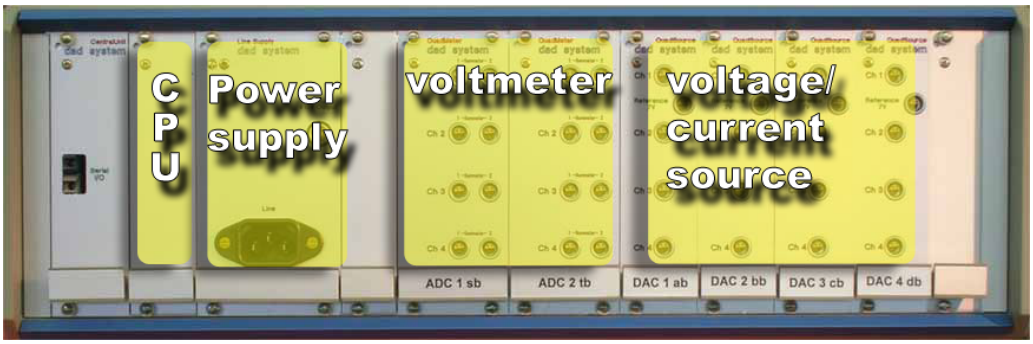

Measurement electronics The electronics used for the measurement was based on a home–made digital–analogue–digital (DAD) system which was designed for low noise and high sensitivity (see Fig. 3.12). The setup is modular and provides up to 16 current/voltage sources and 8 voltmeters. The voltage resolution can be as small as 56 nV for voltage sources and 3 µV for voltmeters.
In order to minimize the electrical noise, the measurement system is operated by a rechargeable battery. For the same reason the communication to PC takes place via optical fibers. Also additional precautions were made in the design of the measurement system (such as wiring of the sample stick and the design of the chip holder) to minimize the cross–talk during the RF measurements.
The RF signal necessary for pumping experiments was provided by the Hewlett–Packard high frequency generator operating in the range of 100 kHz–10 GHz with maximum amplitude of 3 V. Due to impedances of the lines connecting the RF source and the sample, power losses occur. These losses are taken into account by the calibration curve shown in Fig. 3.13.

***ModuLab* software** The measurement system was controlled by *ModuLab*, a powerful LabView–based in–house written software (see Fig. 3.14). It provides

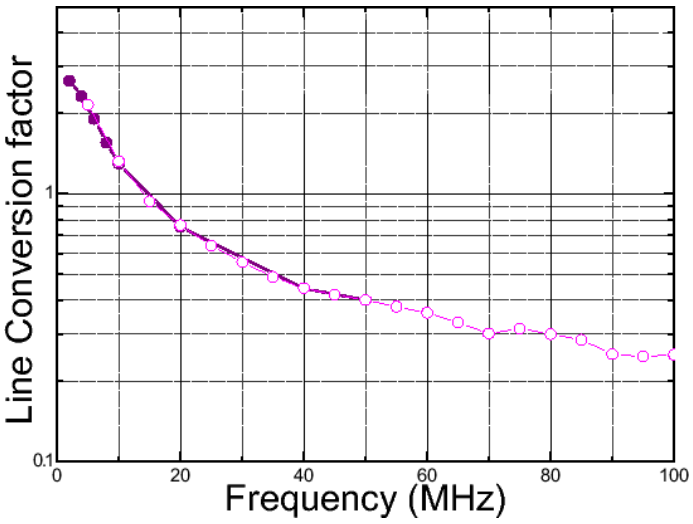

Figure 3.13: Calibration curve for the RF–lines at PTB

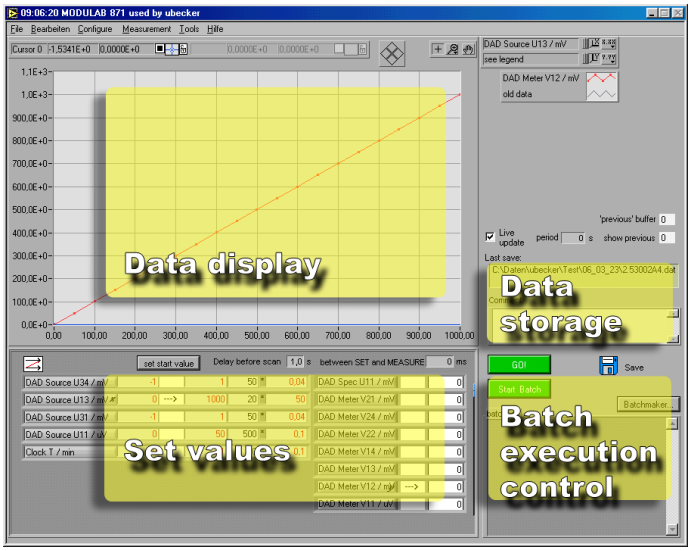

Figure 3.14: Graphical user interface of the software *ModuLab*

similar functionality as *ViDi*, such as control of the devices necessary for the measurements, as well as data visualization and storage. One of the outstanding features of this software is the built–in interpret for an internal batch language. Therefore, any routine sequency involving arbitrary number and type of measurement instruments can be programmed for the experiment. This provides the experimentalist with a flexible, easy to handle and powerful option.

3.2.3 Sample holders used during this work

Different aspects of this work required highly specific conditions. This is reflected in the choice of the used material, of the measurement systems, and also sample holders. As pointed out in section 3.1.3, most of the measurements on SWNT

Figure 3.15: Sample holders used during this work

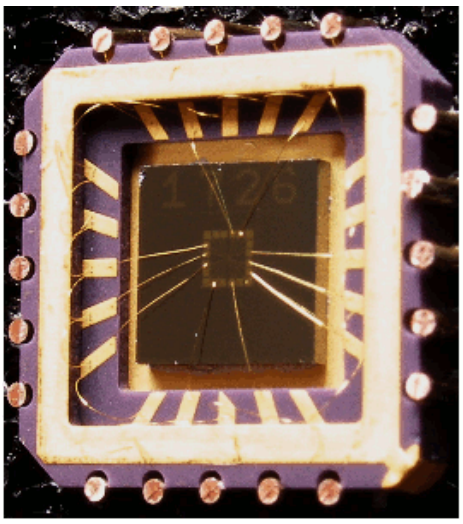

(a) The 20 pin sample holder mounted on the sample stick

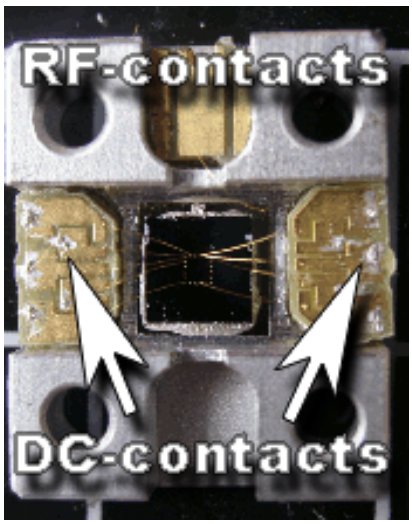

(b) Sample holder optimized for RF measurements

devices are conducted on silicon/silicon dioxide chips. Figure 3.15(a) shows the corresponding sample holder. The chip (dark square in the centre) is glued into the sample holder and bonded to the bond pads on the holder. These pads are connected to notches on the outside perimeter and contacted by spring contacts to the sample stick. This sample holder was mostly used for DC measurements, as well as for the hybrid turnstile measurements (see section 4.3 on page 62).
The sample holder originally designed and optimized for (SAW) RF–measurements is shown in Fig. 3.15(b). All connections to the device are bonded to the *printed circuit boards* (PCB), visible on each side of the sample holder. The PCB on the side, providing 10 contacts in total, are used to contact the devices on the chip. The top PCB is dedicated to the RF–line for SAW generation. All PCB are connected to the sample stick by pogo–pins (as shown in Fig. 3.16(b)). The holes in each corner are used to mount the holder on the sample stick. Unlike the DC–holders, the chips in the RF–chip holders are mounted upside down, so that the pogo–pins press directly on the PCB and the RF–chip holder acts as additional shielding against electrical noise.
The original RF sample holder was designed to carry a $2\,\mathrm{mm}\times 4\,\mathrm{mm}$ piezoelectric chip. The depicted sample holder was modified to accommodate the standard $4\,\mathrm{mm}\times 4\,\mathrm{mm}$ silicon based chip for the local–gate pumping experiments (see section 4.2 on page 55).

Figure 3.16: Modules used for mounting of the sample holders during this work. The design of the module follows the same scheme. On the left is the mounting gear for the respective sample holder (using springs in (a) and pogo pins in (b)). In the middle part a small heating coil is placed. On the right pins are visible which provide mechanical and electrical connection to the sample stick.

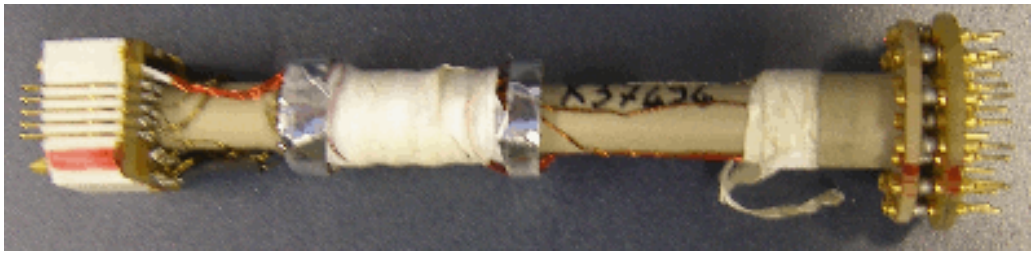

(a) Module for the 20–pin sample holder (as illustrated in Fig. 3.15(a))

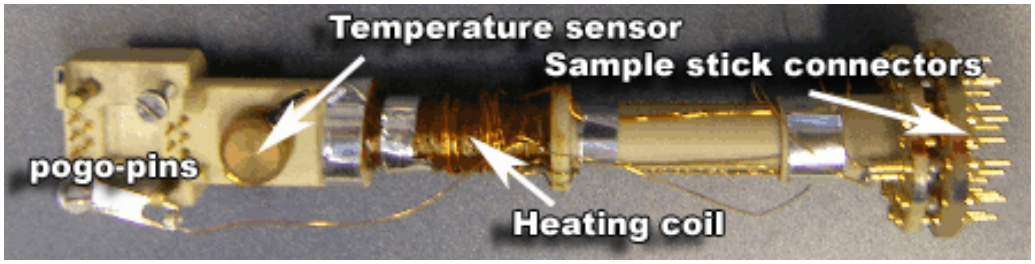

(b) Module for the SAW sample holder (as illustrated in Fig. 3.15(b))

Sample sticks After the bonding procedure sample holders were mounted on sample sticks. As all used measurement setups differ slightly, also different sample sticks are required. Therefore, a modular solution was developed. The sample stick consists of two parts. One part is specific for each individual measurement setup and contains all necessary connectors and cables. The second part comprises a small module containing the chip and sensors. This module is compatible to all systems and can be adjusted for the needs of each specific experiments. Typical applications are the different alignment of the chip within the magnetic field of the cryostat or the integration of the SAW sample holder.
Using this feature the same sample can be easily moved from one setup to another, depending whether a quick test on a simple dewar system is desired or more sophisticated setups, like magnetic field in a liquid helium cryostat or a dilution refrigerator. At the same time the efforts for fabrication of a new sample stick are significantly reduced. The modules used during this work are illustrated in Fig. 3.16.

Chapter 4

Approaches for Pumps and Turnstiles based on SWNT

4.1 SWNT based SAW charge pump

As introduced in Section 2.4.2, the first proposal for using carbon nanotubes as basis for charge pumps was made by Talyanskii et al. in 2001[36]. Therefore, the first part of this work was concerned with implementation of the surface acoustic waves (SAW) driven charge pump based on individual single wall carbon nanotubes (SWNT). Figure 4.1 illustrates the proposed device and its essential parts, which are the substrate, the transducer, the SWNT, and the metal leads. For a successful operation both SAW and SWNT related issues have to be considered.

4.1.1 Choice of the substrate

Taking into account its piezoelectric properties, the lithium niobate ($LiNbO_3$), is on the first look the material of choice to be used as substrate for the SAW experiments. Its value of piezoelectric coupling κ^2 is very high ($\kappa^2_{LiNbO_3} \approx 200$). This allows to achieve high electrostatic SAW potentials at low RF power applied. Lithium niobate also allows generation of SAW with very high (up to 17 GHz[107]) frequencies. This is a great advantage, considering the fact that for metrologically required current sources of about 1 nA frequencies of several GHz are needed.
A good alternative to $LiNbO_3$ is quartz (SiO_2). Even though its piezoelectric properties are not as well pronounced, it is a fairly good candidate. In addition, its surface chemistry is very close to the one of the amorphous silicon (di)oxide which covers the standard silicon chips. This allows similar handling for the surface modification as described in Section 3.1.2 on page 28.
Another advantage is that the ”recipes” developed for electron beam lithography on silicon can be used on quartz, as well. The background is that fabrication of the interdigital transducers is a critical step, with the difficulty lying in the production of several (around 200) long and thin metal fingers (250 nmx80 µm) in

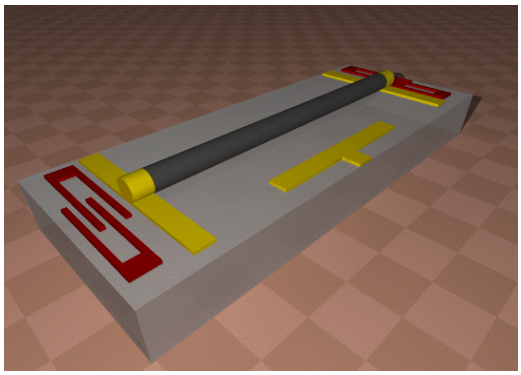

Figure 4.1: Scheme of the SAW/SWNT charge pump. Sketched are parts necessary for the operation: IDT (in red) for SAW generation, SWNT (black) as 1–D channel, contacts and side gate (yellow). The substrate is piezoelectric.

a periodic arrangement. A micrograph of a transducer used during this work is shown in Fig. 4.2. To obtain the required precision in fabrication it is necessary to take into account not only the electrons originating from the electron gun (*primary electrons*) but also the electrons backscattered from the substrate and generated during such scattering (*secondary electrons*). These corrections strongly depend on the substrate and need careful adjustments.

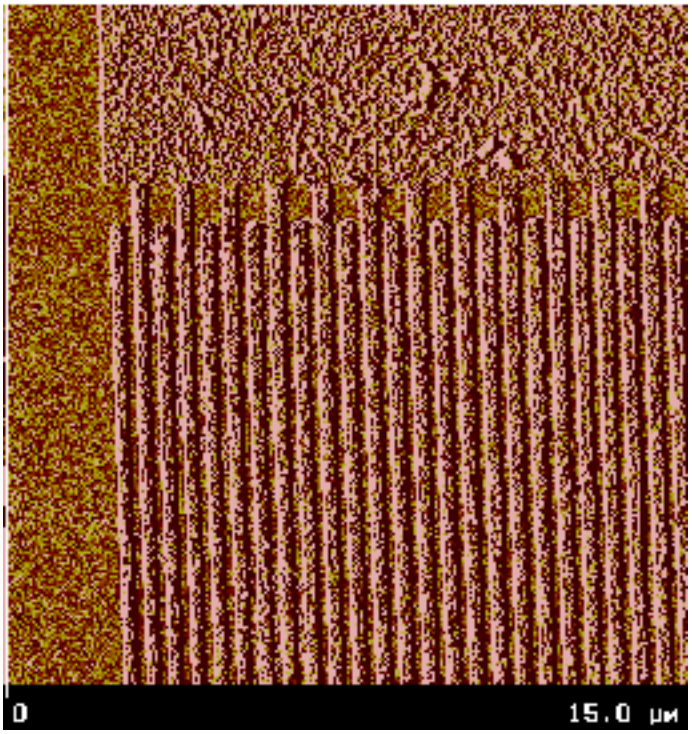

Figure 4.2: An AFM picture of an IDT fabricated on $LiNbO_3$ by PTB Braunschweig. The periodicity of the IDT structure is 1 µm (80 pairs with finger width and finger–finger distance of 250 nm), resulting in 3.4 GHz operation frequency

Another material broadly used for SAW application is gallium arsenide (GaAs), a widespread material in semiconductor applications. However, it was not considered for this experiment due to its low value of piezoelectric coupling.
As discussed in Section 3.1.2, the problem of getting the SWNT on the substrate can be solved by two approaches: either by adsorption out of a suspension, or by growing it directly on the surface by CVD. Both of the approaches were involved during this thesis.

4.1.2 Synthesis of single wall carbon nanotubes by chemical vapour deposition on $LiNbO_3$

Synthesis of carbon nanotubes via chemical vapour deposition (CVD) offers numerous advantages in fabrication of SWNT devices. The nanotubes are grown

directly on the surface, where they will be utilized as main parts of devices. This reduces the fabrication process enormously.
The preparation of a suspension, on the other hand, involves several steps, which have unfavourable consequences. The sonication process is known to introduce defects in SWNT, which effectively results in cutting and breaking the nanotubes down to sub–micrometer length. Especially for the planned SAW experiments this is of a big disadvantage, as the nanotube should be much longer than the SAW wavelength λ_{SAW}. However, to achieve λ_{SAW} <1 µm frequencies above 3 GHz are necessary on most of the piezoelectric materials. This, however, requires a significant effort and is technologically very challenging. Nanotubes grown by CVD, on the other hand, do not undergo any mechanical transformations, which leaves them long (several centimeter have been reported[22]).
Also the fact, that the suspension preparation requires additional chemicals (SDS) is causing problems during the contacting of the SWNT. As SDS wraps around a single SWNT, it might prevent a good electrical contact between the nanotube and the evaporated metal.
In addition, the CVD grown nanotubes tend to have larger diameters (2–5 nm) as compared to nanotubes from laser ablation or arc discharge production (1.2–1.5 nm). Kim et al.[108] showed that SWNT with larger diameter are more likely to have near–ohmic contact. This again speaks in favour of CVD–grown nanotubes to be used for SAW-experiments.

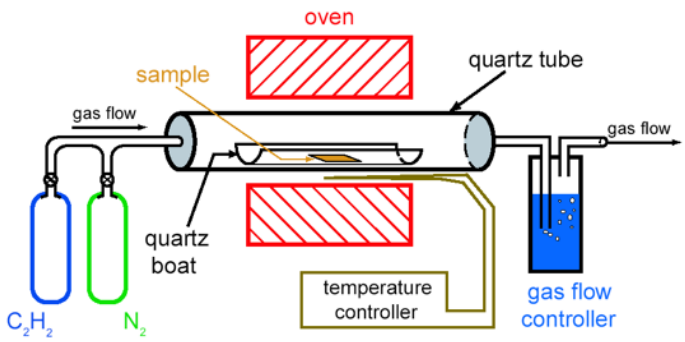

Figure 4.3: Scheme of an chemical vapour deposition setup

A typical CVD setup is sketched in Fig. 4.3. A carbonatious gas (methane, ethane, acetylene) is decomposed at high temperatures of around 1000 °C providing carbon feedstock. Carbon atoms saturate within catalyst particles (typically nickel, iron or alumina compounds) which nucleate carbon nanotubes. By choosing and controlling parameters such as temperature, heating time, gas flow etc, desired results can be achieved. By applying catalyst on specific spots of the chip surface the growth of SWNT can be positioned with sufficient precision.

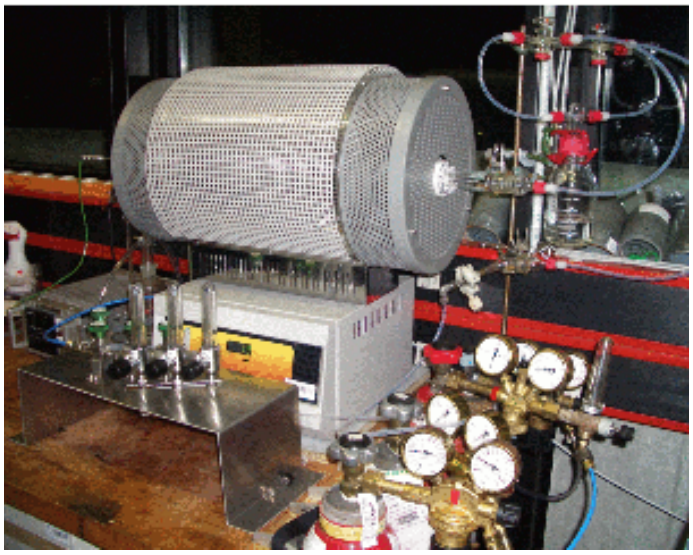

Figure 4.4: A setup built up and used for CVD tests on $LiNbO_3$

At this point of time there was no data available on $LiNbO_3$ in combination with CVD. Therefore, tests were conducted in a CVD setup (see Fig. 4.4) to determine the suitability of lithium niobate for this process.

Figure 4.5: Annealing of $LiNbO_3$ under ambient conditions

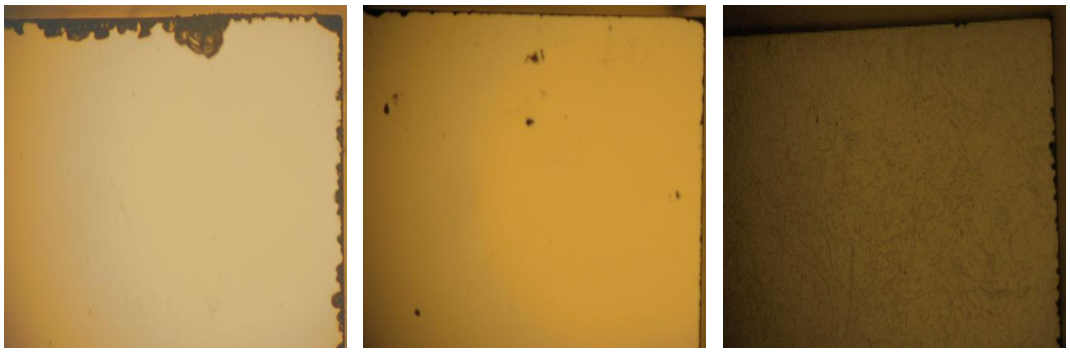

(a) Original substrate (before heating) (b) After heating to 300 °C (c) After heating to 900 °C

Tests showed that the material is strongly incompatible with the process. The surface of $LiNbO_3$ suffers from high temperature and reactive environment. It develops a strong soot–like deposit and the resulting surface roughness the evaporation of transducers impossible. The development of the deposit is documented in Fig. 4.5. This result is also supported by findings of Leek[72] which were reported shortly after the described experiments. According to Smolenskii et al.[109] and Wong[110] $LiNbO_3$ undergoes several phase transitions with increasing temperatures. As a consequence, it cannot be used for SAW applications after the CVD procedure.

Therefore, the devices for this thesis were fabricated by adsorption of SWNT out of a aqueous SDS suspension as described in section 3.1.2. The carbon nanotubes were produced by both the ark discharge and laser ablation method.

4.1.3 Experimental Results

Testing of the IDT performance The simplest SAW device, the so–called delay line is depicted in Fig. 4.6. High frequency AC voltage is applied at the source IDT. If the applied frequency matches the resonance frequency of the IDT, a SAW is generated. In the simplest case it travels to the second (load) IDT, generating a voltage signal across the load R_L.
Additional processes occur in experiments, as indicated in Fig. 4.7, such as multiple reflection of the SAW and high frequency electromagnetic cross talk.
If the surface acoustic wave running across the sample reaches a discontinuity – such as the second IDT, or the sample edge – a part of the wave is reflected. A second reflection of the back wave occurs also on the source transducer. Hence, a part of the wave runs the distance between the IDTs three times. This effect is known as *triple transit echo* (TTE). The resulting interference between the original and the reflected signal leads to increased noise in the measurement.
When a high frequency signal is applied at the source IDT, it can also act as an antenna, emitting the RF signal directly as an electromagnetic wave. This signal is also picked up by the second IDT, contributing to the noise level.
In order to measure the overall transmission of the SAW from the source to the load IDT a network analyzer was used (Agilent E5071B with the range of 300 kHz–8.5 MHz). A network analyzer is a device able to measure frequency dependent transmissions and reflections of electrical signals, in our case occurring at each IDT. The AC–signal was fed into an IDT and transferred via SAW to the second IDT where it was picked up again. A typical measurement is shown in Fig. 4.8.
The measured curve obtained without any filtering (black) shows clear influence of effects described above. The curve is visibly noisy, modulated, and has an offset. Using the fast Fourier transformation, it is possible to transform this signal into the

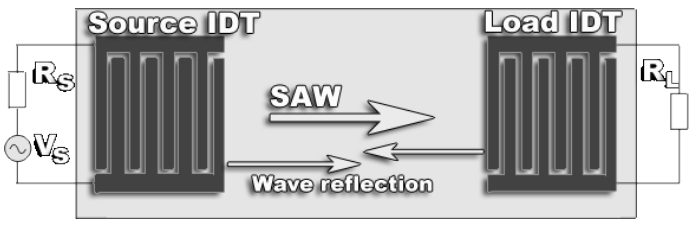

Figure 4.6: An SAW delay line

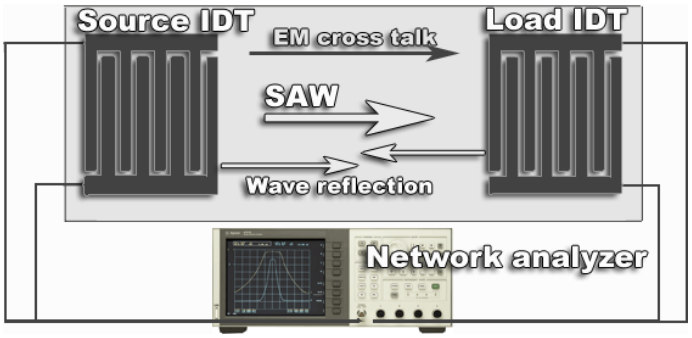

Figure 4.7: Noise sources in a SAW device. Multiple reflections of the SAW on IDTs (TTL) and the AC signal transmitted by the source IDT as electromagnetic wave (EM cross talk) interfere with the desired signal.

time domain. There, the signal can be restricted to a certain time range. This range starts *after* the EM signal emitted by the source IDT reaches the load IDT. The time range ends *before* the multiple reflected wave parts arrive at the load IDT. Using this technique, it is possible to obtain a filtered, noise free measurement (plotted in red). In addition to the expected maximum at 3.35 GHz it also shows a minor peak at 3.42 GHz. The origin of this reproducible peak could not be clarified. A possible reason could be a wave other than a plain Rayleigh surface acoustic wave (e.g. Love wave or a bulk wave, see Campbell[111]) caused by misalignment of the IDT with respect to the crystal axes.

Influence of the suspension on the interdigital transducer As carbon nanotubes are adsorbed from an aqueous suspensions, the IDTs are exposed to (de-ionized) water and SDS. Therefore, the influence of aqueous SDS solution on the IDTs was investigated.
Surprisingly, the experiments showed a severe influence. Several IDTs did not function after the samples have been processed in a way necessary for SWNT deposition. In fact, even the pure SDS solution containing no SWNT decreased or permanently aborted the performance of IDT. The exact reasons could not be fully clarified.

SWNT–SAW device yield During the fabrication process (electron beam lithography and metal evaporation) of SWNT–SAW devices massive difficulties appeared. Structures necessary for SAW generation and SWNT localization (i.e. the IDTs and the marker system) could not be reliably fabricated. This made the production of a sufficient number of devices impossible. Nonetheless, a few samples could be contacted using an AuPd–alloy and provided with side gates, as illustrated in Fig. 4.9(a). The photograph of the chip is shown in Fig. 4.10.
However, no current could be driven through the resulting devices. Failed devices were investigated under the electron microscope. The results are shown

Figure 4.8: Measured response of the SAW delay line, as measured (black) and filtered from the influence of TTE and EM cross talk(red).

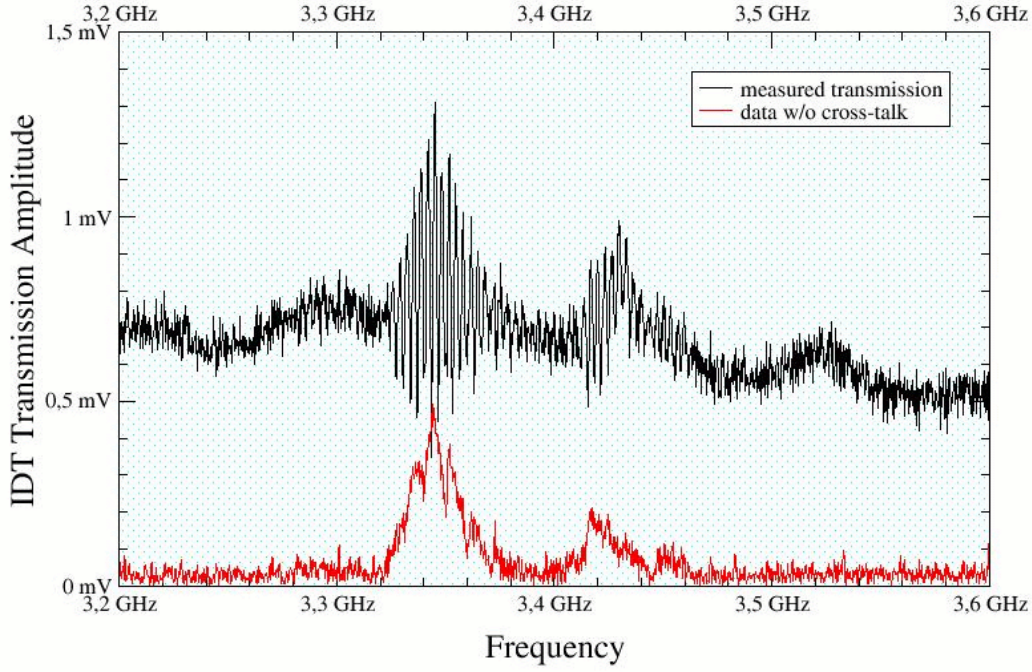

in Fig. 4.9. Obtained micrographs show a strong destructive influence of electrostatic charge on the SWNT–devices (figures 4.9(a) and 4.9(b), taken at PTB) not observed to this extend on nanotube devices adsorbed on silicon/silicon (di)oxide chips. The probable reason is the $LiNbO_3$–substrate. As it strongly insulating, the induced charge cannot dissipate through the bulk therefore destroying the device. Facing the difficulties with a reliable fabrication of SAW relevant device parts and extreme sensitivity of the device to SDS and electrostatic charge, other possibilities for an SWNT based electron charge pump had to be investigated.

4.2 Local gating charge pump

Utilizing the notable properties of carbon nanotubes for the generation of quantized currents without using the SAW technique can be solved by different approaches. One of them, based on local gating of a one–dimensional quantum wire as described in Section 2.5, was also suggested for carbon nanotubes[37]. The carbon nanotube is much thinner than the GaAs based quantum wire used so

Figure 4.9: Impact of static charge on SWNT–devices on $LiNbO_3$

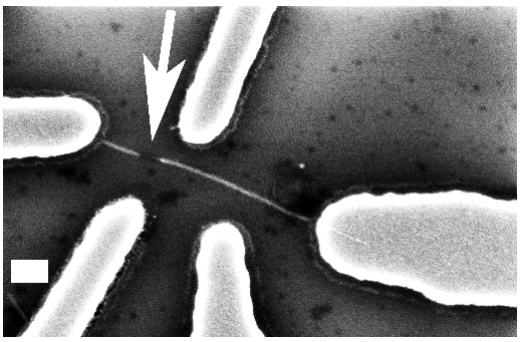

(a) A SEM micrograph of a SWNT device with three side gates. The nanotube suffered an electrical breakdown by static charge. The width of the white box corresponds to 200 nm.

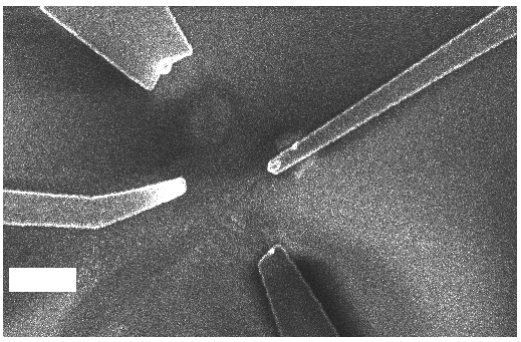

(b) A device completely destructed by electro-statical charge. The scale bar is 1 µm.

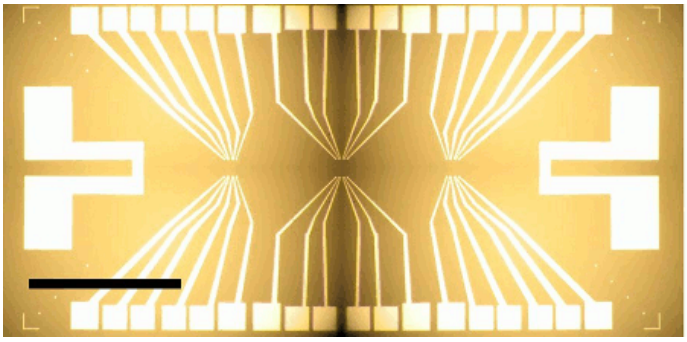

Figure 4.10: Optical image of the 4 mm×2 mm SAW device as used in this work. Clearly visible are the IDT with contact pads (T–like structures on both sides of the sample) and three marker fields with predefined contact leads. The black line corresponds to 1 mm.

far (1–2 nm vs 100 nm). Accordingly, the quantum dots formed by local gating in SWNT have much higher charging energy, a favourable factor for single electron pumping.

Previous works on local gating of carbon nanotubes were reported by e.g. Biercuk et al.[112] and Mason et al. in 2004[113] . The device design, using local gates underneath the SWNT involved several EBL steps and CVD growth of SWNT.

During this work two local gate configurations were tested for the gating of carbon nanotubes deposited out of a suspension: side gates and top gates. In both cases the chip design was similar to the one used for the SAW devices. One difference was, however, that instead of piezoelectric materials standard silicon substrate was used with 200 nm dry–grown SiO_2. Also the IDT from the original SAW design were omitted, as shown in Fig. 4.11.

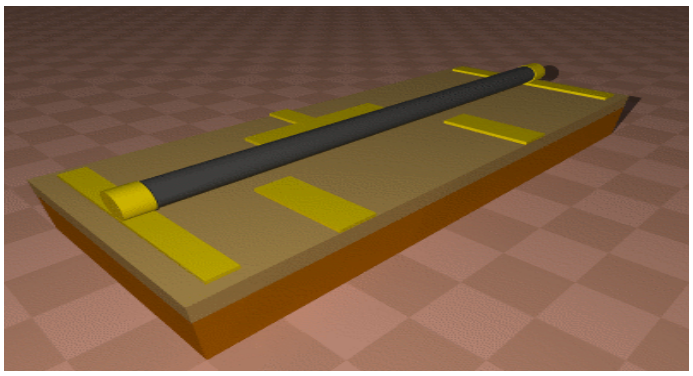

Figure 4.11: Scheme of the local gate SWNT–device (side gates)

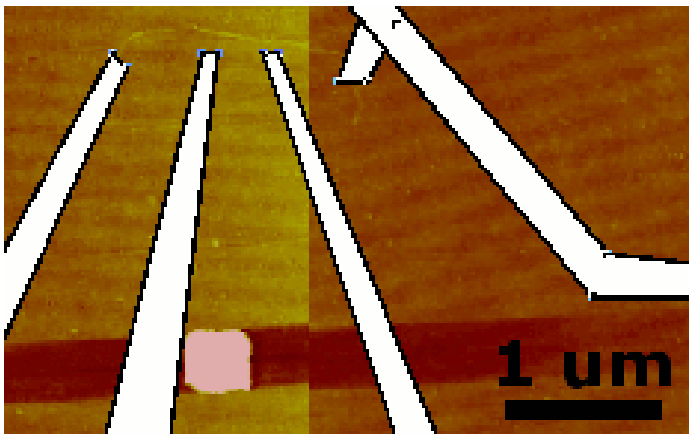

Figure 4.12: An AFM picture of the SWNT (in the upper left corner) on the substrate with indicated contacts and side gate. (Device 01067-M-1-7-56)

4.2.1 Side gate design

The easiest design from the point of view of fabrication is the side gate design. It has the benefit of processing the complete device in one lithography step and avoids the use of additional materials, such as gate dielectrics. Several devices were fabricated following the scheme illustrated in Fig. 4.11.

Carbon nanotubes obtained from the suspension were 800–1200 nm long. Therefore, the width of all structures (contacts, gate leads, and spacings between them) had to be below 150 nm. This is technologically challenging, considering the irregularities of randomly deposited SWNT which prevent the determination of globally valid exposure and uniform sizes of exposed patterns.

Results obtained on one of the devices with two side gates are presented in Figs. 4.13–4.15.

Due to a short these two local gates acted as a single, even though not a uniform, gate. Using this arrangement it was also possible to conduct several measurements on this device which show the main features of side gated SWNT. A comparison of the back gate and side gate operation is given in Fig. 4.13 and Fig. 4.14. In both cases the p–doping of the device by AuPd contacts is clearly

Figure 4.13: Back gate response of an SWNT–device (device 01067-M-1-7-56, T=4.2 K).

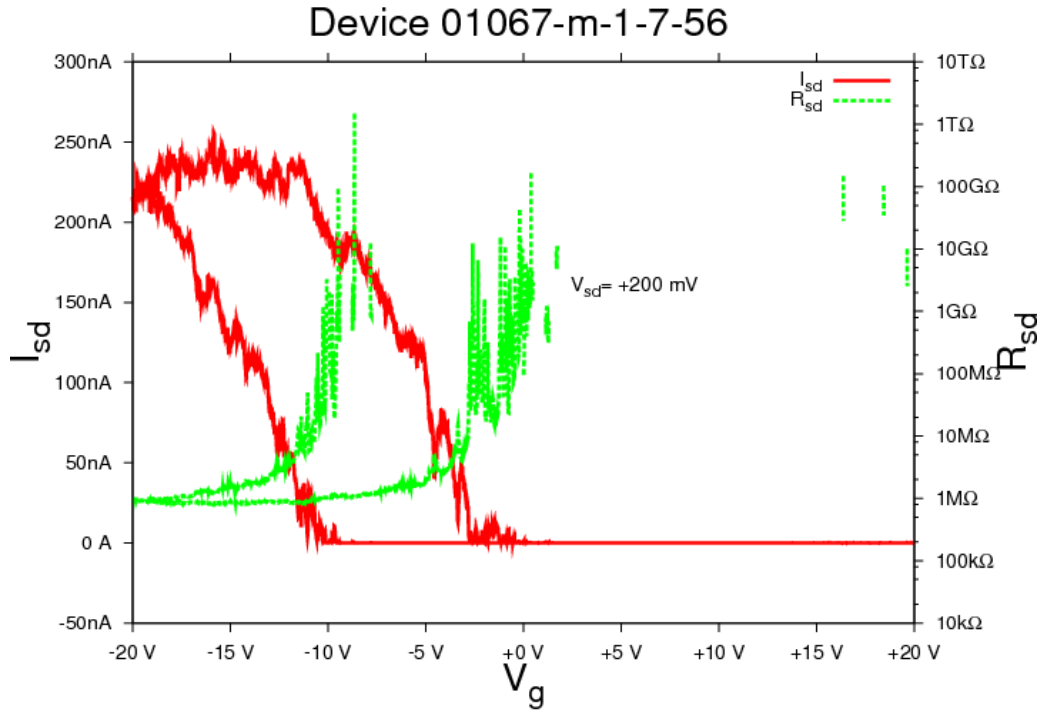

Figure 4.14: Gating by the side gates (device 01067-M-1-7-56, T=4.2 K).

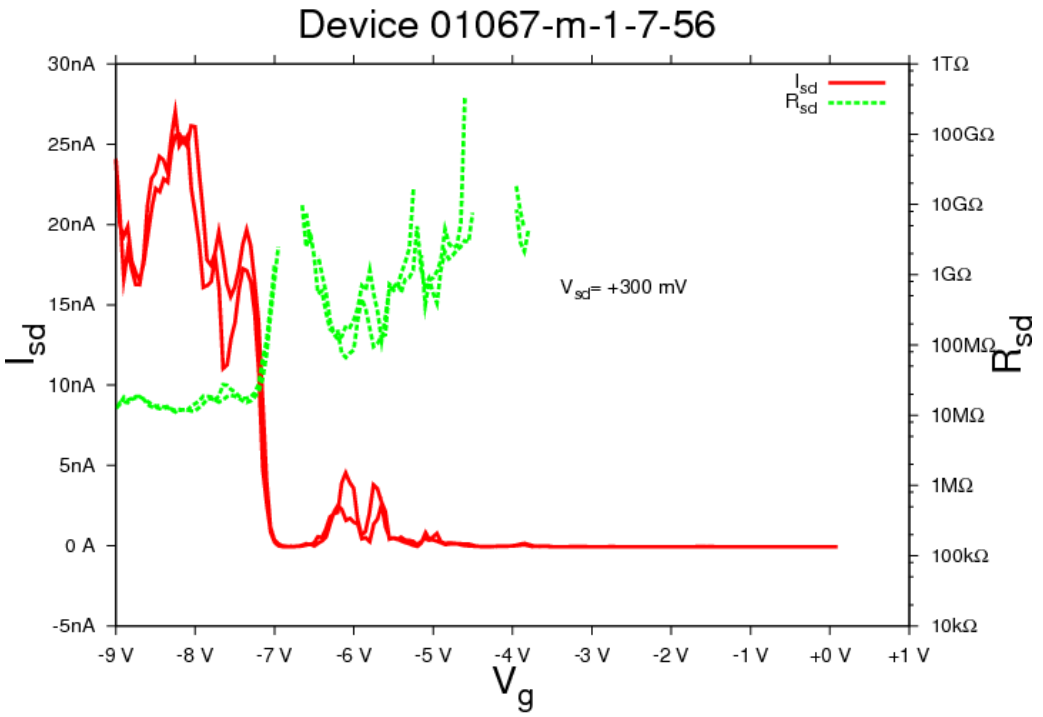

Figure 4.15: A diamond plot measured using side gates (device 01067-M-1-7-56, T=4.2 K).

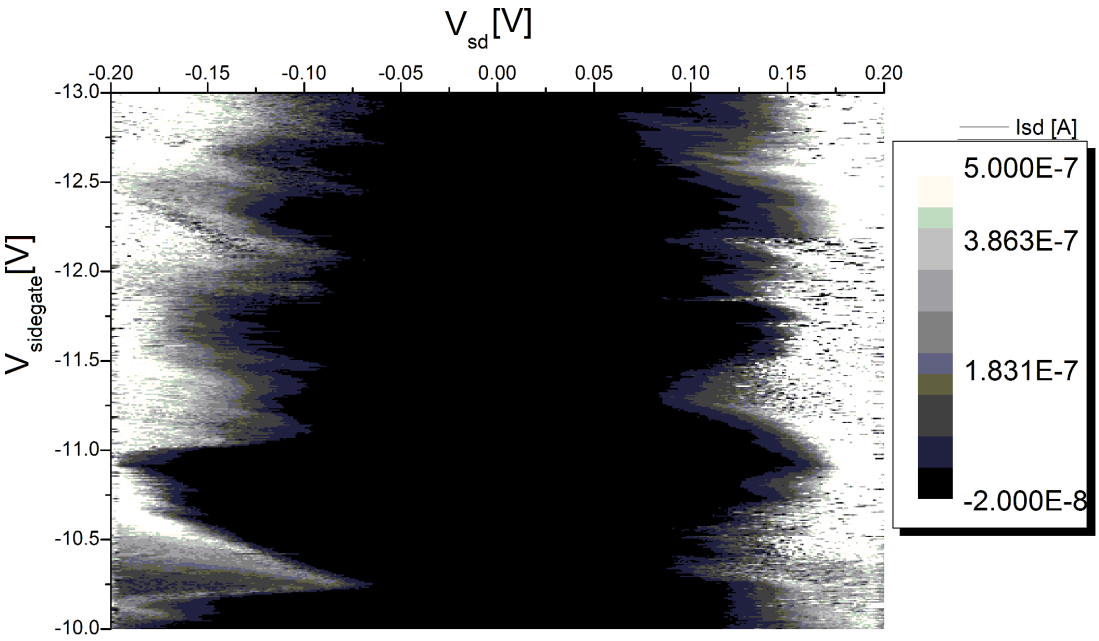

visible. It shows also a hysteretic shift in the current curve for ascending and descending back gate voltage sweeps. This is a feature often present in SWNT measurements on SiO_2. This hysteresis is especially strongly pronounced for large values of applied gate voltage and is caused by impurities in SiO_2. Acting as charge traps (see Appendix B.2), they are activated by the changing back gate voltage and modify the electrostatic potential around the device.

This hysteresis is not present for side gates, as the number of such charge traps influenced by a local gate is much smaller. Side gate have, however, the drawback that very high gate voltages could not be applied. For voltages beyond some threshold leakage currents between the side gate and the drain leads increased abruptly, destroying the device. At the same time, comparably high voltages are necessary for the side gate operation, due to the lack of a dielectric between the gate lead and the SWNT. Results presented in Fig. 4.14 bear a resemblance to the back gate response.

The diamond plot of this device[1] is depicted in Fig. 4.12. Due to high tunneling barriers at the SWNT/metal interface the current was suppressed completely up

[1] For a short introduction into single electron tunneling see Appendix B

to bias values as high as V_{sd}=100 mV. The measured plot deviates strongly from the theoretical shape. That is due to several reasons. Carbon nanotubes are rarely free of defects on the length scale more than 100–200 nm. As the SWNT under test is longer than 1 µm (see Fig. 4.12), it is very likely that it has additional scattering centres, creating serial and/or parallel QD configurations on a single SWNT. In addition, the electrostatic potential created by the forked side gate is not uniform. Thirdly, the electron energy is high due to the bias voltage necessary to overcome the tunnel barriers at the contacts. This energy is sufficient to excite additional states of the SWNT–QD, far beyond the shape expected for a simple SET.

While it was possible to obtain SWNT devices with side gates, the yield of the devices was low. Main critical points, along with high contact resistance, were leakage currents between the side gates and the SWNT, probably due to SDS leftovers on the chip surface.

4.2.2 Top gate design

Figure 4.16: Top gates SWNT device

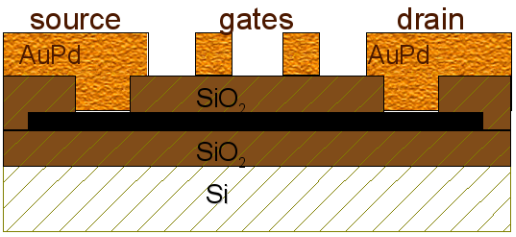

(a) Top gate design involving two EBL steps.

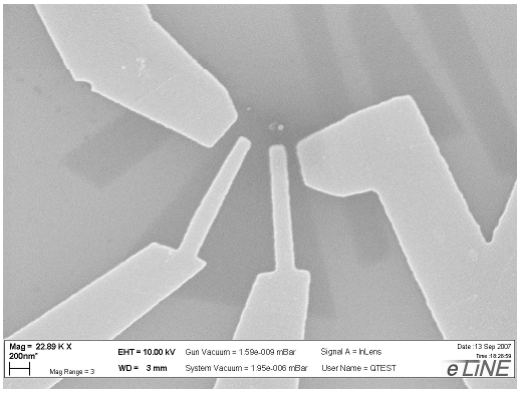

(b) A SEM picture of a top gate SWNT

As alternative, the top gate design was developed. Although connected with additional lithography and evaporation steps, it has several advantages. As the layer between the SWNT and the gate leads is well defined, the occurrence of leakage currents can be controlled much easier. Indeed, evaporated layers of SiO_2 and Al_2O_3 as thick as 15–20 nm were found to be completely sufficient for the purposes of this work. Also, a very efficient gating with low values of gate voltage is possible due to the electrostatic coupling of used dielectrics and to the small dis-

tance between the gate and the SWNT (compared to circa 200 nm in the case of back gate, with SiO_2 as dielectric and circa 100 nm for side gate, with no dielectric involved). In addition, more devices can be contacted per chip when using the top gate design compared to using the side gate design, as contacts and gate leads can be shared much easier among several devices.
The design involving two lithography steps is shown in Fig. 4.16(a). In the first step the areas for later evaporation of the dielectric layer were defined. At the same time, stripes of dielectric material are used to pin down the ends of the SWNT. This prevents the nanotube from shifting around between the fabrication steps. In the second step the contacts and gate leads were defined.
A SEM picture of a top gate SWNT device is shown in Fig. 4.16(b). The dielectric layer is visible as a dark shadow. Recognizable are thin stripes used for fixing the SWNT on the substrate and the larger area used for separating the nanotube from the leads. An example for the performance of top gates at room temperature is given in Fig. 4.17.

Figure 4.17: Local gating of a SWNT by a top gate (ambient conditions)

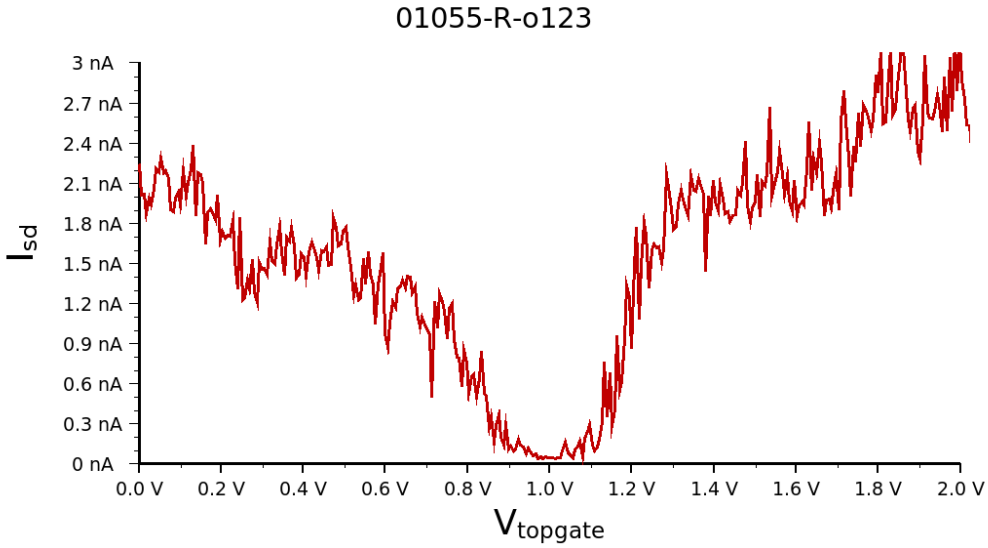

While the back gate (separated by 200 nm SiO_2) had no influence on the device, gating by the top gate (10 nm SiO_2) reveals the nanotube to have a small band gap.
During the measurements on top gated devices it was noticed that many devices had either very high contact resistances or no conductivity at all. Investigating the reasons with scanning electron microscopy revealed that the dielectric material covered the SWNT completely with no gaps for metal contacts left.

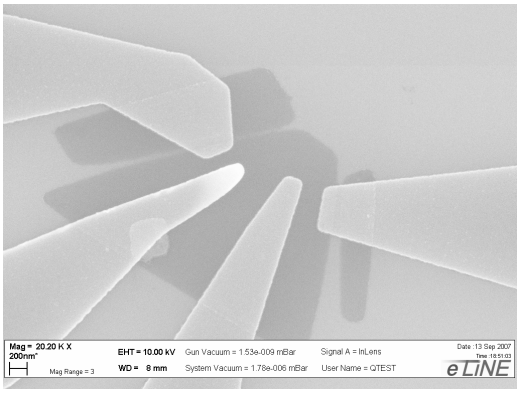

Figure 4.18: A SEM picture of a failed device. The spacing between the areas which are covered by oxide (first fabrication step) is too small to provide a sufficient electrical contact to metal leads (second fabrication step)

The apparent reason lies in the behaviour of the evaporated oxides. Dose tests were run before device fabrication in order to obtain optimal parameters for structures defined by electron beam lithography. While resulting metal structures deviated from the design by not more than 10–30 nm in width, the evaporated oxide structures were up tp 100 nm wider than designed. An explanation is that during the evaporation the oxide particle (which are evaporated at much higher temperatures than metals) are more mobile and fill out not only the space defined by the opening in the resist, but also the much larger area defined by the undercut which results from the 2–layered resist in the EBL..
The idea of using local gating on carbon nanotubes to achieve quantized current pumping is appealing. Also, local gating on nanotubes could be shown in this work using nanotubes adsorbed from a suspension. Both side gate and top gate design were implemented and tested. However, further investigations have shown another alternative which provides desired results with much lower requirements in the fabrication process. Details for this approach are given in the next section.

4.3 Hybrid design based on SWNT

Carbon nanotube quantum dots were investigated for several decades now, also with different types of contacts including superconducting (e.g by Graber et al., Zhong et al.[114, 115]; more on superconductivity in SWNT can be found in [81, 116–120]). Yet there were so far no efforts to employ a SWNT contacted by superconducting leads for the purposes of generating quantized current. This approach, which in the following will be denoted as *hybrid approach* is the subject of the following section.

Figure 4.19: Hybrid turnstile device based on an individual SWNT

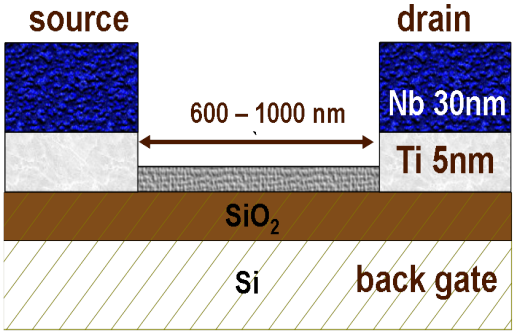

(a) SWNT based SINIS hybrid device scheme

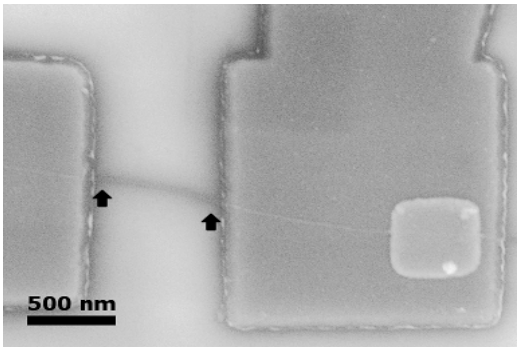

(b) SEM picture of the device 2366-x-x-D2. The length of the carbon nanotube is circa 700 nm

4.3.1 Fabrication and characterization of superconducting contacts

Compared to the previously introduced device designs the hybrid design requires merely a SWNT separated from superconducting leads by tunneling barriers and gated by a global (back) gate.
Carbon nanotubes were adsorbed on the surface and selected as already described above. The contacting procedure was also very similar with two additions. Firstly, the area of the SWNT covered by contact metal could be increased significantly compared to the SAW and local gate approaches. This could be done, as for the hybrid approach the length of the SWNT between the contacts is neither bound to a specific parameter such as e.g. SAW wave length, nor does it have to accommodate several local gates. Also a thin titanium layer of circa 5 nm was evaporated directly on the SWNT for the purpose of higher adhesion and transparency of the contacts. These two measures resulted in contact resistances of several hundreds kiloohm on average.
Although titanium is a superconducting metal as well, its superconducting band gap is small. However, a large superconducting band gap is beneficial for the precision of the underlying pumping principle, as illustrated in Fig. 2.15 on page 22. Therefore, niobium was chosen as superconducting material. It combines high (up to 9 K) critical temperature and easy technological use. Highest quality niobium films are produced by sputtering in ultra high vacuum (10^{-9} mbar and bet-

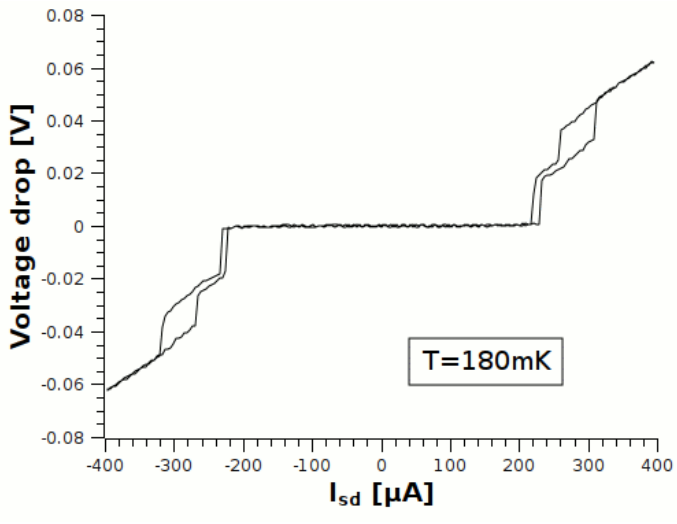

Figure 4.20: Current dependent voltage drop measured at the Nb/Ti metal strip. Both here and in Fig. 4.21 the transition from super to normal conducting state are clearly visible.

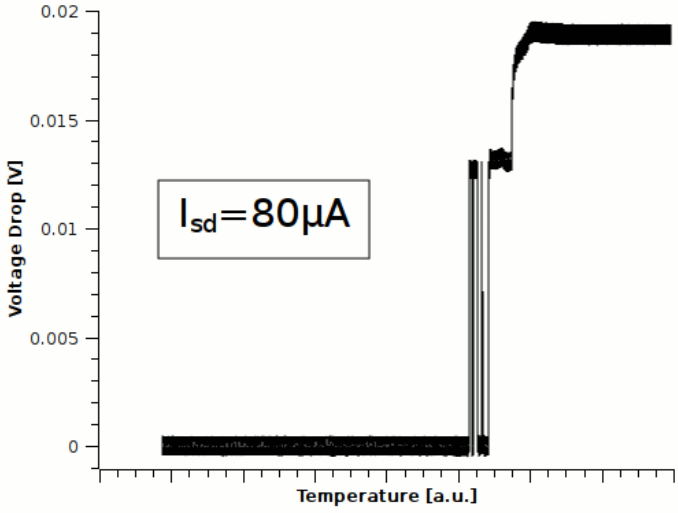

Figure 4.21: Temperature dependent voltage drop measured at the Nb/Ti metal strip. The critical temperature is estimated to be 1.6 K. Similar to the above figure, features of two critical temperatures are observable. These can be attributed to two layers of superconductors (Nb and Ti)

ter), a process where a metal layer on the substrate surface is created by highly energetic atoms.

This procedure, albeit commonly used for conventional Josephson junctions, is not applicable in the case of carbon nanotubes, as their mechanical stability is not sufficient to withstand the bombardment by metal atoms. Resulting defects lead to a low yield and ill-defined superconductor–nanotube interface. Therefore, an additional effect of evaporated Ti was to provide mechanical protection during the sputtering of niobium (30–40 nm).

The critical temperature of the resulting a two–layered contact structure (see Fig. 4.19(a)) was determined in a four–probe measurement. For this purpose a metal strip was defined on the chip containing the SWNT devices. The dimensions of the strip were chosen to correspond to the dimensions of the typical contact lead (several micrometers long, about 250 nm wide, and 35 nm in thick-

ness). The strip was defined and metalized at the same time and under the same conditions as the metal leads used to contact the measured nanotubes. The four–probe measurement was conducted using the same bonding pads on the chip, as used for SWNT measurements to consider all effects involved.
The measurements of the voltage drop across the metal strip as function of applied current (Fig. 4.20) and temperature (Fig. 4.21) showed the the transition from the superconducting to the normal conducting state. It was yet not possible to obtain an exact value of the critical temperature and the resulting superconducting band gap Δ. The reason was that used ^{4}He–systems could only achieve temperatures around 1.8 K, without reaching the superconducting state of the metal strip. By using dilution refrigerators, the superconducting state could be reached and also the transition into the normal state could be observed (Fig. 4.21) by warming up the sample stick from the base temperature of 180 mK to the room temperature. However, the transition occurred at a temperature beyond the sensitivity range of the temperature sensor, limited to circa 1.6 K. Therefore, the transition temperature could not be measured directly in the range between 1.6 K and 1.8 K. Therefore, the value of the critical temperature is estimated with 1.6 K. A similar

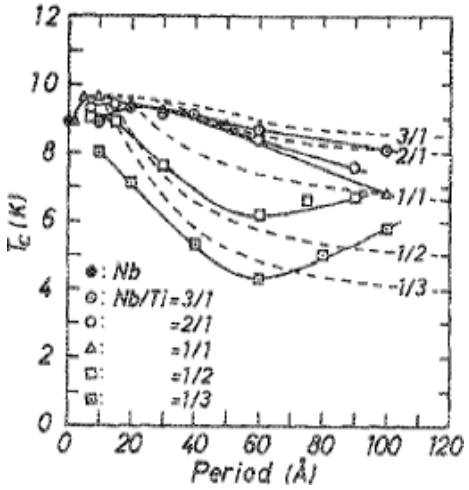

Figure 4.22: Dependence of the critical temperature of Nb/Ti layered structures on relative thickness of layers and their number (Sato[121])

reduction of the critical temperature in Nb/Ti two–layer contacts was also reported by Grove-Rasmussen et al. in 2009[122]. On the other hand, much higher critical temperatures of 7 K were reported by Pallecchi et al. in 2008[117], just by using a thicker Nb–layer. The dependence of the critical temperature of a Nb/Ti–layered structure on the thickness of each layer has been also investigated by Sato in 1990[121] (see Fig. 4.22). This dependence has been explained as the consequence of the superconducting proximity effect between two superconductors with different superconducting band gaps.

4.3.2 Superconducting proximity effect

If a superconductor is brought in contact with a normal conducting metal (or a superconductor with a smaller band gap), the superconducting wave function does not end abruptly at the interface but extends into the neighbouring metal. This *proximity superconductivity* is usually limited to few nanometers. In carbon nanotubes, however, this effect can be observed in structures as long as several hundreds of nanometers due to the very long phase coherence length in the carbon nanotubes[81, 117, 123] (more information on superconducting proximity effect can be found in e.g. [124, 125]).
For the SWNT used in the hybrid device it is necessary to stay a normal conductor even in the presence of the superconducting leads. Otherwise the designed SINIS structure changes to a SISIS structure which is not suitable for generating quantized current. Therefore, the nanotubes for SWNT–hybrid devices were chosen to be as long as possible to avoid the proximity effect.

Figure 4.23: Superconducting proximity effect. A superconducting material (S) is in contact with a normal conducting material (N) or a superconductor with a smaller band gap (S*). The superconducting wave function of S (in red) reaches into the N/S* part (blue).

4.3.3 Observation of current quantization

For the RF measurements the experimental setup at Physikalisch–Technische Bundesanstalt in Braunschweig was employed. There, a dilution refrigerator at a base temperature of circa 100 mK was used with the possibility of applying high frequency signal at the back gate of the silicon chip. The signal has the shape of

$$V_{bg}(x) = V_{offset} + V_{ampl}(\sin \omega t),$$

where V_{offset} is the static gate value and V_{ampl} is the amplitude of the applied RF gate signal.
Current quantization is expected as function of gate amplitude as shown in Fig. 4.24. Several features of the pumping are clearly visible. For example, the number of electrons n transferred per cycle can be modified by simply changing the signal

Figure 4.24: Gate amplitude dependence of quantized currents generated by the SWNT based hybrid turnstile device. (Device 2366-19-20-D2; absolute current values not corrected for AC power losses)

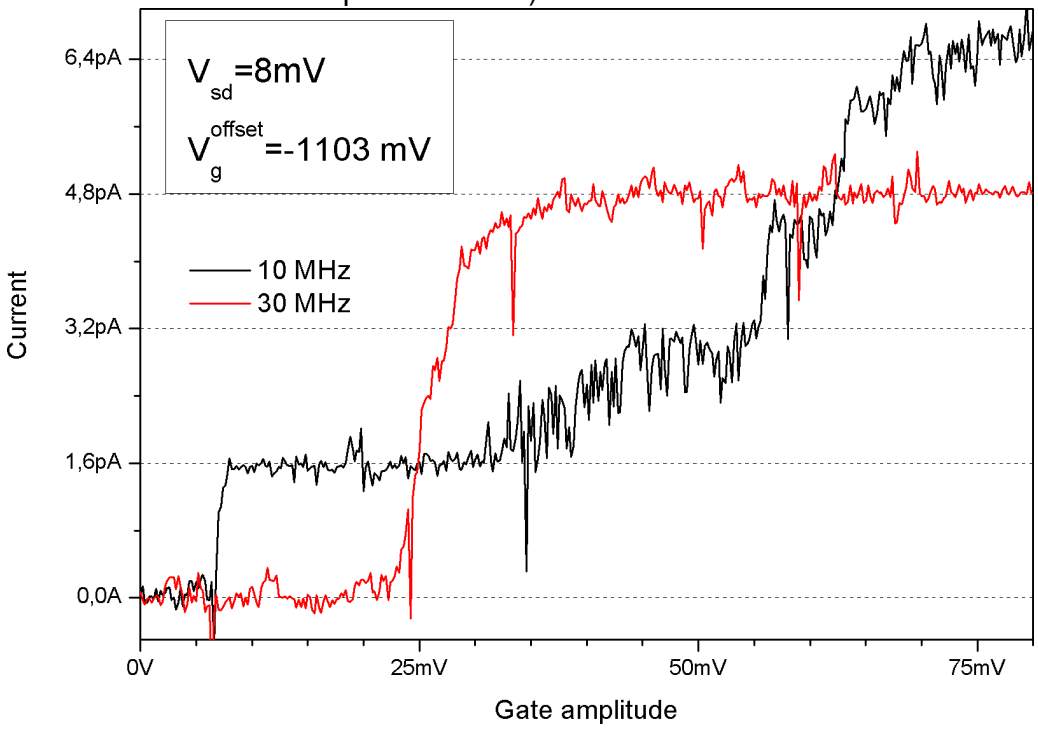

amplitude. This corresponds to several plateaus in Fig. 4.24. Following the relation

$$I = n \cdot e \cdot f$$

the current generated by the turnstile device depends also linearly on applied frequency. The third plateau measured at a frequency of 10 MHz coincides quite well with the first plateau measured at 30 MHz.

Due to power losses in the RF signal lines, a plateau shift toward higher amplitudes is observable with increasing frequencies (compare red (30 MHz) and black (10 MHz) lines in Fig. 4.24 and 4.25). Using the calibration data in Fig. 3.13 it is possible to correct for this experimental artefact, as shown in Fig. 4.26, where the current quantization for different frequencies is illustrated again.

The features mentioned above can be observed also for a wider frequency range (Fig. 4.27 and Fig. 4.28, respectively). In addition, the hybrid device allows the observation of current quantization as function of source–drain bias and back gate offset. Both plots reveal the fact that the SWNT is coupled asymmetrically to the superconducting leads. This is visible in the shift to the negative bias voltages (Fig. 4.29) and in different slopes for increasing and decreasing gate offset in Fig. 4.30. The narrowing down of the plateaus with increasing frequency as func-

Figure 4.25: Gate amplitude dependence of quantized currents in units of e per operation cycle (not corrected for AC power losses)

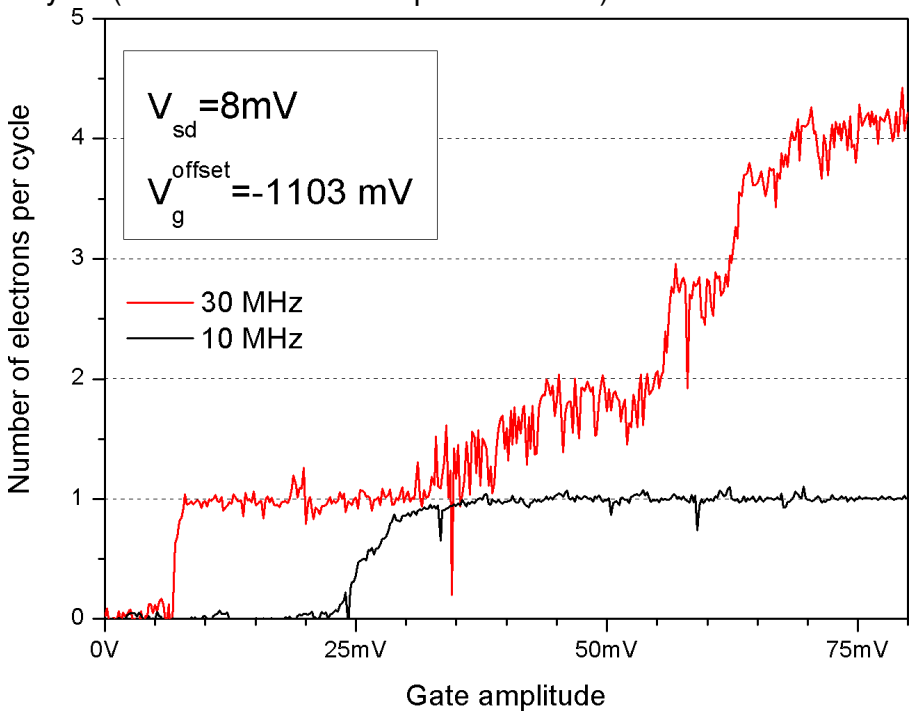

Figure 4.26: Gate amplitude dependence of quantized currents with AC power losses correction.

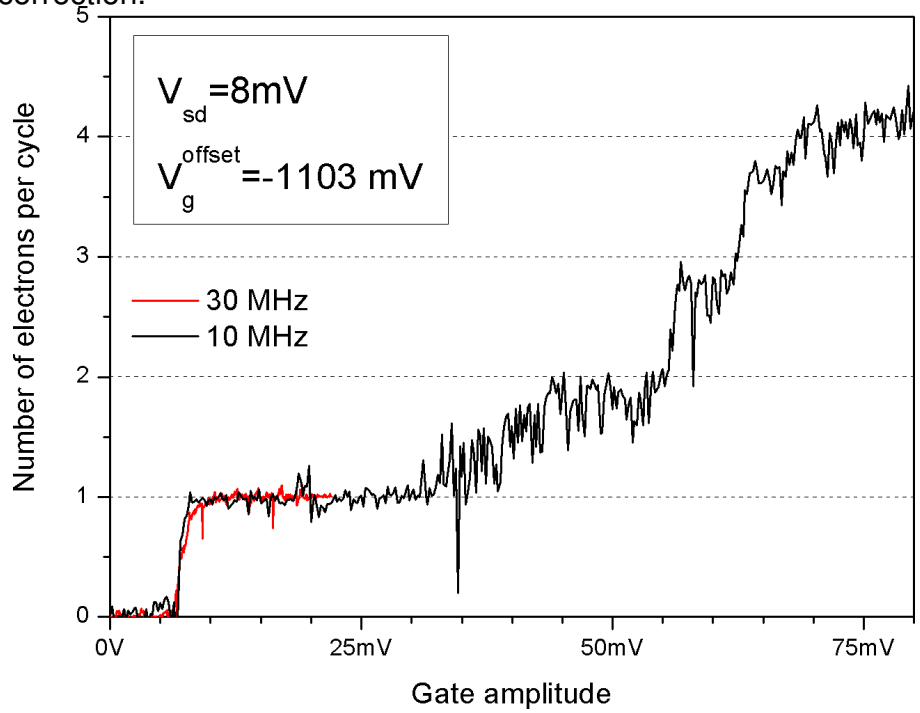

Figure 4.27: Dependence of quantized currents on gate amplitude for several frequencies. (not corrected for AC power losses, here and following: device 2366-19-20-D2)

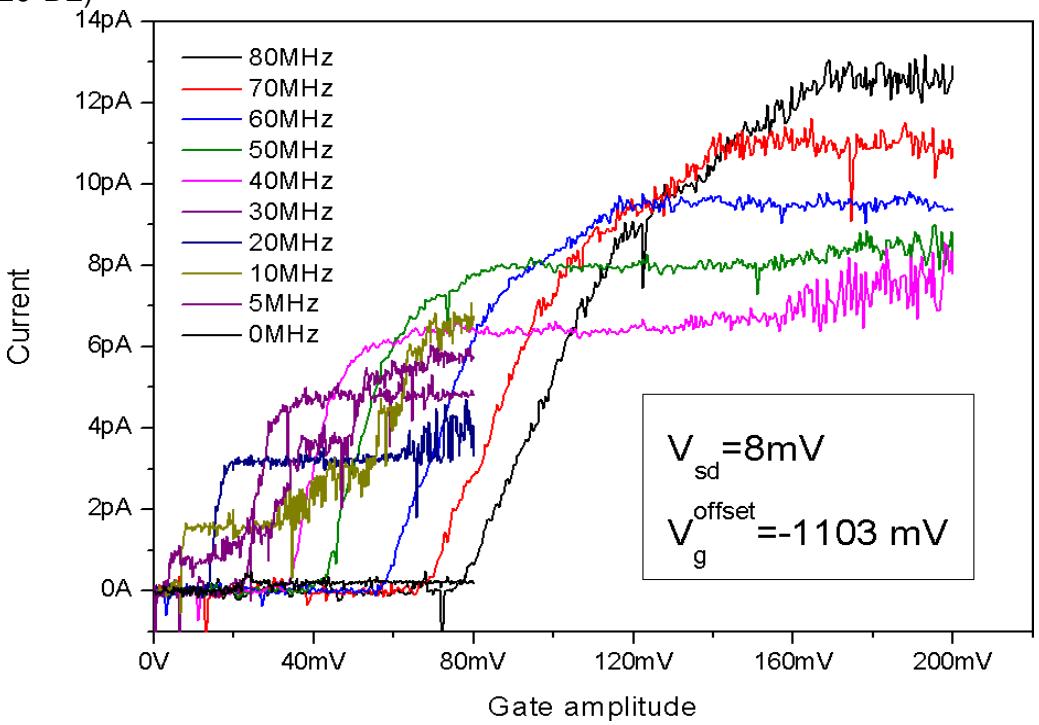

Figure 4.28: Dependence of quantized currents on gate amplitude for several frequencies with AC power loss correction

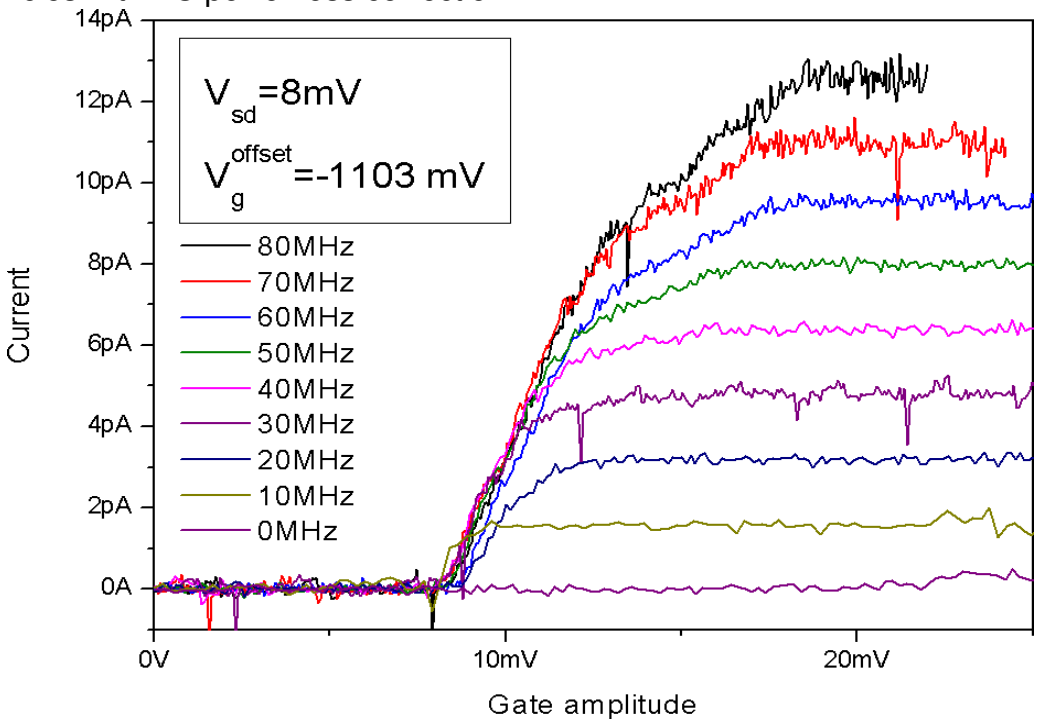

tion of the gate offset is another consequence of power losses in the RF supply lines (increased plateau width at 50 MHz is caused by a different choice of the amplitude value of the AC gate voltage).

In order to compensate for the power losses, the values of gate amplitude at the center of each developed plateau in Fig. 4.27 were noted (see Table 4.1) and used to measure curves in Figs. 4.29 and 4.30.

Table 4.1: Table of frequencies and gate amplitudes used for the pumping.

Frequency (MHz)	Pumping amplitude (mV)
5	7
7.5	10
10	15
12.5	20
15	25
17.5	30
20	30
22.5	40
25	42
27.5	45
30	50
32.5	60
40	90
50	110(150)
60	140
70	180
80	200

The summary plot in Fig. 4.31 shows a clear current quantization in dependence of all three parameters involved, namely source–drain bias, gate offset and gate amplitude.

Plotting the generated quantized current as function of gate amplitude and gate offset (Fig. 4.32) gives a quick access to specific features of a mesoscopic, SWNT–based device.

One of the issues immediately attracting the attention is the structure of the current plateaus. While some of them are clearly and fully developed even when several electrons are transferred per cycle, there are other plateaus with irregularities. Partly, these irregularities in the shape and size of plateaus originate from the decreasing size of the turnstile's central island. The charging process of a small metal island is governed by the Coulomb repulsion of electrons. Shrinking the island down to dimensions comparable with the electron wave length leads however to additional energy quantization according to the quantum mechanical particle-in-a-box-model (compare Fig. B.4 on page 98).

The characterization of the above device (Fig. 4.33) showed a strongly pronounced band gap, which prevents the areas of Coulomb blockade regime from closing. This is expected (see Fig. 2.16 on page 24). Indeed, this expansion of stability regions is the necessary condition for the operation of a hybrid turnstile, as introduced in Fig. 2.16, Section 2.6. However, the size of this gap is larger than

Figure 4.29: Dependence of quantized currents on source–drain bias (not corrected for AC power losses)

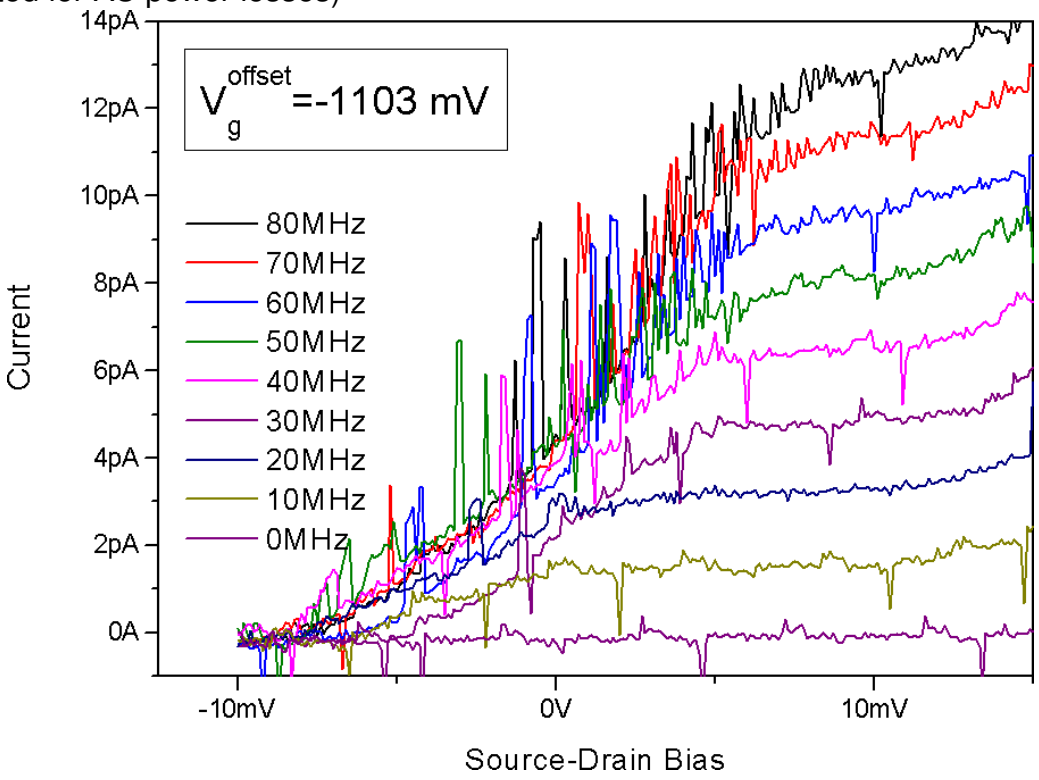

the estimated band gap of contacts used in the experiment and even the gap expected for pure niobium contacts.

Hence, the large band gap is at least not entirely due to the superconductivity. A closer investigation of the carbon nanotube showed it to be a thin bundle consisting of several SWNT. Its gate response (Fig. 4.34) is clearly composed of a (p–doped) semiconducting part, where current increases with negative gate voltage and a metallic part, distinguishable by non–vanishing current at positive gate voltage. It is known, that a defect can split a SWNT in several parts, which then act as individual quantum dots (in both parallel and serial configurations). This can happen due to SWNT kinks, twists, structural defects, or – as very likely in this case – by the interaction within the bundle in question. This explains also the high two–contact resistance of circa 6 MΩ, which deviates noticeably from other resistances achieved under similar circumstances.

This suggests, that in the case of the measured device not one but several (at least two) and different in size quantum dots are present (compare Fig. 4.35). Although the dots couple equally to the back gate, the energy level spacing in

Figure 4.30: Dependence of quantized currents on gate offset (not corrected for AC power losses)

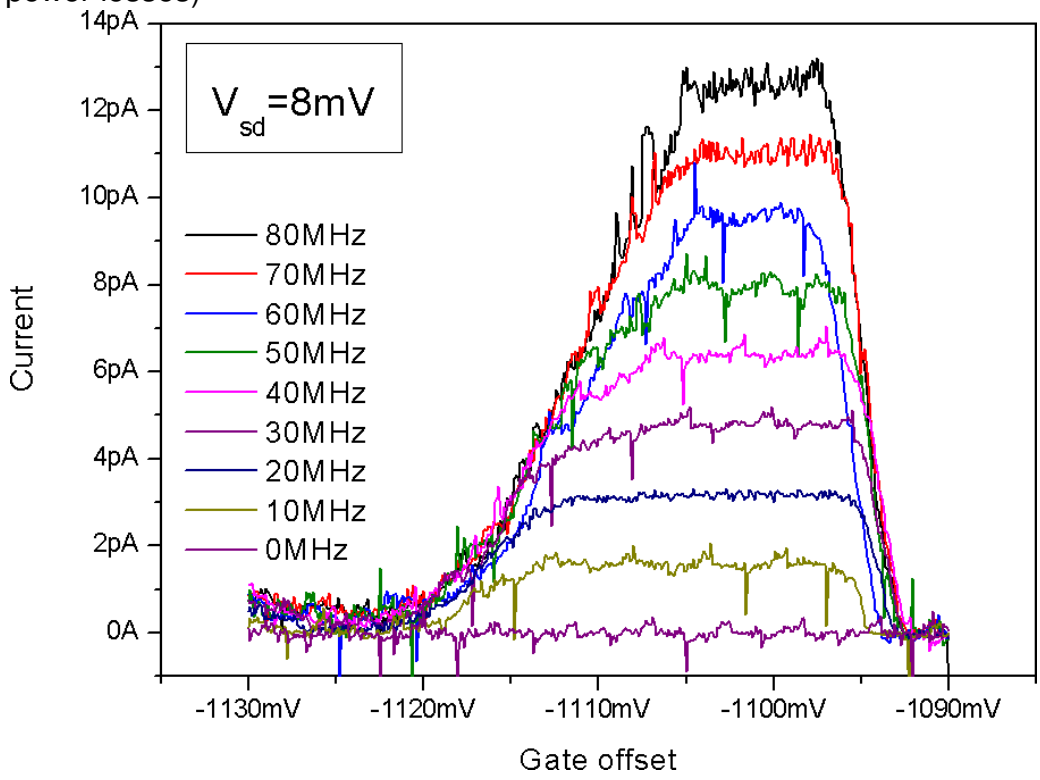

the two different asymmetric dots is not equal. Therefore, the probability for the overall transfer of the electron varies depending on the energy state alignments of both QDs.

The development of the steps in the $I(V_{ampl})$ characteristics (Fig. 4.25) stands out from the results obtained in similar experiments. Typically quantized plateaus monotonically degrade when pumping parameters move away from the optimum settings. We, on the other hand, observe a reappearance of pronounced plateaus with increasing value of V_{ampl}. Also the fact, that the generation of quantized current at V_{offset}=−1136 mV sets in only at considerable pumping amplitude, hints at an additional, dynamic process intrinsic to this specific device. This also speaks in favour of the 'split–SWNT' model.

4.3.4 Influence of superconducting proximity effect

While for an all–metal SINIS turnstile device the total sub-gap leakage is estimated to be very small, the situation in a SWNT based device is somewhat different. Contacted by superconducting metals, the SWNT may become superconducting as well due to the proximity effect. Consequently the quantization steps in the

Figure 4.31: Results summary for source–drain bias, gate offset and amplitude

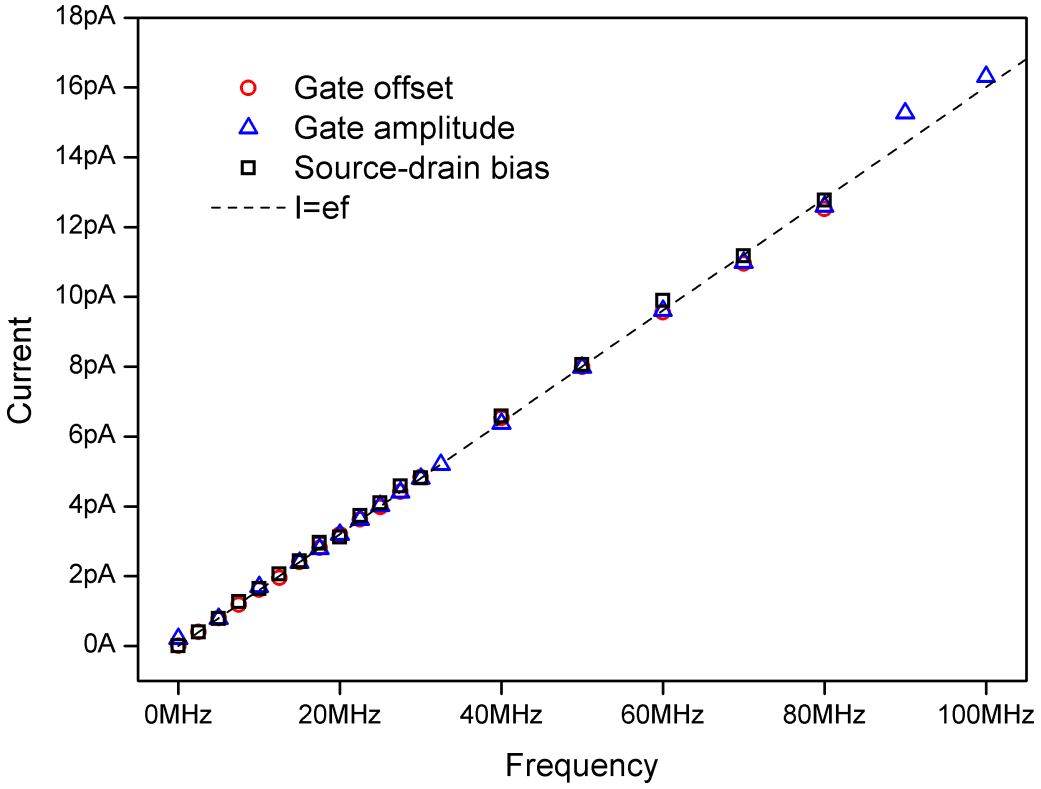

current–voltage characteristics smear out. It is also the behaviour observed in one of our samples (2366-7-8-D1, R_{RT} =80 kΩ, metallic, ca. 700 nm long).
The gate amplitude dependence of the quantized current is shown in Fig. 4.36. The data shows additional features, not shown in the previous plots.
Firstly, the plateaus are developed much poorer and are not equidistant (expected difference between individual plateaus is 1.6 pA at 10 MHz). Also the frequency dependency of the current shown in Fig. 4.37 deviates significantly from the expected straight line. During following experiments these features could be identified as the consequence of the superconducting proximity effect. Indeed, Fig. 4.38 shows for some values of gate voltage a vanishing band gap, as expected in the case of proximity superconductivity. This feature, however, is gate dependent and can be tuned by the gate voltage as also reported by Morpurgo et al.[81].
The peak, reproducibly observed at V_{ampl} =72 mV as well as a dip at V_{ampl} =5 mV could not be explained. However, it is striking that this dip coincides very well with the quantized charge pumping of holes instead of electrons as charge carriers.

Figure 4.32: Three–dimensional plot of generated currents (f =10 MHz, V_{sd} =8 mV)

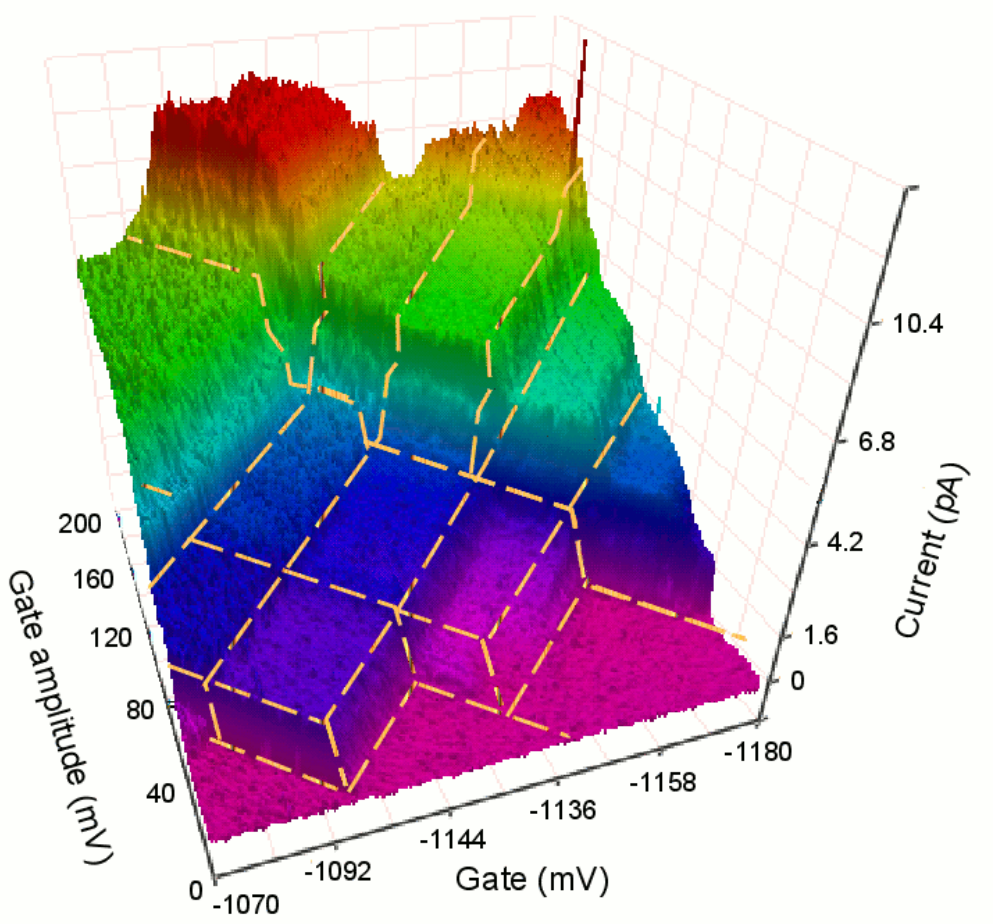

4.3.5 Random Telegraph Noise

Another feature known as random telegraph noise (RTN) reveals itself in the region starting at V_{offset}=−1070 mV and V_{ampl}=80–160 mV in Fig. 4.32. Random telegraph noise is also observed in other mesoscopic systems, such as MOSFETs[1] or small metal stripes (see e.g. Averin and Likharev[47]). Commonly, the origin of this effect is attributed to motion of defects in the sample or to charge traps in the silicon oxide. As seen in Fig. 4.32 and also reported previously by Yu et al.[126] and Jhang et al.[127], RTN is dependent on the back gate and bias voltage. It is peculiar that the random telegraph noise strongly developed between the current plateaus is virtually not present in the plateaus themselves. The apparent

[1] metal oxide semiconductor field-effect transistor

Figure 4.33: Stability diagram for the device 2366-19-20-D2 (T=30 mK). Yellow lines mark the band gap expected for pure Nb contacts, orange lines for the Nb/Ti–contacts used in the experiment.

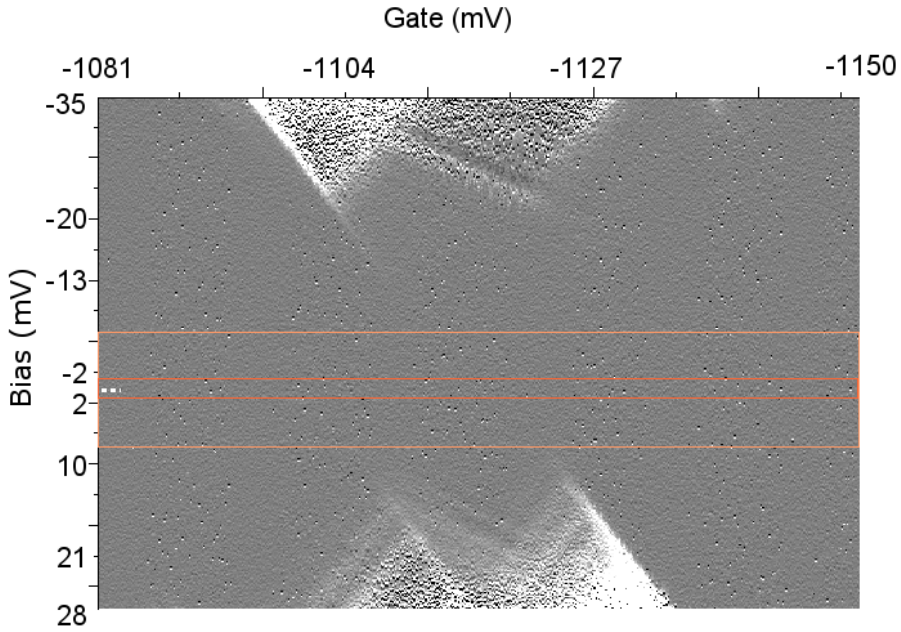

reason for this behaviour is that the locked charge state successfully suppresses the stochastic noise.

4.3.6 Possible error sources

Results presented in Fig. 4.31 deviate from expected values given by

$$I = e \cdot f$$

by a very few percent. While this is sufficient for testing the concept of an molecular turnstile, a SWNT-based definition of a current standard would require a thorough consideration of involved processes. A detailed theoretical analysis of error sources in the operation of a metal hybrid turnstile can be found was done by Averin and Pekola[76] and Pekola et al.[43].
The operation of the hybrid turnstile relies on the suppression of tunneling events in the energy scale corresponding to Δ. For small source–drain voltages the tunneling at the S-N interface is strongly diminished due to fully occupied states below the gap in the superconductor and sets in for energies exceeding Δ.

Figure 4.34: Gate characteristics of the device 2366-19-20-D2. For negative back gate voltages the device clearly displays semiconducting behaviour. Significant currents flow, however, also independent of the gate setting, indicating a metallic component. This I(V) characteristic is typical for thin bundles, containing metallic and semiconducting nanotubes.

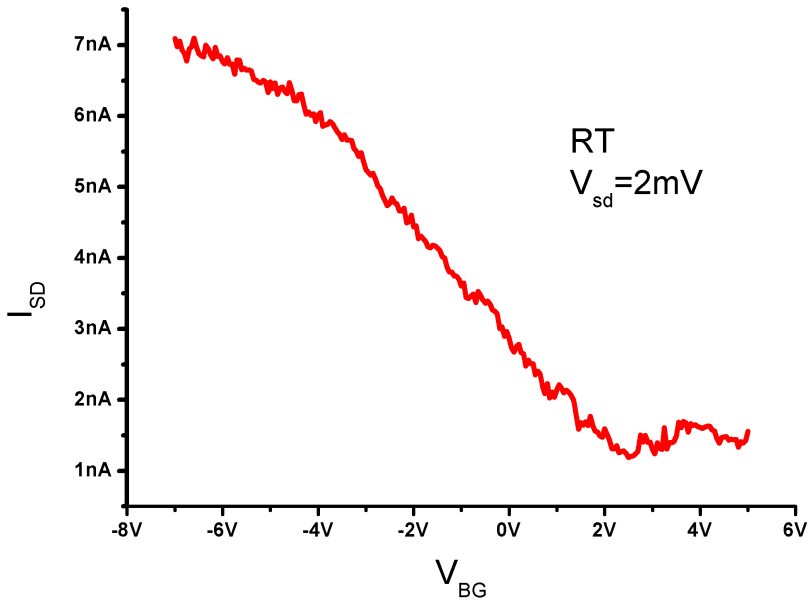

Figure 4.35: Suggested model for the device 2366-19-20-D2

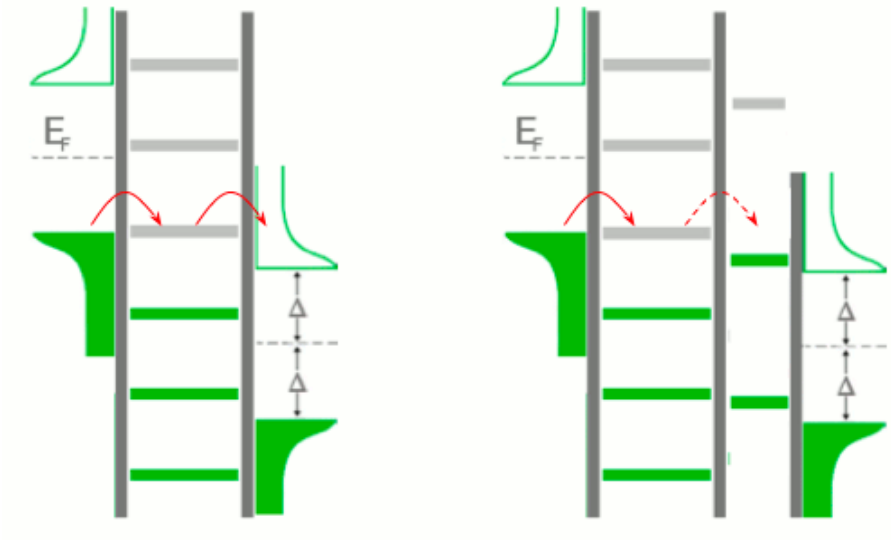

Figure 4.36: Gate amplitude dependence (device 2366-7-8-D1, $f = 10\,\mathrm{MHz}$)

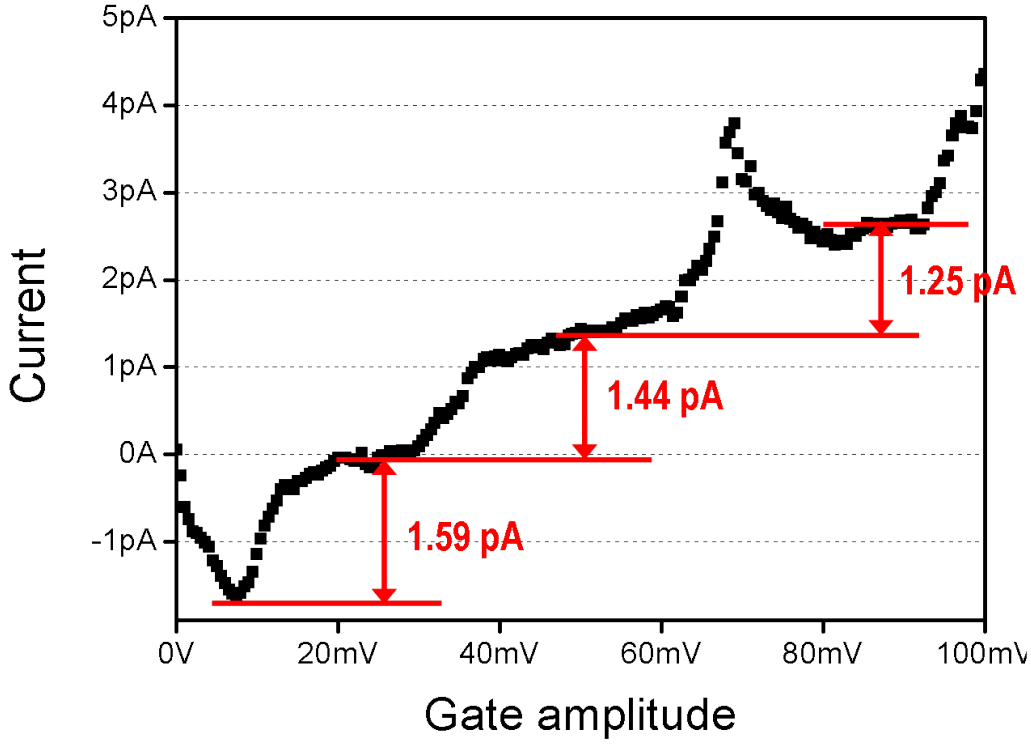

There are, however, several processes enhancing the unwanted forward tunneling for $V_{sd} < \Delta/e$. Apart from pin-holes in the S-I-N interface caused by the fabrication process, there is a contribution to the sub–gap leakage caused by superconducting proximity effect.

An estimate of thermal errors, which at theoretically optimal conditions are proportional to $\exp^{-\Delta/k_B T}$ leads to a vanishingly small value of 10^{-16}. It is worthwhile mentioning that the effective temperature of the turnstile is influenced by joule heating on one hand, and cooling effect arising at the interface between a superconductor and a normal conductor[43, 128] on the other.

A significant error source is a missed cycle. The probability for this process is proportional to $\exp^{-\Delta/2\pi f e^2 R_T}$, which in the case of the presented device can be estimated to 10^{-5} for 10MHz. This value mainly results from the high two-terminal resistance of the presented device. However, contacts to nanotubes with resistances in the order of several hundreds kiloohm have been routinely obtained before and do not pose a serious technological hurdle.

Figure 4.37: Summary for the device 2366-7-8-D1

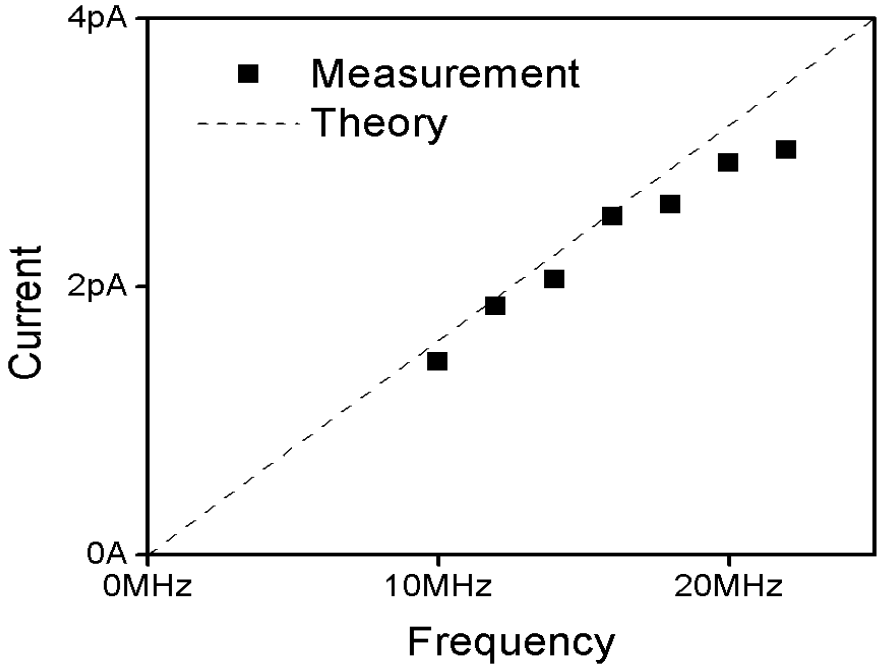

Figure 4.38: Differential conductivity diagram of the device 2366-7-8-D1. The influence of the superconducting proximity effect is visible in the vanishing band gap.

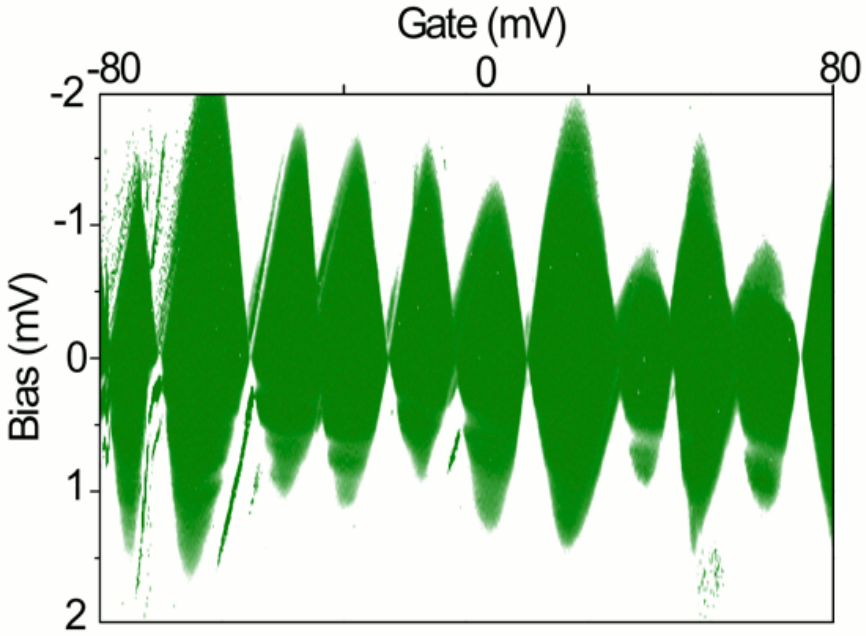

4.3.7 Alternative explanation of the data

Using the SWNT as the base for electronic nano devices involves a vast variety of physical phenomena. This is especially true for the interfaces to metal contacts. Given the variety of known implementations for quantized current pumps and turnstiles and in the light of properties of SWNT observed during this work a direct proof is advisable that the data presented above is described exclusively by the hybrid turnstile mechanism. Such a proof is usually provided by lifting the superconductivity applying a sufficiently high magnetic field. It was also attempted during measurements, however without success, as the critical field of the contact material was higher then the maximum magnetic field provided by the measurement setup (2 T).

Therefore, the possibility that mechanisms other than hybrid turnstile could be – at least partly – responsible for the current quantization was not ruled out. A possible candidate is a pumping principle similar to the one implemented by Geerligs and introduced in Section 2.2 on page 13. Due to the Schottky effect additional states could be created in the vicinity of contacts and separated from the main part of the carbon nanotube by some tunneling barrier as sketched in Fig. 4.39(c). This would effectively split a single SWNT into three quantum dots, such making a Geerligs–like pumping possible. Observations made on SWNT which showed negative differential resistance (Fig. 4.39(a)) due to a strong doping of the SWNT by the contacts in a configuration similar to a Esaki diode make this assumption plausible.

Figure 4.39: Alternative explanation of the data by Geerligs mechanism

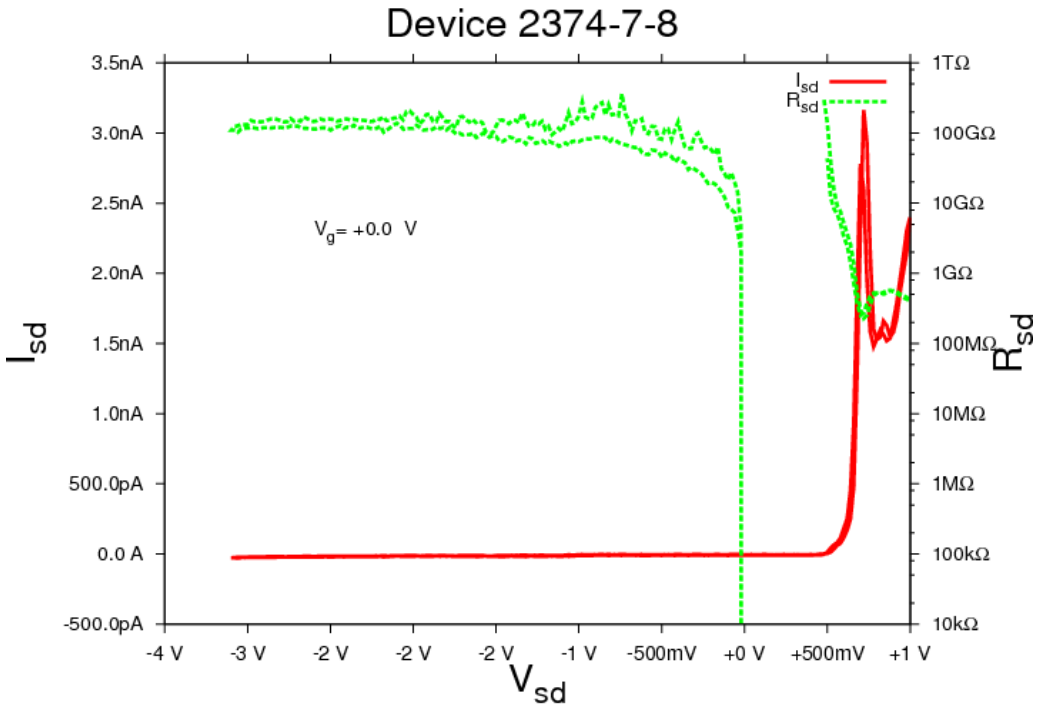

(a) Observed negative differential resistance on a SWNT with Nb/Ti contacts

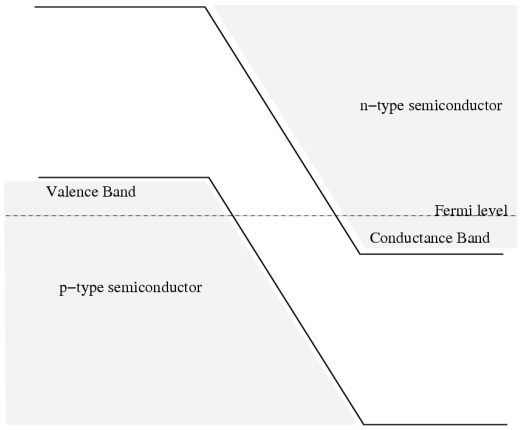

(b) Scheme of the Esaki–diode

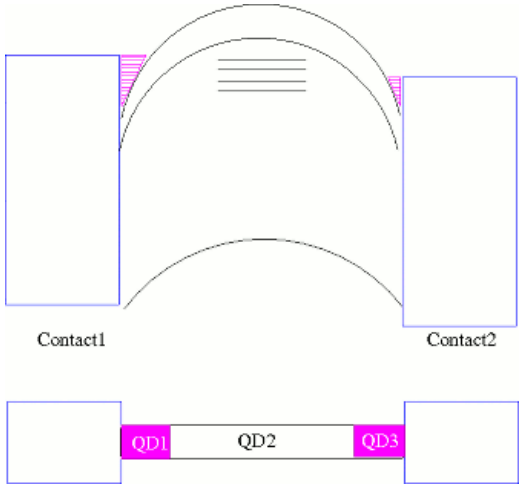

(c) Proposed scheme of several QD on a single SWNT allowing Geerligs–like pumping

Chapter 5

Summary and Outlook

Generating quantized currents with a high precision is a task involving fundamental and diverse physics. One of the approaches aimed at the fabrication of a metrological current source involves loading individual electrons on a very small conductor, usually denoted as *quantum dot*. The performance of such a device increases with decreasing size of the island. Usually, this is accomplished via the top–down approach. There, the fabrication tools are continuously refined to achieve steadily smaller structures.
Carbon nanotubes, on the other hand, offer an alternative, so–called bottom–up approach. Being tubular structures with some micrometers in length and a few nanometers in diameter they do not require additional resizing. Quantum dots based on individual single wall carbon nanotubes (SWNT) have a charging energy – a figure of merit, significant for the operation of single electron quantized current sources – of up to two orders of magnitude higher than available by the top–down approach.
The aim of the presented work is to investigate the suitability of SWNTs as basis for a quantized current source. Three implementation were checked involving surface acoustic waves (SAW), local gating, and properties of normal conducting–superconducting interface.

5.1 The SAW–SWNT approach

The device proposed by Talyanskii et al.[36] involves properties of both SWNT and SAW. The carbon nanotube provides an one–dimensional ballistic conductor. Ideally, it is several SAW wave lengths long and has an appropriate electronic structure. The surface acoustic wave provides a periodically changing electrostatic potential, which is responsible for the electron transport. The resulting device does not require any bias voltage to drive electrons and, therefore, is a real *electron pump*.
In contrast to other SAW charge pumps implemented on two–dimensional electron gas by e.g. Shilton et al.[14], the SWNT based device opens the prospect of the *quantized adiabatic charge pumping*. Similar to the quantum hall effect, it is expected to enable current generation with outstanding precision despite of imperfection of devices involved.
Albeit the SAW driven SWNT charge pump could not be implemented during this thesis, manifold insights could be obtained.

Generating SAW is a complex process, even more so at high frequencies. Several effects come into operation, such as different kinds of induced waves and additional noise sources. Also not only a thorough understanding of the devices is required but also a reliable and reproducible sample fabrication.
Merging SAW and SWNT, two equally demanding areas of research on one device, causes additional issues. Direct synthesis of carbon nanotubes on the piezoelectric substrate via chemical vapour deposition is a promising approach. However, not every substrate is equally suitable for this process, as the investigation of lithium niobate – an otherwise excellent piezoelectric material – showed during this thesis. Adsorbing individual carbon nanotubes on the substrate out of an aqueous SDS suspension entails also several unfavourable consequences. Firstly, treatment of the SAW generating transducers by SDS suspension showed a pronounced and harmful effect. Secondly, leftovers of SDS can prevent a good electrical contact to evaporated contacts. Also, the CVD grown nanotubes have larger diameters and are more likely to have near–ohmic contacts, as opposed to small–diameter nanotubes obtained in laser ablation or arc discharge and used for SDS suspension. The most serious limitation imposed by the usage of the suspension, however, is the maximum length of obtained individual SWNTs. Due to the sonication and centrifugation of the SWNT material only rather short (1 µm) individual nanotubes can be obtained. This, however, corresponds merely to one wave length of the surface acoustic wave at 3 GHz (transducers for higher frequencies and hence shorter wave lengths are extremely difficult to fabricate).
The choice of the substrate for a SWNT device is also of a great importance. Carbon nanotube devices are generally very vulnerable to electrostatic charges, and require extended protection. During this work it became evident that the use of (strongly isolating) piezoelectric materials intensifies the problem. The electrostatic charges on surfaces of the substrates destroy sensitive SWNT devices, which resulted in the observed low yield.
Leek[72] reports also that $LiNbO_3$ is poorly suitable for SWNT–based devices for an additional reason. Being a ferroelectric material, $LiNbO_3$ forms surface domains with large electrostatic potentials, resulting in high electric fields. This, however, is highly undesirable for sensitive measurements.
Based on the obtained experience, the system of choice for further investigations of the SAW/SWNT–device is rather a CVD grown long SWNT on top of a quartz substrate.

Considering the observed obstacles, the demonstration of SAW induced quantized current on SWNT devices by Würstle et al.[39] and Ebbecke et al.[71] is encouraging. It shows that the system SAW/SWNT is in principle capable of providing new perspectives and exciting research (see e.g. [129–131]). On the other hand, the quantized current data obtained so far is not entirely conclusive and does not provide a full picture.
Also concerning the metrological application one has to state that the original proposal by Talyanskii et al.[36] of achieving the quantized adiabatic quantum pumping with the aspired accuracy has not been implemented so far, despite of efforts by Buitelaar et al.[42] and Leek et al.[38]. All pumping data is compatible with the turnstile model with tunneling barriers modulated by the SAW. This device type is however limited in its possibilities of generating quantized current.

5.2 Local gating approach

The local gating approach is taking advantage of the one–dimensional and ballistic nature of carbon nanotubes. It also requires transparent SWNT–metal contacts. The experience obtained during this work shows that a considerable effort is required for a successful and reproducible fabrication of locally gated SWNT devices.
This effort, however, is of purely engineering nature, where existing well–known approaches and tools (multiple steps of EBL, evaporation of different materials, etc) have to be combined in an appropriate order with optimal parameters.
In addition, there is also the aspect uncertainty generated by SWNT. Different existing types of SWNT make a directed development of a device time consuming. Currently, several techniques have been suggested, which target the issue of separating the carbon nanotubes according to their electronic configurations (e.g. [132, 133]). Although technically sophisticated by themselves, these techniques might decrease the effort in fabrication of SWNT–based devices with specific properties significantly.
From the physical point of view and with regard to metrological applications, SWNT is a material worth considering and an exciting object of study. A local gated pump based on an individual carbon nanotube would have significantly improved characteristics compared to currently used implementations.

5.3 Hybrid normal conducting–superconducting approach

The investigations of the suitability of SWNT as base material for sources of quantized current resulted in the implementation of a novel molecular device. Its operation principle is based on Coulomb repulsion and properties of the normal conducting–superconducting interface. Previously these principles were successfully used by Pekola et al.[43] on metal–metal systems to generate quantized current.

The turnstile device comprises an (individual) normal conducting carbon nanotube contacted by superconducting leads. The AC signal is applied at the nearby gate, a small bias voltage is necessary for the operation. The implemented device is able to generate quantized current in a wide frequency range. The robustness of the pumping principle could be satisfactorily tested even in the case of the quantum dot consisting of a single molecule, presence of defects and imperfection of the contacts. In addition, the device has several possibilities to control both the absolute current and number of electrons tranferred in each cycle (continuously tunable frequency, AC gate amplitude, gate offset and bias), not provided by any other SWNT based device at the moment of writing.

It is worth mentioning that the hybrid turnstile device requires least fabrication effort out of all alternatives examined during this work.

The full potential of SWNT-based turnstiles lies in their high charging energies. According to Averin and Pekola[76] higher-order quantum tunneling processes are effectively suppressed with increasing value of E_c/Δ. This allows high currents or alternatively high precision of generated currents. Consequently, currents as high as 100 pA could be pumped with precision of 10^{-8} for $E_c/\Delta = 10$, which is the minimum requirement for a metrological source. However, the choice of materials used in our device already allows for a value of $E_c/\Delta = 50 - 100$ and without the increased lithography efforts needed for high–E_c all–metal turnstiles [79].

The presented work shows the feasibility of implementing a fully controllable turnstile device based on very few molecules – or even a single one. This offers a molecular–based approach to quantum metrology. The SWNT device supersedes the all-metal turnstiles by at least one order of magnitude in the significant parameters and clearly has the potential of meeting the high metrological standards and generating currents in order of several hundred picoamperes.

In addition, the combination of mesoscopic systems with high charging energy, high frequency and S-I-N interface allows investigating new fields of physics, such as e.g. single electron refrigirating as reported by Pekola et al. in 2007[134].
The operation principle of the hybrid turnstile allows also an alternative implementation. While the band gap in the contacts is essential for the successful operation, it does not have to be induced by superconductivity. Merely the size of the band gap is required to have roughly the same order of magnitude as the charging energy of the quantum dot. Graphene, a new allotrope in the focus of the carbon community, has a vanishing band gap, which can be opened if graphene is e.g. cut in thin stripes or nanoribbons. The size of the energy gap can be tuned by the width of the nanoribbon as reported by Han et al. in 2007[135]. This makes an all–graphene turnstile device imaginable. Such a device would have the benefit that all significant parameters – charging energy and band gap – could be engineered and adjusted in one fabrication step, without the limitations imposed by metal systems.
In the light of the current developments in science and technology, when investigated structures keep shrinking, carbon nanotubes offer good possibilities. Due to their size and geometrical factor they provide a relatively easy access to many interesting phenomena which are relevant for mesoscopic systems. This is, despite of many experimental difficulties, a great advantantage of this material.

Appendix A

Surface Acoustic Waves

A.1 General

Applying mechanical force to solids results in a variety of effects. The applied energy propagates by compressional or shear waves. These waves travel either through bulk or on the surface. Complex physical phenomena - such as earth quakes - are a mixture of such wave forms. One of the wave forms is of special importance for the issues discussed in this work. This wave form is commonly known as Rayleigh wave (Fig. A.1).

Figure A.1: Visualization of the Rayleigh wave

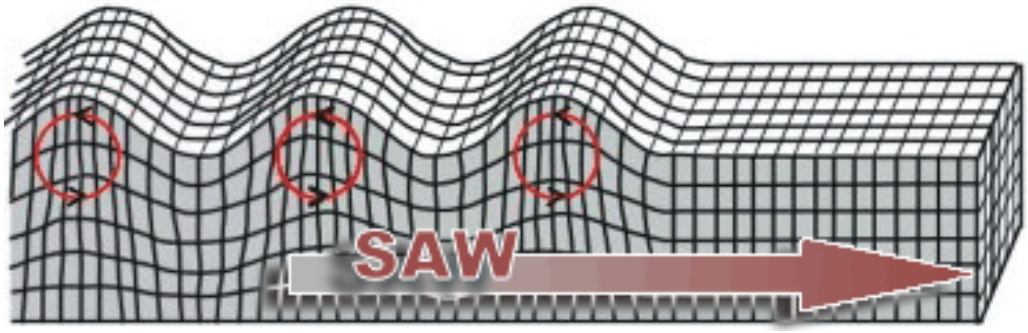

Substrate particles involved in Rayleigh waves perform circular trajectories. Their amplitudes decay very quickly with the depth of the bulk (in the order of magnitude of the wave length). Therefore, the wave can be considered to propagate solely on the surface of the sample.
An important technological application has the generation of Rayleigh waves in piezoelectric materials. There, the acoustic wave is accompanied by an electrostatic wave. The reason is that piezoelectric materials have a permanent electric

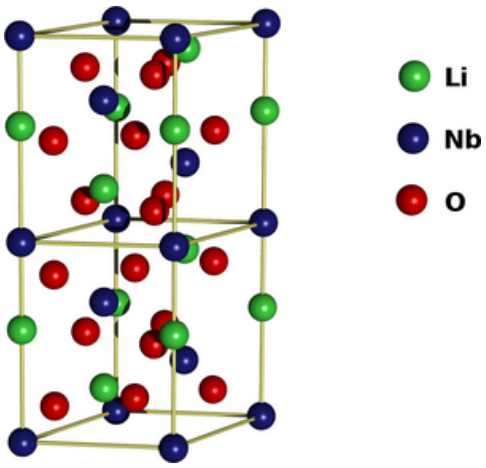

Figure A.2: Crystal structure of $LiNbO_3$. Elastic deformations of the crystal cause a shift of charge distributions. Inversely, applied voltage leads to crystal deformation.

moment due to their crystal structure (see Fig. A.2). As a consequence, any lateral change results in a shift of charges and creates potential difference. Vice versa, applied voltage causes a change in the dimensions of the sample[111, 136]. This quality is well known and is also technically widely used from electric lighters to drive mechanism of an atomic force microscope. Further applications include e.g. various filters in electronics, sensors of different substances[137, 138], storage of light[131], moving micron scale objects and even elementary charges[129, 130, 139–142].

In this work the term *surface acoustic waves* (SAW) always refers to the Rayleigh wave in piezoelectric materials. Both wave components – the acoustic and the electrostatic – move in phase with a wavelength λ.

White and Voltmer[143] suggested in 1965 the use of interdigital transducers (IDT) for SAW generation as illustrated in Fig. A.3. The IDT consists of two metallic interlocking comb–like structures. Its resonance frequency is defined by $f = v_{SAW}/\lambda$. The wave length λ is given by the periodicity of the metal fingers (see Fig. A.3(a)) and v_{SAW} is the velocity of the SAW. The exact velocity and other properties of the SAW for each substrate are defined by the cut through the crystal structure. For this thesis $LiNbO_3$ was used with yz–cut ($v_{SAW}^{LiNbO_3} \approx 3400\,\mathrm{m\,s^{-1}}$) and quartz with 36° rotated y–cut ($v_{SAW}^{quartz} \approx 3000\,\mathrm{m\,s^{-1}}$).

If an AC voltage with the resonance frequency is connected to the IDT, the signal is converted into surface modulation and the SAW is induced propagating parallel to the fingers of the transducer. During this thesis IDT were used with resonant frequencies of ca 3.4 GHz, which corresponds to $\lambda \approx$1 µm.

For SAW induced charge transport the electrical potential of the SAW is essential and hence the piezoelectric coupling of the substrate. The strength of piezoelec-

tric coupling is usually quantified by the electromechanical coupling constant, κ^2. $LiNbO_3$ has a very high value of $\kappa \approx 14$, which is eight times the coupling of quartz and about 16 times the value of GaAs.

Figure A.3: Illustrations of an interdigital transducer (IDT)

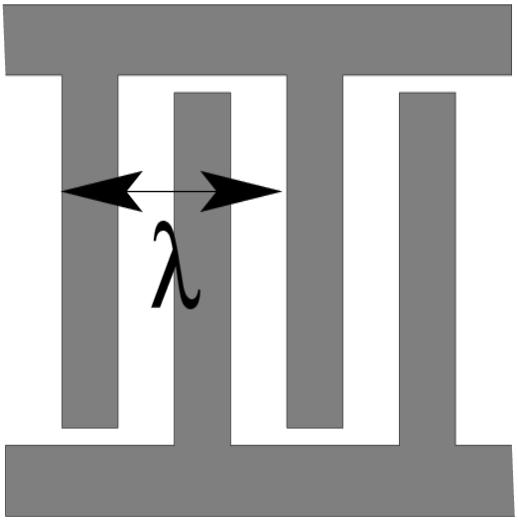

(a) A scheme of an IDT. The operation frequency f is defined by $f = v_{SAW}/\lambda$

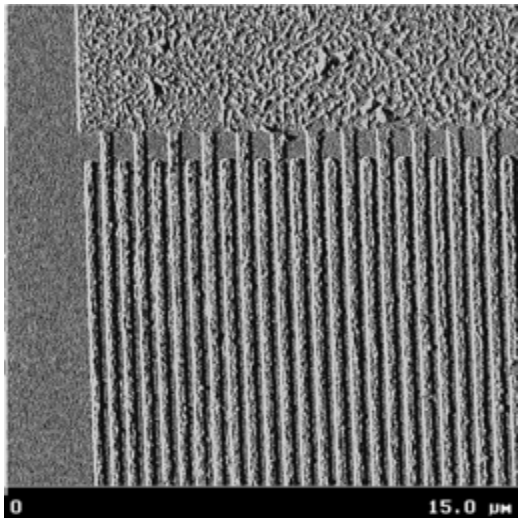

(b) An AFM picture of an IDT fabricated on $LiNbO_3$ by PTB Braunschweig. The periodicity of the IDT structure is 1 µm (80 pairs with finger width and finger–finger distance of 250 nm), resulting in 3.4 GHz operation frequency

A.2 Generation of higher harmonics

The resonance frequency of an IDT is determined by material parameters of the substrate (v_{SAW}) and the periodicity of the finger structure. However, sometimes it is desirable to operate a SAW device at several different frequencies. This is indeed possible if the the IDT is excited not at its fundamental frequency $f_{fundamental}$ but at one of the higher harmonics $f_{harmonic} = n \cdot f_{fundamental}$.
This harmonic mode offers higher operation frequencies with the same lithographic effort for the fabrication of IDT. On the other hand it is also connected to two draw–backs.
Firstly, the amplitude of the SAW is decreasing considerably with increasing harmonics. The operation in the harmonic mode is therefore applicable rather for piezoelectric materials with high value of κ, such as $LiNbO_3$ or $LiTaO_3$.

Secondly, not all harmonics can be generated with the same geometry and therefore different IDT layouts are required (Fig. A.4). The simplest IDT design as illustrated in Fig. A.3(a) is capable of generating harmonics with odd values of $n = 3, 5, 7 \ldots$, as demonstrated by e.g. Ebbecke et al.[71] and also observed during this thesis on some of the $LiNbO_3$ devices. Other values of n can be achieved by choosing devices deviating from this simple scheme as illustrated in Fig. A.4. So is e.g. the three–electrode IDT capable of operating in both even and odd harmonic modes.

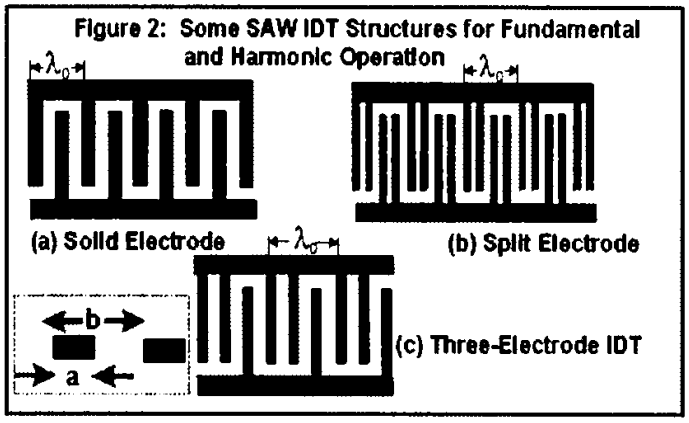

Figure A.4: Various IDT geometries (from Campbell[111]) optimized for different harmonic operations.

Aside from the number and arrangement of the IDT fingers, the amplitude of the individual harmonic mode is dependent on the metallization ratio, which is defined as the ratio between the width of the metallized finger and the finger–finger distance (see the inset of Fig. A.4).

Especially for quantized charge pumps the use of different frequencies is of a great interest. As the amplitude of the SAW is important for the charge transport, it is also particularly important to obtain harmonic modes with high amplitude by optimizing the IDT parameters. Such devices were also designed during this work, but were not implemented due to experimental difficulties on the SWNT side.

Appendix B

Single Electron Transport

B.1 Coulomb Blockade

A device, or – more general – a conductor is considered to be *weakly linked* to the leads if its contact resistances are much larger than the resistance quantum $R_K = h/e^2$. Equivalently one can say that the conductor is separated from the leads by *tunneling junctions*. Under some conditions, it is possible to observe in such a conductor a sharp increase of resistance. This phenomenon is known as Coulomb blockade[46, 47, 144] and is easily understandable considering the discrete nature of the electron charge.

Due to the electric field which is applied across the conductor the electron tunnels from the leads to the conductor (which in the field of of single electron transport is traditionally called an *island*). This, however, is equivalent to charging up a capacitor which is comprised of the island and the the two electrodes. Each new electron to be brought on the island has to overcome the electrostatic repulsion of electrons which are already on the island. Therefore, any additional electron costs the energy of

$$E_c = e^2/2C,$$

where C is the total capacitance of the island. The energy E_c is known as electrostatic *charging energy*.

For macroscopic islands the charging energy is small. However, with shrinking size of the island the charging energy increases significantly and can be as large as several hundreds microelectron volts or even tens of millielectron volts.

Due to Coulomb blockade the energy spectrum of the island is discrete and the spacing between energy levels equals to $2E_c$ (see Fig. B.1). The Coulomb block-

ade can be observed only under the condition that other relevant energies such as thermal energy $E_T = k_B \cdot T$ (with k_B as Boltzmann energy) and the electron kinetic energy $E_k = e \cdot V_{sd}$ are significantly lower than the charging energy E_C. Otherwise, the electron is excited into empty higher energy states, avoiding the Coulomb electron–electron repulsion.

Leaving aside the quantum mechanical nature of electron tunneling from and to the island, the phenomenon of Coulomb blockade is of purely classical nature even though it is brought in connection with and observed in nano–scale devices (Coulomb blockade was first observed by Fulton and Dolan in 1987[145] in a multi–junction configuration).

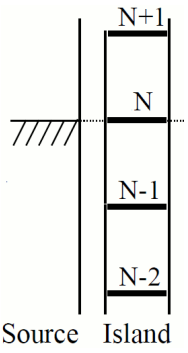

Figure B.1: Discrete energy states on an island (adapted from [45]). The number of electrons on an electrically neutral island is denoted with N.

B.2 Single Electron Box and Single Electron Trap

The discrete energy spectrum of the island gives rise to a number of interesting applications. One of them is known as *single electron box* The schematic design of a single electron box is illustrated in Fig. B.2(a). It consists of an island which is separated from the source lead by a tunneling barrier but stays at the same electrochemical potential. In addition, a *gate electrode* is coupled electrostatically to the island. Voltage applied to the gate shifts the island potential. If the energy states of the island are aligned with the electrochemical potential of the source lead, single electrons can tunnel to or from the island, charging or discharging it by e (see Fig. B.1).

Increasing the number of islands one obtains the *single electron trap*. This setup posseses the property of *bistability* (or more general of *multistability*). By applying a sufficiently high gate voltage an electron can be driven onto the edge island. Its charge prevents other electrons from following. After the gate voltage returns to the initial level, the electron is trapped on the edge island (Fig. B.2(d)); trap times of several hours were observed [146]. So, by cycling the gate voltage from initial to some critical value the device can be repeatedly switched between two

Figure B.2: Single electron charging effects and applications (from Likharev[46])

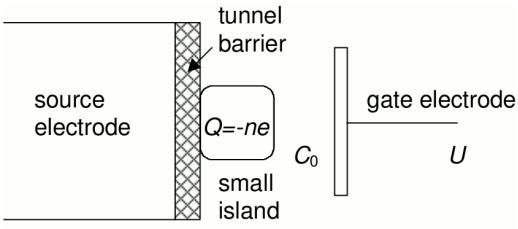

(a) Scheme of a single electron box

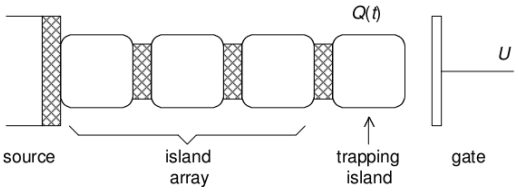

(b) Scheme of a single electron trap

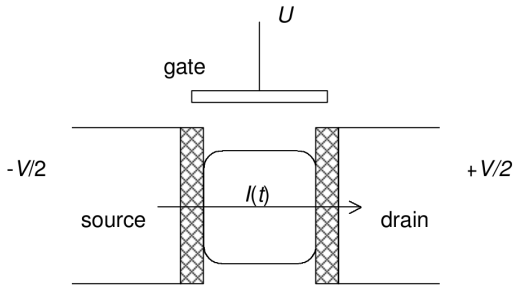

(c) Scheme of a single electron transistor

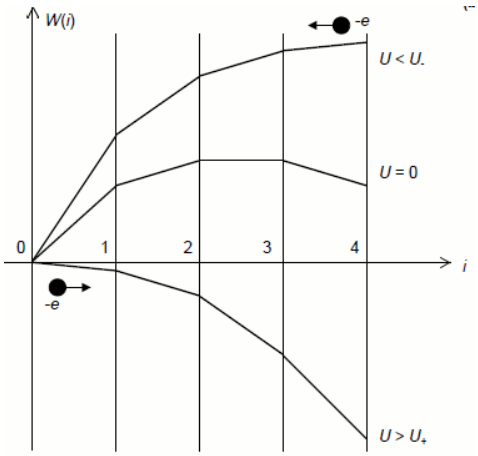

(d) Electrostatic energy of an extra electron in a single electron trap as a function of its position for three values of the gate voltage U

stable states (charged/uncharged edge island). The Geerligs device (Section 2.2 on page 13) can be seen as a combination of two single electron traps.

B.3 Single Electron Transistor

Adding a drain electrode to the single electron box results in a new device, known as *single electron transistor* (SET, see Fig. B.2(c)). Typical characteristics of an SET in the $V_{sd} - V_g$ space (so–called *stability diagram*) are shown in Fig. B.3. Several diamond–shaped regions are clearly visible, a feature which made this kind of plot known as *diamond plot*.

The SET can be operated in two different modes. For small bias values the current through the SET is suppressed (off-state) due to Coulomb blockade (white areas in the centre of the Fig. B.3). There, an electron occupying an energy state of

the island is preventing further electron flow. At the same time it can escape to neither of the leads as both source and drain lie energetically higher (compare the left inset in Fig. B.3). By changing the potentials of source, drain and/or gate electrodes, different energetic configurations of the SET can be achieved (comp. insets on the right in Fig. B.3), allowing electron flow through the device. This on–state is achieved, if one or several energy states of the island lie energetically between the electrochemical potential of the source and the drain electrode.
Obviously, while the SET is perfectly able to *confine* charge on single electron level, it fails to control one-by-one electron *output*. Indeed, Fig. B.3 shows that at the border between the N and $N+1$ (insets on the right illustrate different possibilities) there is a degeneracy of occupancy of the island. There is no possibility to control the number of electrons defining the net flow from source to drain. Therefore, a plain SET cannot be employed as a device for generating quantized current. However, the existing implementations of such devices are build upon the SET.

B.3.1 Excited States

Electrons occupying the island have various degrees of freedom, such as spin direction of individual electrons or different modes of the collective electron motion (radial, rotational, vibrational, etc) on the island. These degrees of freedom provide tunneling channel additional to channels sketched in Fig. B.3, and are commonly known as *excited states* (see also Fig. B.4).

B.3.2 Quantum Dot

In addition to the discrete energy spectrum originating from the Coulomb repulsion as introduced in Section B.1 there is also the quantum mechanical contribution. It originates from the fact, that energy quantization is expected, if the size of the island is comparable to the electron wave length. With the size of the island reaching nanometer–regime the quantum mechanical energy–level spacing is increasing rapidly and is comparable with or even exceeds the electrostatic charging energy.

Figure B.3: Stability diagram of an SET. White areas correspond to the Coulomb blockade regime (left inset). In greyed areas the number of electrons on the island is fluctuating by one unit and the current is flowing through a single state of the island (the SET is in the on–state). For dark areas the bias voltage V_{sd} is high enough to allow electron tunneling through several energy states of the island. On the right: energy schemes for SET configurations along the border lines of adjacent areas. (adapted from[87])

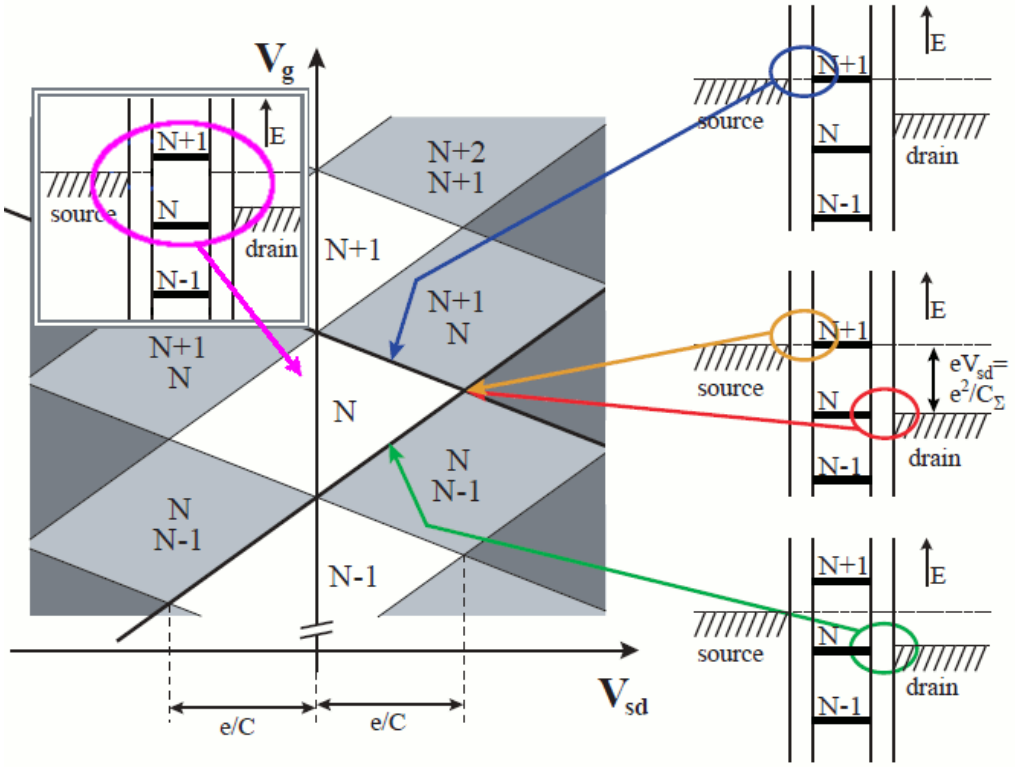

Islands with significant size of quantum mechanical energy–level spacing are called *quantum dots* (QD). Main differences between common island and QDs are illustrated in Fig. B.4.

Figure B.4: Stability diagram for an SET based on a metallic island (left) and a quantum dot (right) (adapted from [45]). Top: scheme of energy states. The number of excited states (drawn in thin lines) is smaller for QDs, given the lower number of electrons present. Bottom: typical stability diagrams. While the areas in the $V_{sd} - V_g$ plane are equally shaped for larger islands, the regions in the QD diagram are irregularly shaped. The reason is the interplay between the energy–level spacing and charging energy.

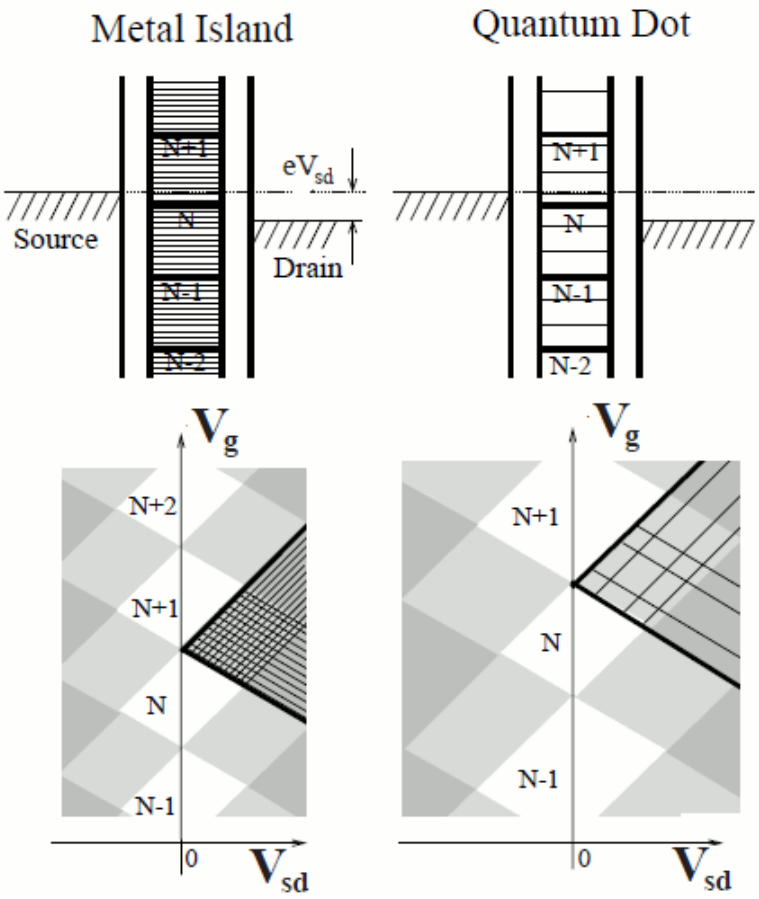

Appendix C

Single Walled Carbon Nanotubes

C.1 General Overview

After the publication of Iijima in 1991[15] the carbon nanotubes received an overwhelming attention of the scientific community and the general public. They also were often predicted to be the substance of the upcoming age[90, 147]. Among proposed applications were nanoscale electronic and mechanic devices, suitable solution for H_2–storage[148] and building space elevators[149], yarning, artificial muscles, and many more[150, 151].
Though some hopes proved to be false, this topic is still investigated by a vibrant and growing community (see e.g. [16, 20, 147]). Much of the knowledge acquired with nanotubes could be transferred and successfully used for graphene, a single sheet of graphite, which currently emerges as interesting candidate for exciting research and applications (e.g. applications in GHz regime[152]) as visualized in Fig. C.1.

Thermal& mechanical applications As described above, CNTs have mechanical and thermal properties, which – in combination with polymers – lead to light and strong materials. The targeted aplications are

- thermal conductors and
- mechanically strong and/or electrically conducting plastics.

Applications resulting from the geometrical shape The vessel–like shape of CNTs inspired to many different possible applications. Prominent examples for imaginable applications are:

Figure C.1: Time dependent number of articles on carbon allotropes (from Barth and Marx[153])

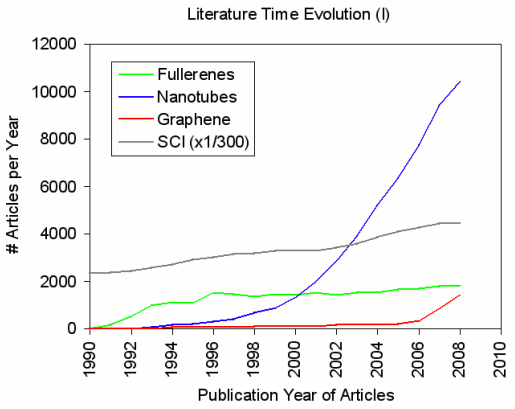

(a) Total number of articles on fullerenes, nanotubes, and graphene. The Science Citation Index (SCI) is shown as a rough measure for the growth of scientific literature.

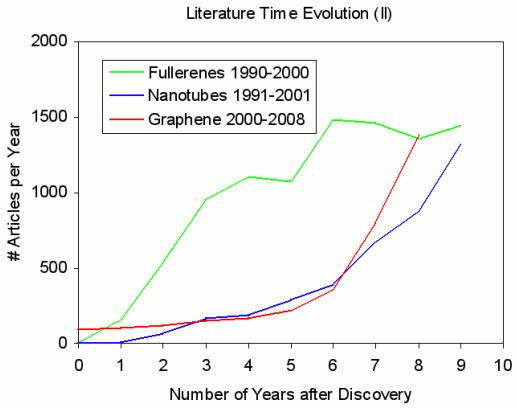

(b) Number of articles within the first decade after discovery

- hydrogen storage[148, 151]
- encapsulating and transport of active ingredients in biological systems (so–called *drug delivery systems*)
- friction-free membranes[154]
- channeling of high-energy particle beams[155] etc.

Figure C.2: Possible usage of CNTs in integrated circuits

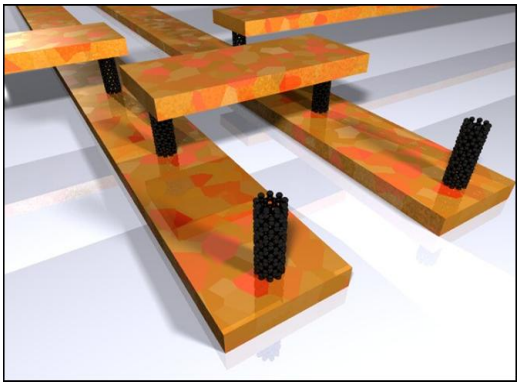

(a) A metallic CNT as an interconnect

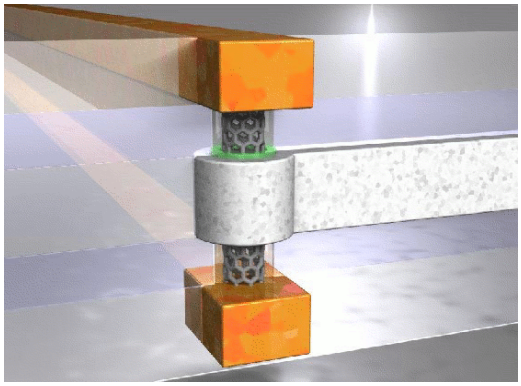

(b) Vertical CNT–based transistor

Electronics based on CNTs Maybe the topic which attracts most interest in CNT research:

- gas sensors[156, 157]
- field electron-emitting sources[25]
- light emitting devices[27]
- CNT-based transistors
- metallic interconnects for better electrical connection[158, 159] Fig. C.2(a)
- 3–dimensional stacking of transistors in future computer chips [160] as illustrated in Fig. C.2(b)
- transparent conducting films and transistors[161, 162]
- spintronic devices[28]

C.2 Chemical Properties

A single carbon nanotube can be considered as a seamlessly wrapped up graphene sheet. For this reason the tube is chemically as good as inert except for the end–cap regions. Here the curvature effects provide for non saturated bonds, making these parts reactive. This explains the properties of CNTs, as there were for example:

Thermal stability SWNTs can be heated to very high temperature (400 °C in ambient condition, more than 1000 °C without oxygen). As stated above, the end caps are the parts which disintegrate first. This property is widely used, as a method of purification of the SWNT material. The amorphous carbon, which makes the considerable share of impurities burns in presence of O_2 at lower temperatures than nanotubes. It also allows to open SWNTs to fill them with other nanoparticles, e.g. with (metallo-endo-)fullerenes[163]. Furthermore, by heating the interface between a nanotube and the contact metal – either by passing high current through either one of them or in a furnace – it is possible to obtain contact resistances close to the theoretical limit.

Figure C.3: Aqueous dispersion of CNT bundles and individual nanotubes using SDS micelles[164]. SWNT are indicated in blue, hydrophilic end of the SDS is red, the hydrophobic tail is green.

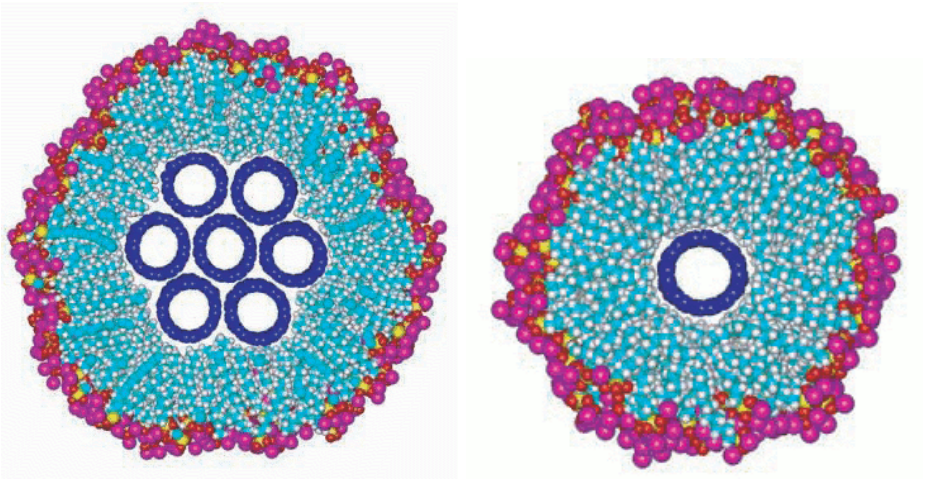

Low solubility Fullerenes "consist" – in a manner of speaking – of end caps only. This manifests also in their much higher solubility in organic solvents (e.g. toluol). The behaviour of carbon nanotubes is dominated by their walls, which are hardly reactive. Therefore, obtaining a suspension of CNTs requires more effort. One of the methods often described in literature and also used in this work involves two steps. Firstly, the nanotube material is dispersed by ultrasonication. However, once dispersed, nanotubes would re–bundle quickly, making it impossible to obtain individual SWNT. The bundling is prevented by adding a surfactant – usually sodium dodecyl sulfate(SDS) – which, at certain concentration (in our case 1%) creates micelles around dispersed particles, such as individual SWNT, remaining bundles and amorphous carbon (Fig. C.3). Such suspensions are stable for a sufficiently long time.

C.3 Electrical Properties

The electrical properties of carbon nanotubes result from the electron band structure of graphene. In graphene the conduction and the valence bands touch in exactly six (K–)points as illustrated in Fig. C.4. These six points in the momentum space form the characteristic hexagon pattern.
The (imaginary) rolling of the graphene sheet to a SWNT occurs along a direction defined by the *rolling vector* $na_1 + ma_2$, where n and m are integer values along

the base vectors of the graphene lattice, see Fig. C.5. As these values can unambiguously describe the properties of an individual SWNT they are commonly used as (n, m)–*indices* for identifying different nanotube types.

Rolling up of the SWNT also imposes a periodic boundary condition in the direction perpendicular to the axis of the nanotube. As a consequence, the Brillouin zone is reduced to lines. These lines have different distances to the K–points, which corresponds to the energy gap in resulting semiconducting nanotubes (i.e. $\mathrm{mod}\ n - m/3 \neq 0$). For metallic nanotubes the lines cross the K–points exactly(i.e. $\mathrm{mod}\ n - m/3 = 0$).

Theoretically, exactly one third of all possible ways of rolling up the graphene results in metallic nanotubes. This, however, is not always of a practical importance, as the generation and post–process of SWNT might have preferences for certain (n, m). During the work majority of the measured SWNT exceeding 66% was semiconducting.

In addition to the band gap originating from the periodic conditions imposed on the graphene sheet and scaling inversely proportional with the diameter $\sim 1/d$, the actual curvature of the SWNT has to be taken into account, as it results in deviations from an ideal graphene lattice. Due to these deviations an additional band gap $\sim 1/d^2$ opens in nanotubes, which should be otherwise considered metallic due to their (n, m) indices. Therefore, only the so–called *armchair* nanotubes (of the type (n, n)) are truly metallic.

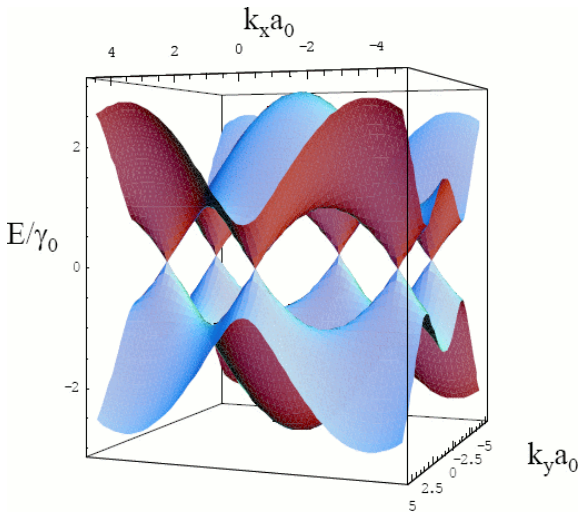

Figure C.4: Graphene band structure

Figure C.5: Type–dependence of SWNT on the (n,m)–indeces

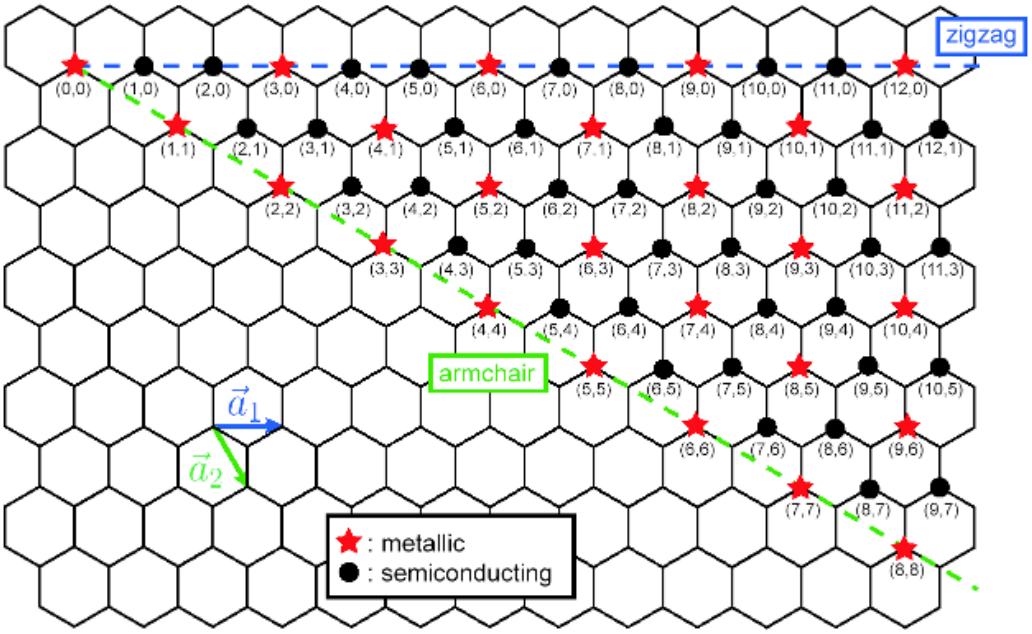

C.3.1 SWNT as Quantum Dot and Quantum Wire

In an idealized carbon nanotube the momentum is quantized only along the circumference. However, a carbon nanotube of a finate length, as defined by metal contacts, is different. Electrons within such a carbon nanotube behave according to the quantum mechanical 'particle-in-a-box'–model. This gives rise to quantum mechanical energy–level splitting as also described in Section B.3.2[1].
The energy splitting ΔE in a SWNT equals to

$$\Delta E = \frac{h\nu_f}{2L}, \tag{C.1}$$

where L is the length of the nanotube, $\nu_f \approx 8.1 \cdot 10^5 \mathrm{m\,sec}^- 1$ is the Fermi velocity for graphene. Nanotube based quantum dots have been investigated soon[41, 166] after their discovery.
Is a nanotube well–coupled to the leads, i.e. with the contact resistance below $R_K = h/e^2$, a quantum wire behaviour can be observed in phenomena such as Fabry–Perot–interferometry[167] or Luttinger liquid[168–172] behaviour.

[1] In addition there are effects appearing in very short nanotubes, such as change of the band gap as reported in e.g. [165]

Bibliography

[1] K. K. Likharev and A. B. Zorin, J. Low. Temp. Phys. **59**, 347 (1985).

[2] F. Piquemal, A. Bounouh, L. Devoille, N. Feltin, O. Thevenot, and G. Trapon, C. R. Physique **5** (2004).

[3] M. W. Keller, Metrologia **45**, 102 (2008), URL http://stacks.iop.org/0026-1394/45/102.

[4] K. v. Klitzing, G. Dorda, and M. Pepper, Phys. Rev. Lett. **45**, 494 (1980).

[5] K. v. Klitzing, Rev. Mod. Phys. **58**, 519 (1986).

[6] B. D. Josephson, Physics Letters **1**, 251 (1962).

[7] B. Jeckelmann and B. Jeanneret, Measurement Science and Technology **14**, 1229 (2003), URL http://stacks.iop.org/0957-0233/14/1229.

[8] L. J. Geerligs, V. F. Anderegg, P. A. M. Holweg, J. E. Mooij, H. Pothier, D. Esteve, C. Urbina, and M. H. Devoret, Phys. Rev. Lett. **64**, 2691 (1990), URL http://link.aps.org/abstract/PRL/v64/p2691.

[9] L. P. Kouwenhoven, A. T. Johnson, N. C. van der Vaart, C. P. M. Harmans, and C. T. Foxon, Phys. Rev. Lett. **67**, 1626 (1991), URL http://link.aps.org/abstract/PRL/v67/p1626.

[10] M. W. Keller, A. L. Eichenberger, J. M. Martinis, and N. M. Zimmerman, Science **285**, 1706 (1999), URL http://www.sciencemag.org/cgi/content/abstract/285/5434/1706.

[11] S. V. Lotkhov, S. A. Bogoslovsky, A. B. Zorin, and J. Niemeyer, Appl. Phys. Lett. **78**, 946 (2001), URL http://link.aip.org/link/?APL/78/946/1.

[12] M. D. Blumenthal, B. Kaestner, L. Li, S. Giblin, T. J. B. M. Janssen, M. Pepper, D. Anderson, G. Jones, and D. A. Ritchie, Nature Phys. **3**, 343 (2007), ISSN 1745-2473, URL http://dx.doi.org/10.1038/nphys582.

[13] A. Fujiwara, N. M. Zimmerman, Y. Ono, and Y. Takahashi, Appl. Phys. Lett. **84**, 1323 (2004), URL http://link.aip.org/link/?APL/84/1323/1.

[14] J. M. Shilton, V. I. Talyanskii, M. Pepper, D. A. Ritchie, J. E. F. Frost, C. J. B. Ford, C. G. Smith, and G. A. C. Jones, Journal of Physics: Condensed Matter **8**, L531 (1996), URL http://stacks.iop.org/0953-8984/8/L531.

[15] S. Iijima, Nature **354**, 56 (1991), URL http://dx.doi.org/10.1038/354056a0.

[16] W. Marx and A. Barth, physica status solidi (b) **245**, 2347 (2008), URL http://dx.doi.org/10.1002/pssb.200879660.

[17] R. Saito, G. Dresselhaus, and M. S. Dresselhaus, *Physical Properties of Carbon Nanotubes* (World Scientific Publishing Company, 1998), ISBN 1860940935.

[18] S. Reich, C. Thomsen, and J. Maultzsch, *Carbon Nanotubes: Basic Concepts and Physical Properties* (Wiley-VCH, 2004).

[19] M. P. Anantram and F. Leonard, Reports on Progress in Physics **69**, 507 (2006), URL http://stacks.iop.org/0034-4885/69/507.

[20] J.-C. Charlier, X. Blase, and S. Roche, Rev. Mod. Phys. **79**, 677 (pages 56) (2007), URL http://link.aps.org/abstract/RMP/v79/p677.

[21] S. Maruyama, URL http://www.photon.t.u-tokyo.ac.jp/~maruyama/.

[22] L. X. Zheng, M. J. O'Connell, S. K. Doorn, X. Z. Liao, Y. H. Zhao, E. A. Akhadov, M. A. Hoffbauer, B. J. Roop, Q. X. Jia, R. C. Dye, et al., Nature Mater. **3**, 673 (2004), ISSN 1476-1122, 10.1038/nmat1216, URL http://dx.doi.org/10.1038/nmat1216.

[23] S. Datta, *Electronic Transport in Mesoscopic Systems* (Cambridge Studies in Semiconductor Physics and Microelectronic Engineering, 1997).

[24] A. Javey, J. Guo, Q. Wang, M. Lundstrom, and H. Dai, Nature **424**, 654 (2003), ISSN 0028-0836, 10.1038/nature01797, URL http://dx.doi.org/10.1038/nature01797.

[25] Y. Saito, K. Hamaguchi, K. Hata, K. Uchida, Y. Tasaka, F. Ikazaki, M. Yumura, A. Kasuya, and Y. Nishina, Nature **389**, 554 (1997), ISSN 0028-0836, 10.1038/39221, URL http://dx.doi.org/10.1038/39221.

[26] S. J. Tans, A. R. M. Verschueren, and C. Dekker, Nature **393**, 49 (1998), ISSN 0028-0836, 10.1038/29954, URL http://dx.doi.org/10.1038/29954.

[27] J. A. Misewich, R. Martel, P. Avouris, J. C. Tsang, S. Heinze, and J. Tersoff, Science **300**, 783 (2003), 10.1126/science.1081294, URL http://www.sciencemag.org/cgi/content/abstract/300/5620/783.

[28] K. Tsukagoshi, B. W. Alphenaar, and H. Ago, Nature **401**, 572 (1999), ISSN 0028-0836, URL http://dx.doi.org/10.1038/44108.

[29] J. Appenzeller and D. J. Frank, Appl. Phys. Lett. **84**, 1771 (2004), URL http://link.aip.org/link/?APL/84/1771/1.

[30] J. Chaste, L. Lechner, P. Morfin, G. Feve, T. Kontos, J.-M. Berroir, D. C. Glattli, H. Happy, P. Hakonen, and B. Placais, Nano Letters **8**, 525 (2008), ISSN 1530-6984, URL http://dx.doi.org/10.1021/nl0727361.

[31] N. Chimot, V. Derycke, M. F. Goffman, J. P. Bourgoin, H. Happy, and G. Dambrine, Appl. Phys. Lett. **91**, 153111 (pages 3) (2007), URL http://link.aip.org/link/?APL/91/153111/1.

[32] K. Jensen, J. Weldon, H. Garcia, and A. Zettl, Nano Letters **7**, 3508 (2007), ISSN 1530-6984, URL http://dx.doi.org/10.1021/nl0721113.

[33] J. Bylander, T. Duty, and P. Delsing, Nature **434**, 361 (2005).

[34] Z. Zhong, N. M. Gabor, J. E. Sharping, A. L. Gaeta, and P. L. McEuen, NATURE NANOTECHNOLOGY **3**, 201 (2008), ISSN 1748-3387.

[35] D. Kienle and F. Leonard, PHYSICAL REVIEW LETTERS **103** (2009), ISSN 0031-9007.

[36] V. Talyanskii, D. Novikov, B. Simons, and L. Levitov, Phys. Rev. Lett. **87**, 276802 (2001).

[37] B. Kaestner, Private communication.

[38] P. J. Leek, M. R. Buitelaar, V. I. Talyanskii, C. G. Smith, D. Anderson, G. A. C. Jones, J. Wei, and D. H. Cobden, Phys. Rev. Lett. **95**, 256802 (pages 4) (2005), URL http://link.aps.org/abstract/PRL/v95/e256802.

[39] C. Würstle, J. Ebbecke, M. E. Regler, and A. Wixforth, New J. of Physics **9**, 73 (2007), URL http://stacks.iop.org/1367-2630/9/73.

[40] Y. A. Pashkin, Y. Nakamura, and J. S. Tsai, Appl. Phys. Lett. **76**, 2256 (2000), URL http://link.aip.org/link/?APL/76/2256/1.

[41] S. J. Tans, M. H. Devoret, H. Dai, A. Thess, R. E. Smalley, L. J. Geerligs, and C. Dekker, Nature **386**, 474 (1997), URL http://dx.doi.org/10.1038/386474a0.

[42] M. R. Buitelaar, V. Kashcheyevs, P. J. Leek, V. I. Talyanskii, C. G. Smith, D. Anderson, G. A. C. Jones, J. Wei, and D. H. Cobden, Phys. Rev. Lett. **101**, 126803 (pages 4) (2008), URL http://link.aps.org/abstract/PRL/v101/e126803.

[43] J. P. Pekola, J. J. Vartiainen, M. Mottonen, O.-P. Saira, M. Meschke, and D. V. Averin, Nature Phys. **4**, 120 (2008), ISSN 1745-2473, URL http://dx.doi.org/10.1038/nphys808.

[44] D. J. Thouless, Physical Review B **27**, 6083 (1983), URL http://link.aps.org/abstract/PRB/v27/p6083.

[45] J. Weis, *Electrical transport through quantum dot systems*, Habilitationsschrift (2002).

[46] K. Likharev, in *Proceedings of the IEEE* (1999), vol. 87, pp. 606 – 632.

[47] D. V. Averin and K. K. Likharev, *Mesoscopic Phenomena in Solids* (Elsevier, Amsterdam, 1991), p. 173.

[48] L. Geerligs, Surface Science **263**, 396 (1992), ISSN 0039-6028, URL http://www.sciencedirect.com/science/article/B6TVX-46XB091-107/2/74a067d048a53e5fbc3d94fc6c4c3116.

[49] A. A. Odintsov, Appl. Phys. Lett. **58**, 2695 (1991), URL http://link.aip.org/link/?APL/58/2695/1.

[50] M. W. Keller, J. M. Martinis, N. M. Zimmerman, and A. H. Steinbach, Appl. Phys. Lett. **69**, 1804 (1996), URL http://link.aip.org/link/?APL/69/1804/1.

[51] N. Fletcher et al., Physical Review B **68**, 245310 (pages 9) (2003), URL http://link.aps.org/abstract/PRB/v68/e245310.

[52] V. I. Talyanskii, J. M. Shilton, M. Pepper, C. G. Smith, C. J. B. Ford, E. H. Linfield, D. A. Ritchie, and G. A. C. Jones, Phys. Rev. B **56**, 15180 (1997).

[53] J. Cunningham, V. I. Talyanskii, J. M. Shilton, M. Pepper, A. Kristensen, and P. E. Lindelof, Phys. Rev. B **62**, 1564 (2000).

[54] J. Cunningham, V. I. Talyanskii, J. M. Shilton, M. Pepper, M. Y. Simmons, and D. A. Ritchie, Phys. Rev. B **60**, 4850 (1999), URL http://link.aps.org/abstract/PRB/v60/p4850.

[55] V. I. Talyanskii, J. M. Shilton, J. Cunningham, M. Pepper, C. J. B. Ford, C. G. Smith, E. H. Linfield, D. A. Ritchie, and G. A. C. Jones, Physica B **249-251**, 140 (1998).

[56] J. Ebbecke, G. Bastian, M. Blöcker, K. Pierz, and F. J. Ahlers, Appl. Phys. Lett **77**, 2601 (2000).

[57] J. Ebbecke, N. E. Fletcher, T. J. B. M. Janssen, H. E. Beere, D. A. Ritchie, and M. Pepper, Phys. Rev. B **72**, 121311 (2005).

[58] A. Aharony and O. Entin-Wohlman, Phys. Rev. B **65**, 241401 (2002).

[59] G. R. Aĭzin, G. Gumbs, and M. Pepper, Phys. Rev. B **58**, 10589 (1998).

[60] H. Totland, O. L. Bø, and Y. M. Galperin, Phys. Rev. B **56**, 15299 (1997).

[61] O. Entin-Wohlman, A. Aharony, and V. Kashcheyevs, TURK.J.PHYS. **27**, 371 (2003), URL http://www.citebase.org/abstract?id=oai:arXiv.org:cond-mat/0308408.

[62] K. Flensberg, Q. Niu, and M. Pustilnik, Phys. Rev. B **60**, R16291 (1999).

[63] V. Kashcheyevs, A. Aharony, and O. Entin-Wohlman, Eur. Phys. J. B **39**, 385 (2004), URL http://dx.doi.org/10.1140/epjb/e2004-00204-0.

[64] S. Hatch, Master's thesis, University of Western Australia (2000).

[65] B. Simons, *Quantized adiabatic charge transport in a carbon nanotube*, Seminar given at the Annual Condensed Matter Theory Group meeting of the IOP (2001).

[66] M. Switkes, C. M. Marcus, K. Campman, and A. C. Gossard, Science **283**, 1905 (1999), URL http://www.sciencemag.org/cgi/content/abstract/283/5409/1905.

[67] Q. Niu, Phys. Rev. Lett. **64**, 1812 (1990), URL http://link.aps.org/abstract/PRL/v64/p1812.

[68] J. E. Avron, D. Osadchy, and R. Seiler, Physics Today **56**, 38 (2003), URL http://link.aip.org/link/?PTO/56/38/1.

[69] Q. Niu and D. J. Thouless, Journal of Physics A: Mathematical and General **17**, 2453 (1984), URL http://stacks.iop.org/0305-4470/17/2453.

[70] Q. Niu, Phys. Rev. B **34**, 5093 (1986).

[71] J. Ebbecke, C. J. Strobl, and A. Wixforth, Physical Review B **70**, 233401 (pages 4) (2004), URL http://link.aps.org/abstract/PRB/v70/e233401.

[72] P. J. Leek, Ph.D. thesis, University of Cambridge (2006).

[73] B. Kaestner, V. Kashcheyevs, S. Amakawa, M. D. Blumenthal, L. Li, T. J. B. M. Janssen, G. Hein, K. Pierz, T. Weimann, U. Siegner, et al., Phys. Rev. B **77**, 153301 (2008), URL http://link.aps.org/abstract/PRB/v77/e153301.

[74] B. Kaestner, V. Kashcheyevs, G. Hein, K. Pierz, U. Siegner, and H. W. Schumacher, Appl. Phys. Lett. **92**, 192106 (pages 3) (2008), URL http://link.aip.org/link/?APL/92/192106/1.

[75] A. Kemppinen, M. Meschke, M. Mottonen, D. V. Averin, and J. P. Pekola, Eur. Phys. J. **172**, 311 (2009), URL http://dx.doi.org/10.1140/epjst/e2009-01056-0.

[76] D. V. Averin and J. P. Pekola, Phys. Rev. Lett. **101**, 066801 (pages 4) (2008), URL http://link.aps.org/abstract/PRL/v101/e066801.

[77] W. Buckel and R. Kleiner, *Superconductivity: Fundamentals and Applications* (Wiley-VCH, 2004).

[78] S. Hunklinger, *Skript zur Vorlesung Festkorperphysik* (Heidelberg, 2004).

[79] A. Kemppinen, S. Kafanov, Y. A. Pashkin, J. S. Tsai, D. V. Averin, and J. P. Pekola, Appl. Phys. Lett. **94**, 172108 (pages 3) (2009), URL http://link.aip.org/link/?APL/94/172108/1.

[80] K. Hata, D. N. Futaba, K. Mizuno, T. Namai, M. Yumura, and S. Iijima, Science **306**, 1362 (2004), URL http://www.sciencemag.org/cgi/reprint/306/5700/1362.pdf.

[81] A. F. Morpurgo, J. Kong, C. M. Marcus, and H. Dai, Science **286**, 263 (1999), URL http://www.sciencemag.org/cgi/reprint/286/5438/263.pdf.

[82] P. Jarillo-Herrero, J. Kong, H. S. J. van der Zant, C. Dekker, L. P. Kouwenhoven, and S. D. Franceschi, Phys. Rev. Lett. **94**, 156802 (pages 4) (2005), URL http://link.aps.org/abstract/PRL/v94/e156802.

[83] P. Jarillo-Herrero, J. A. van Dam, and L. P. Kouwenhoven, Nature **439**, 953 (2006), ISSN 0028-0836, URL http://dx.doi.org/10.1038/nature04550.

[84] G. S. Düsberg, Ph.D. thesis, Eberhard Karls Universität Tübingen (2001).

[85] V. C. Moore, M. S. Strano, E. H. Haroz, R. H. Hauge, R. E. Smalley, J. Schmidt, and Y. Talmon, Nano Letters **3**, 1379 (2003), ISSN 1530-6984, URL http://pubs3.acs.org/acs/journals/doilookup?in_doi=10.1021/nl034524j.

[86] J. Muster, Ph.D. thesis, Technische Universität Kaiserslautern (2007).

[87] D. Obergfell, Ph.D. thesis, Eberhard Karls Universität Tübingen (2009).

[88] S. Sahakalkan, Private communication.

[89] J. C. Meyer, D. Obergfell, S. Roth, S. Yang, and S. Yang, Appl. Phys. Lett. **85**, 2911 (2004), URL http://link.aip.org/link/?APL/85/2911/1.

[90] P. Avouris, Chemical Physics **281**, 429 (2002), URL http://www.sciencedirect.com/science/article/B6TFM-45G01CM-1/2/8026aa6b058cf77ce8245a65832b9eff.

[91] C.-W. Liang, Ph.D. thesis, Eberhard Karls Universität Tübingen (2009), URL http://tobias-lib.ub.uni-tuebingen.de/volltexte/2009/3907/.

[92] V. Krstic, Ph.D. thesis, ÉCOLE POLYTECHNIQUE FÉDÉRALE DE LAUSANNE (2002).

[93] Y. Zhang and H. Dai, Appl. Phys. Lett. **77**, 3015 (2000), URL http://link.aip.org/link/?APL/77/3015/1.

[94] J. Haruyama, A. Tokita, N. Kobayashi, M. Nomura, S. Miyadai, K. Takazawa, A. Takeda, and Y. Kanda, Appl. Phys. Lett. **84**, 4714 (2004), URL http://link.aip.org/link/?APL/84/4714/1.

[95] R. Martel, V. Derycke, C. Lavoie, J. Appenzeller, K. K. Chan, J. Tersoff, and P. Avouris, Phys. Rev. Lett. **87**, 256805 (2001).

[96] B. Babić, Ph.D. thesis, University of Basel, Faculty of Science (2004).

[97] J. Zhao, J. Han, and J. P. Lu, Phys. Rev. B **65**, 193401 (2002).

[98] B. Shan and K. Cho, Phys. Rev. Lett. **94**, 236602 (2005).

[99] W. S. Su, T. C. Leung, and C. T. Chan, Phys. Rev. B **76**, 235413 (pages 8) (2007), URL http://link.aps.org/abstract/PRB/v76/e235413.

[100] J. Sun, Z. Zhang, S. Hou, G. Zhang, Z. Gu, X. Zhao, W. Liu, and Z. Xue, Applied Physics A: Materials Science & Processing **75**, 479 (2002), URL http://dx.doi.org/10.1007/s003390201403.

[101] R. D'Arcy and N. Surplice, Surface Science **36**, 783 (1973), ISSN 0039-6028, URL http://www.sciencedirect.com/science/article/B6TVX-46T3K4Y-13P/2/b7e1b881a5acf7e9427ba171a00654af.

[102] W. Brearley and N. Surplice, Surface Science **64**, 372 (1977), ISSN 0039-6028, URL http://www.sciencedirect.com/science/article/B6TVX-46SWSVX-2B/2/c72c0866d4871e6f902b5f277d8316e1.

[103] Z. Yao, Ph.D. thesis, The University of Texas at Austin (2007).

[104] J. Kong, E. Yenilmez, T. W. Tombler, W. Kim, H. Dai, R. B. Laughlin, L. Liu, C. S. Jayanthi, and S. Y. Wu, Phys. Rev. Lett. **87**, 106801 (2001).

[105] D. Mann, A. Javey, J. Kong, Q. Wang, and H. Dai, Nano Letters **3**, 1541 (2003), URL http://pubs.acs.org/doi/pdf/10.1021/nl034700o.

[106] J. Wu, W. Duan, B.-L. Gu, J.-Z. Yu, and Y. Kawazoe, Appl. Phys. Lett. **77**, 2554 (2000), URL http://link.aip.org/link/?APL/77/2554/1.

[107] K. Yamanouchi, T. Meguro, Y. Wagatsuma, H. Odagawa, and K. Yamamoto, Jap. J. Appl. Phys. **33**, 3018 (1994), URL http://jjap.ipap.jp/link?JJAP/33/3018/.

[108] W. Kim, A. Javey, R. Tu, J. Cao, Q. Wang, and H. Dai, Appl. Phys. Lett. **87**, 173101 (pages 3) (2005), URL http://link.aip.org/link/?APL/87/173101/1.

[109] G. A. Smolenskii, N. N. Krainik, N. P. Khuchua, V. V. Zhdanova, and I. E. Mylnikova, physica status solidi (b) **13**, 309 (1966), URL http://dx.doi.org/10.1002/pssb.19660130202.

[110] K. K. Wong, ed., *Properties of Lithium Niobate* (The Institution of Engineering and Technology, 2002).

[111] C. K. Campbell, *Surface Acoustic Wave Devices and Their Signal Processing Applications* (Academic Press Inc, 1989).

[112] M. J. Biercuk, N. Mason, and C. M. Marcus, Nano Letters **4**, 1 (2004), ISSN 1530-6984, URL http://dx.doi.org/10.1021/nl034696g.

[113] N. Mason, M. J. Biercuk, and C. M. Marcus, Science **303**, 655 (2004), URL http://www.sciencemag.org/cgi/content/abstract/303/5658/655.

[114] M. R. Graber, T. Nussbaumer, W. Belzig, and C. Schonenberger, Nanotechnology **15**, S479 (2004), URL http://stacks.iop.org/0957-4484/15/S479.

[115] Y.-L. Zhong, T. Akazaki, K. Kanzaki, Y. Kobayashi, and H. Takayanagi, Science and Technology of Advanced Materials **7**, S78 (2006), URL http://stacks.iop.org/1468-6996/7/S78.

[116] W. A. Little, Phys. Rev. **134**, A1416 (1964).

[117] E. Pallecchi, M. Gaass, D. A. Ryndyk, and C. Strunk, Appl. Phys. Lett. **93**, 072501 (pages 3) (2008), URL http://link.aip.org/link/?APL/93/072501/1.

[118] A. Y. Kasumov, R. Deblock, M. Kociak, B. Reulet, H. Bouchiat, I. I. Khodos, Y. B. Gorbatov, V. T. Volkov, C. Journet, and M. Burghard, Science **284**, 1508 (1999), URL http://www.sciencemag.org/cgi/content/abstract/284/5419/1508.

[119] A. Kasumov, M. Kociak, M. Ferrier, R. Deblock, S. Guéron, B. Reulet, I. Khodos, O. Stéphan, and H. Bouchiat, Phys. Rev. B **68**, 214521 (2003).

[120] Z. K. Tang, L. Zhang, N. Wang, X. X. Zhang, G. H. Wen, G. D. Li, J. N. Wang, C. T. Chan, and P. Sheng, Science **292**, 2462 (2001), URL http://www.sciencemag.org/cgi/content/abstract/292/5526/2462.

[121] N. Sato, Journal of Applied Physics **67**, 7493 (1990), URL http://link.aip.org/link/?JAP/67/7493/1.

[122] K. Grove-Rasmussen, H. I. J. rgensen, B. M. Andersen, J. Paaske, T. S. Jespersen, J. N. rd, K. Flensberg, and P. E. Lindelof, Physical Review B (Condensed Matter and Materials Physics) **79**, 134518 (pages 5) (2009), URL http://link.aps.org/abstract/PRB/v79/e134518.

[123] J.-P. Cleuziou, W. Wernsdorfer, V. Bouchiat, T. Ondarcuhu, and M. Monthioux, Nature Nanotech. **1**, 53 (2006), ISSN 1748-3387, URL http://dx.doi.org/10.1038/nnano.2006.54.

[124] T. M. Klapwijk, Journal of Superconductivity **17**, 593 (2004), URL http://dx.doi.org/10.1007/s10948-004-0773-0.

[125] B. Pannetier and H. Courtois (1999), URL http://arxiv.org/abs/cond-mat/9912024.

[126] H. Y. Yu, D. S. Lee, U. Dettlaff-Weglikowska, S. Roth, and Y. W. Park, Phys. Rev. B **78**, 155415 (pages 5) (2008), URL http://link.aps.org/abstract/PRB/v78/e155415.

[127] S.-H. Jhang, S. W. Lee, D. S. Lee, Y. W. Park, G. Jeong, T. Hirata, R. Hatakeyama, U. Dettlaff, S. Roth, M. S. Kabir, et al., Fullerenes Nanotubes Carbon Nanostruct. **13**, 195 (2005).

[128] F. Giazotto, T. T. Heikkilä, A. Luukanen, A. M. Savin, and J. P. Pekola, Rev. Mod. Phys. **78**, 217 (pages 58) (2006), URL http://link.aps.org/abstract/RMP/v78/p217.

[129] C. Wiele, F. Haake, C. Rocke, and A. Wixforth, Physical Review A **58**, R2680 (1998), URL http://link.aps.org/abstract/PRA/v58/pR2680.

[130] C. Strobl et al., Appl. Phys. Lett. **85**, 1427 (2004), URL http://link.aip.org/link/?APL/85/1427/1.

[131] C. Rocke, S. Zimmermann, A. Wixforth, J. P. Kotthaus, G. Böhm, and G. Weimann, Phys. Rev. Lett. **78**, 4099 (1997).

[132] M. S. Arnold, A. A. Green, J. F. Hulvat, S. I. Stupp, and M. C. Hersam, Nature Nanotech. **1**, 60 (2006), ISSN 1748-3387, URL http://dx.doi.org/10.1038/nnano.2006.52.

[133] R. Krupke, F. Hennrich, H. v. Lohneysen, and M. M. Kappes, Science **301**, 344 (2003), URL http://www.sciencemag.org/cgi/content/abstract/301/5631/344.

[134] J. P. Pekola, F. Giazotto, and O.-P. Saira, Phys. Rev. Lett. **98**, 037201 (pages 4) (2007), URL http://link.aps.org/abstract/PRL/v98/e037201.

[135] M. Y. Han, B. Özyilmaz, Y. Zhang, and P. Kim, Phys. Rev. Lett. **98**, 206805 (pages 4) (2007), URL http://link.aps.org/abstract/PRL/v98/e206805.

[136] C. K. Campbell, *SAW Devices for Mobile and Wireless Communications* (Academic Press Inc, 1998).

[137] S. Sivaramakrishnan, R. Rajamani, C. Smith, K. McGee, K. Mann, and N. Yamashita, Sensors and Actuators B: Chemical **132**, 296 (2008), ISSN 0925-4005, URL http://www.sciencedirect.com/science/article/B6THH-4RR8YPD-4/2/04d792ee30203ebbb25ee4cde5e7ceb2.

[138] K. Länge, B. Rapp, and M. Rapp, Analytical and Bioanalytical Chemistry **391**, 1509 (2008), URL http://dx.doi.org/10.1007/s00216-008-1911-5.

[139] J. J. Caron, R. B. Haskell, J. C. Andle, and J. F. Vetelino, Sensors and Actuators B: Chemical **35**, 141 (1996), ISSN 0925-4005, proceedings of the Sixth International Meeting on Chemical Sensors, URL http://www.sciencedirect.com/science/article/B6THH-3TTDGV5-58/2/09751bee47951921409b86b775eca183.

[140] J. Mrosk, C. Ettl, L. Berger, P. Dabala, H. Fecht, G. Fischerauer, J. Hornsteiner, K. Riek, E. Riha, E. Born, et al., in *ndustrial Electronics Society, 1998. IECON '98. Proceedings of the 24th Annual Conference of the IEEE* (IEEE, 1998), vol. 4, pp. 2386–2390.

[141] C. Bödefeld, A. Wixforth, J. Toivonen, M. . Sopanen, and H. Lipsanen, physica status solidi (b) **224**, 703 (2001).

[142] C. H. W. Barnes, J. M. Shilton, and A. M. Robinson, Physical Review B **62**, 8410 (2000), URL http://link.aps.org/abstract/PRB/v62/p8410.

[143] R. White and F. Voltmer, Appl. Phys. Lett. **7**, 314 (1965), URL http://link.aip.org/link/?APL/7/314/1.

[144] D. V. Averin and K. K. Likharev, J. Low. Temp. Phys. **62**, 345 (1986), URL http://dx.doi.org/10.1007/BF00683469.

[145] T. A. Fulton and G. J. Dolan, Phys. Rev. Lett. **59**, 109 (1987), URL http://link.aps.org/abstract/PRL/v59/p109.

[146] P. D. Dresselhaus, L. Ji, S. Han, J. E. Lukens, and K. K. Likharev, Phys. Rev. Lett. **72**, 3226 (1994).

[147] P. Avouris, Spectrum, IEEE **41**, 40 (2004).

[148] B. Panella, M. Hirscher, and S. Roth, Carbon **43**, 2209 (2005), URL http://www.sciencedirect.com/science/article/B6TWD-4G4N0BS-D/2/f2113ad04f9aaae736998b0c4c28cfbb.

[149] B. C. Edwards, Acta Astronautica **47**, 735 (2000), URL http://www.sciencedirect.com/science/article/B6V1N-41P17DG-1/2/da496a4f5630c64bf69dd64d9bf2d9ed.

[150] M. Zhang, K. R. Atkinson, and R. H. Baughman, Science **306**, 1358 (2004), URL http://www.sciencemag.org/cgi/reprint/306/5700/1358.pdf.

[151] R. H. Baughman, A. A. Zakhidov, and W. A. de Heer, Science **297**, 787 (2002), URL http://www.sciencemag.org/cgi/reprint/297/5582/787.pdf.

[152] Y.-M. Lin, K. A. Jenkins, A. Valdes-Garcia, J. P. Small, D. B. Farmer, and P. Avouris, NANO LETTERS **9**, 422 (2009), ISSN 1530-6984.

[153] A. Barth and W. Marx.

[154] M. Majumder, N. Chopra, R. Andrews, and B. J. Hinds, Nature **438**, 44 (2005), ISSN 0028-0836, 10.1038/43844a, URL http://dx.doi.org/10.1038/43844a.

[155] S. Bellucci, V. M. Biryukov, Y. A. Chesnokov, V. Guidi, and W. Scandale, NUCL.INSTRUM.METH.B **202**, 236 (2003), URL http://www.citebase.org/abstract?id=oai:arXiv.org:physics/0208081.

[156] A. Modi, N. Koratkar, E. Lass, B. Wei, and P. M. Ajayan, Nature **424**, 171 (2003), ISSN 0028-0836, 10.1038/nature01777, URL http://dx.doi.org/10.1038/nature01777.

[157] J. Kong, N. R. Franklin, C. Zhou, M. G. Chapline, S. Peng, K. Cho, and H. Dai, Science **287**, 622 (2000), 10.1126/science.287.5453.622, URL http://www.sciencemag.org/cgi/content/abstract/287/5453/622.

[158] A. P. Graham, G. S. Duesberg, F. Kreupl, R. Seidel, M. Liebau, E. Unger, and W. Honlein, in *XVII International Winterschool/Euroconference on Electronic Properties of Novel Materials*, edited by H. Kuzmany, J. Fink, M. Mehring, and S. Roth (AIP, 2003), vol. 685, pp. 587–591, URL http://link.aip.org/link/?APC/685/587/1.

[159] W. Hoenlein, F. Kreupl, G. S. Duesberg, A. P. Graham, M. Liebau, R. Seidel, and E. Unger, ELECTRIC PROPERTIES OF SYNTHETIC NANOSTRUCTURES: XVII International Winterschool/Euroconference on Electronic Properties of Novel Materials **723**, 565 (2004), URL http://link.aip.org/link/?APC/723/565/1.

[160] F. Kreupl, G. S. Duesberg, A. P. Graham, M. Liebau, E. Unger, R. Seidel, W. Pamler, and W. Hoenlein, *Carbon nanotubes in microelectronic appli-*

cations (2004), URL http://www.citebase.org/abstract?id=oai:arXiv.org:cond-mat/0410360.

[161] Z. Wu, Z. Chen, X. Du, J. M. Logan, J. Sippel, M. Nikolou, K. Kamaras, J. R. Reynolds, D. B. Tanner, A. F. Hebard, et al., Science **305**, 1273 (2004), 10.1126/science.1101243, URL http://www.sciencemag.org/cgi/content/abstract/305/5688/1273.

[162] M. Kaempgen and S. Roth, in *MOLECULAR NANOSTRUCTURES: XVII International Winterschool Euroconference on Electronic Properties of Novel Materials*, edited by H. Kuzmany, J. Fink, M. Mehring, and S. Roth (AIP, 2003), vol. 685, pp. 554–558, URL http://link.aip.org/link/?APC/685/554/1.

[163] M. Ashino, D. Obergfell, M. Haluska, S. Yang, A. N. Khlobystov, S. Roth, and R. Wiesendanger, Nature Nanotech. **3**, 337 (2008), ISSN 1748-3387, 10.1038/nnano.2008.126, URL http://dx.doi.org/10.1038/nnano.2008.126.

[164] M. J. O'Connell, S. M. Bachilo, C. B. Huffman, V. C. Moore, M. S. Strano, E. H. Haroz, K. L. Rialon, P. J. Boul, W. H. Noon, C. Kittrell, et al., Science **297**, 593 (2002), URL http://www.sciencemag.org/cgi/reprint/297/5581/593.pdf.

[165] A. Rochefort, D. R. Salahub, and P. Avouris, The Journal of Physical Chemistry B **103**, 641 (1999), URL http://pubs.acs.org/doi/pdf/10.1021/jp983725m.

[166] M. Bockrath, D. H. Cobden, P. L. McEuen, N. G. Chopra, A. Zettl, A. Thess, and R. E. Smalley, Science **275**, 1922 (1997), URL http://www.sciencemag.org/cgi/reprint/275/5308/1922.pdf.

[167] W. Liang, M. Bockrath, D. Bozovic, J. H. Hafner, M. Tinkham, and H. Park, Nature **411**, 665 (2001), URL http://www.nature.com/physics/highlights/6838-1.html.

[168] M. Bockrath, D. H. Cobden, J. Lu, A. G. Rinzler, R. E. Smalley, L. Balents, and P. L. McEuen, Nature **397**, 598 (1999), ISSN 0028-0836, URL http://dx.doi.org/10.1038/17569.

[169] M. Bockrath, Nature **426**, 511 (2003), ISSN 0028-0836, URL http://dx.doi.org/10.1038/426511a.

[170] H. Ishii, H. Kataura, H. Shiozawa, H. Yoshioka, H. Otsubo, Y. Takayama, T. Miyahara, S. Suzuki, Y. Achiba, M. Nakatake, et al., Nature **426**, 540 (2003), ISSN 0028-0836, URL http://dx.doi.org/10.1038/nature02074.

[171] S. Bellucci, J. Gonzalez, and P. Onorato, Phys. Rev. Lett. **95**, 186403 (pages 4) (2005), URL http://link.aps.org/abstract/PRL/v95/e186403.

[172] C. Kane, L. Balents, and M. P. A. Fisher, Phys. Rev. Lett. **79**, 5086 (1997).

Danksagung

An dieser Stelle möchte ich vielen Menschen danken, die in der einen oder der anderen Form zu dieser Arbeit und ihrem Gelingen beigetragen haben.

Ich danke Professor Dr. Dieter Kern für seine Bereitschaft, meine Dissertation zu betreuen. Für seine freundliche Unterstützung während dieser Zeit, die Diskussionen und auch die Möglichkeit, als externer Doktorand am Leben seiner Arbeitsgruppe teilzunehmen, bin ich ihm äußerst dankbar.

Ich danke Professor Dr. Klaus von Klitzing dafür, mir die Forschung in seiner Abteilung am Max–Planck-Institut für Festkörperphysik ermöglicht zu haben. Auch danke ich für sein aufrichtiges Interesse an meiner Arbeit und Diskussionen, die meine Zeit am MPI bereichert haben.

Mein großer Dank gebührt Dr. habil. Siegmar Roth. Die Zeit, die ich in dieser Gruppe verbringen durfte, bleibt für immer unvergesslich. Ich möchte mich für die Möglichkeit bedanken, in einer einmaligen Umgebung gearbeitet zu haben, in der man sich nicht nur als Wissenschaftler, sondern auch als Persönlichkeit weierentwickeln konnte.

Ich danke Dr. Franz Josef Ahlers (Physikalisch–Technische–Bundesanstalt in Braunschweig), für die Einführung in das faszinierende Gebiet der Quantenmetrologie im Allgemeinen und der Einzelelektronenpumpen im Einzelnen.

Herzlich danken möchte ich Professoren Dres. Dieter Kölle und Reinhold Kleiner, wie auch Mitarbeitern ihrer Arbeitsgruppe, für die Diskussionen und Probenherstellung.

Dres. Hans–Werner Schumacher, Bernd Kästner, Sergey Lotkhov, Erol Sağol und Thomas Weimann (PTB) danke ich für lange, ausführliche und außerst hilfreiche Diskussionen, Hilfe bei Probenherstellung und Messungen.

Dr. Dirk Obergfell danke ich besonders (aber nicht ausschließlich :) dafür, mich in die Welt von Kohlenstoffröhrchen und die Gruppe von Dr. Roth eingeführt zu haben.

Martti, Chen–Wei und Serhat danke ich dafür, fantastische Bürokollegen gewesen zu sein, mit denen es viel Spass gemacht hat, (nicht nur) über wissenschaftliche Fragen zu diskutieren.

Allen Mitgliedern der Gruppe Roth danke ich vom ganzen Herzen für die wunderbare Zeit, die ich in in 4C11 und während der "$\sigma\rho$–travelling agency"–Ausflüge gehabt habe.

Mein Dank gilt meiner Familie, insbesondere meiner Frau Natalie und Tochter Annelie für ihre Kraft, Unterstützung und Liebe.